Double-Sided Arc Welding of AA5182

Aluminum Tailor Welded Blanks

By

Jeffrey A. Moulton

A thesis
presented to the University of Waterloo
in fulfillment of the
thesis requirement for the degree of
Master of Applied Science
in
Mechanical Engineering

Waterloo, Ontario, Canada, 2008

I hereby declare that I am the sole author of this thesis. This is a true copy of the thesis, including any required final revisions, as accepted by my examiners.

I understand that my thesis may be made electronically available to the public.

Abstract

Increasing regulatory pressure to reduce fuel consumption of new vehicles has prompted the automotive industry to seek ways to reduce the weight of their automobiles. The use of steel tailor welded blanks has been successful in reducing vehicle weight while simultaneously reducing manufacturing costs; however, further weight reductions are possible if steel alloys are substituted with aluminum alloys. This has created a need to identify and develop welding techniques that would enable the production of high-quality welds between aluminum sheets of different thicknesses at rates compatible with the demands of the automotive industry. A relatively new welding technique that has been shown to have potential for joining aluminum sheet for tailor welded blank applications is the double-sided arc welding (DSAW) process. In DSAW, an arc is struck between two welding torches situated on either side of the sheets to be welded allowing the aluminum surface oxide to be electrically cleaned simultaneously from both sides of the joint. The demonstrated potential for welding aluminum sheet and the low capital cost compared to conventional laser welding systems typically used for fabricating TWBs makes DSAW an excellent candidate for welding aluminum TWBs. The objective of the research described in this thesis was to assess the feasibility and merits of using a DSAW system to manufacture aluminum TWBs.

In this study, a DSAW system comprised of a plasma arc welding (PAW) torch above the work piece and a gas tungsten arc welding (GTAW) torch below the work piece was applied to the high speed welding of 1.0 to 1.5 mm thick AA5182-O aluminum alloy sheets in the butt-joint configuration. A series of conduction-mode DSAW welds were made in the horizontal position to identify the welding conditions that produced

good quality welds using visual acceptance criteria and with minimal geometric discontinuity across the weld. Further studies were conducted to determine the influence of the welding process parameters on the hardness, strength, ductility, formability and internal flaws of DSAW welds.

DSAW welds were made using a series of welding torch-to-work piece distances, between 1.5 and 6.0 mm, to investigate the influence of varying the relative arc forces acting on the top and bottom of the weld pool on the resulting weld bead dimensions including weld metal drop through. It was found that increasing the torch-to-work piece distance decreased the process efficiency when a constant welding power was used resulting in narrower welds being produced. Weld metal sag or drop through was not observed to be affected by varying the welding torch-to-work piece distance; however, decreasing the PAW torch-to-work piece distance to 1.5 mm was found to produce a pronounced surface ripple pattern on the top surface of the weld.

A series of DSAW welds were made to investigate the range of welding speeds and powers that produced visually acceptable welds on 1.0 to 1.5 mm thick AA5182 aluminum sheets. Welding powers ranging from 1.4 to 4.6 kW were found to produce acceptable welds at travel speeds between 10 and 70 mm/s when the net heat input per unit distance was between 60 and 110 J/mm. Above these speeds, unacceptable weld bead quality and lack of fusion defects were observed due to incomplete cathodic etching of the oxide from the surfaces and inconsistent coupling between the welding arcs the sheets. It was found that the visual appearance of the weld was improved and travel speeds could be increased for a given welding power when welding specimens were stainless steel wire brushed prior to welding to break-up and remove most of the pre-

existing hydrated aluminum surface oxide. Significant reductions in hydrogen gas porosity were also observed when stainless steel wire brushing was used.

The strength, ductility and formability of DSAW welds were found to vary significantly depending on the welding parameters used and the occurrence of porosity defects in the welds. Welds made using welding speeds greater than 30 mm/s were found to exhibit solidification shrinkage micro-porosity and a corresponding degradation in mechanical properties, especially ductility and formability. As the welding speed was further increased, degradation of the material properties continued to increase due to an increase in the quantity of micro-porosity defects in the weld. These defects caused significant strain localization resulting in a marked decrease in ductility and formability. The severity of solidification shrinkage micro-porosity present in the weld metal was found to correspond to the relative length-to-width ratio of the weld pool for all the welding conditions examined. Welds produced at high welding speeds resulted in large length-to-width ratios, a relatively large distance between the liquidus and non-equilibrium solidus and low thermal gradients in the mushy zone at the tail of the weld. These conditions are known to promote micro-porosity in alloys with a wide freezing range.

Visually acceptable DSAW welds produced using welding speeds below 25 mm/s were found to have excellent material properties that were nearly indistinguishable from the base metal with excellent ductility and formability. These welds had relatively small length-to-width ratios and little or no evidence of solidification micro-porosity, because the length of the mushy zone at the tail of the weld was much smaller and the thermal gradients were much higher. These conditions are known to prevent solidification micro-

porosity during solidification of alloys with a wide freezing range. They also provide more time and opportunity for any hydrogen bubbles that may form during solidification to float up and escape through the top surface of the weld pool thereby further reducing the propensity for hydrogen porosity.

The DSAW process has been shown to be capable of successfully producing tailor-welded blanks in 5182 aluminum alloy sheets with excellent ductility and formability provided that all sources of porosity are eliminated. This includes careful cleaning and removal of preexisting hydrated oxides using stainless steel wire brushing prior to welding to minimize hydrogen porosity and welding at slow enough speeds to prevent the formation of solidification micro-porosity at the tail of the weld pool.

Acknowledgments

Table of Contents

List of Tables

List of Figures

xiv

xvii

Chapter 1

Introduction

Aluminum alloys have been popular engineering materials for applications that demand high strength-to-weight ratios and which may also require excellent corrosion resistance. Aerospace and automation applications are excellent examples of places where aluminum is used extensively. These applications require specific material properties that make aluminum alloys the material of choice despite the high relative cost of aluminum. Automobiles present an application that could benefit significantly from the use of aluminum instead of the various steels that are currently used by the industry. An aluminum intensive midsize automobile has the potential to reduce vehicle weight by 20 percent translating to a 12 percent reduction in fuel consumption [1]; however, the relative cost and difficulty of welding aluminum compared to steel have prevented widespread use of aluminum in the automotive industry.

In recent years, climate change has become a topic of great concern across the planet. Although climate change is not well understood, some scientists are linking climate change to emissions of greenhouse gases such as carbon dioxide. This has prompted governments to target new legislation at reducing carbon dioxide emissions. Consequently, the automotive industry is under increasing pressure to improve the fleet average fuel economy of new vehicles. Increasing the aluminum content in new vehicles could be a vital way for the automotive industry to meet new fuel consumption regulations and ultimately reduce automotive carbon dioxide emissions.

Aluminum alloys have been successfully used in a variety of high performance automobiles to reduce weight and increase vehicle performance. Audi has successfully used an aluminum space frame for the past number of iterations of its A8 luxury sedan [2,3]. Meanwhile, Mazda has used aluminum body panels on its RX-8 sports car and its popular MX-5 Miata convertible. Other vehicles that now have some lightweight aluminum alloy components include the Acura NSX, Chevrolet Corvette and the Ford GT; however, widespread use of aluminum by the automotive industry will require advances in aluminum manufacturing techniques to reduce the cost barriers currently associated with using aluminum.

1.1 Tailor Welded Blanks

A tailor welded blank (TWB) is a stamping blank that consists of two or more pieces of sheet material that have been joined by welding. TWBs usually contain different material grades, gages or coatings that allow stamped components to have additional strength and corrosion resistance where they are required most. Stamping or forming operations performed on TWBs require these blanks to have high quality welds with excellent strength and ductility properties. TWBs are attractive to the automotive industry because they can generate substantial weight savings compared to traditional monolithic stamping blanks. An excellent example of how weight savings can be generated is the TWB of an automotive inner door panel made from two different gages of 5182-O aluminum alloy sheets shown in Figure 1.1. In this case, the hinge and door latch regions require additional reinforcement and have been made with 2.5 mm thick material, while the centre of the door panel does not require reinforcement and is only 1.0 mm thick. A traditional monolithic
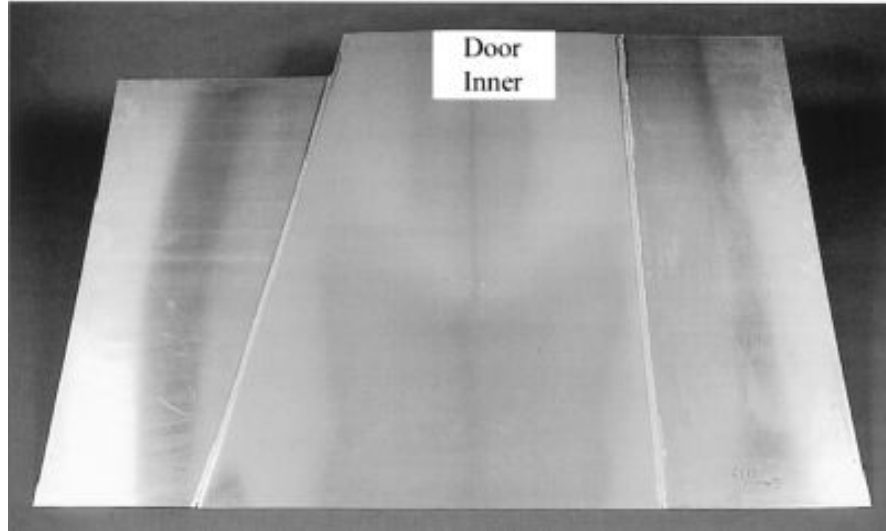
(a)
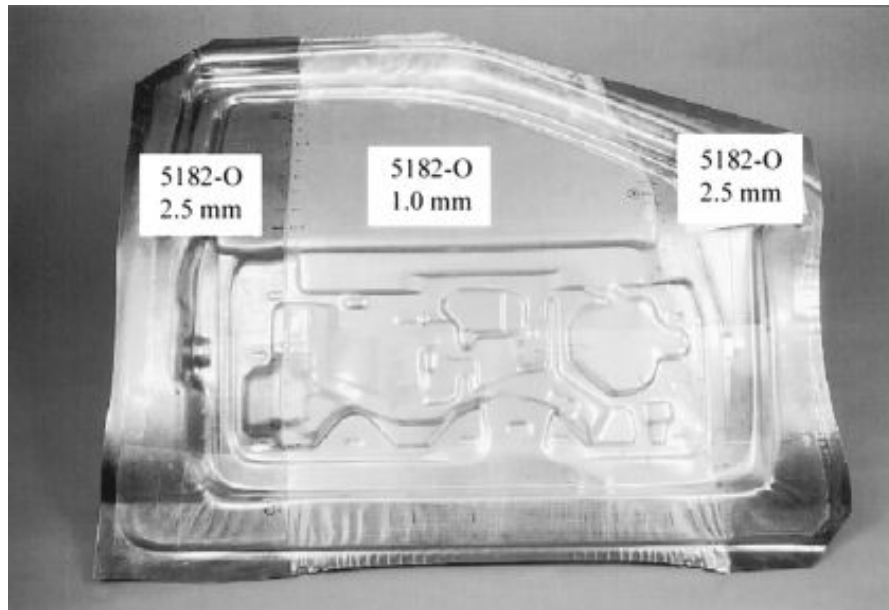
(b)

Figure 1.1: Photographs showing an aluminum TWB of an automotive inner door panel; (a) as welded, (b) after final stamping operation (taken from Davies *et al.* [4]).

blank for an inner door panel would need to be 2.5 mm thick across the entire part, which adds substantial weight to the component. Applications for TWBs also include the body side frames, centre pillar inner panels and the wheel housing or shock tower panels. If TWBs are used for all of these components, weight savings of up to 25 percent can be generated for a midsize vehicle [5]. TWBs also allow larger panels to be stamped. This reduces the number of smaller blanks and stamping dies that are required as well as the number of subsequent production steps, thereby generating substantial cost savings [4]. These benefits, combined with reduced raw material costs, have lead to a rapid increase in the use of TWBs in the automotive industry since their inception in the early 1990's [5].

The dominant materials currently used for automotive body and structural panels, including those produced from TWBs are steel alloys [5]. Steel has been used for many years in automobiles due to its relative low cost in combination with good welding and forming characteristics. Despite the increased use of TWBs, vehicles have actually been increasing in weight over the past two decades as consumers demand increased safety, comfort and convenience without sacrificing overall vehicle performance [6]. This emphasizes the importance of finding new methods to reduce vehicle weight and improve fuel economy. Otherwise, automotive companies will risk losing market share by sacrificing consumer demands in order to meet new fuel consumption targets.

The Institute for Energy and Environmental Research has compiled a series of test data for fuel consumption of vehicles. Results show that reducing a vehicle weight by 100 kg can lead to average fuel savings of 0.35 l per 100 km traveled irrespective of the vehicle size [7]. The use of aluminum in place of steel has the potential to provide significant weight reductions. As an example, Audi was able to save 194 kg by using an aluminum

body-in-white design instead of steel for their A8 sedan. The weight savings from using aluminum also allowed Audi to indirectly realize a further savings of 45 kg by decreasing the size of the engine and fuel tank required to meet the performance and design requirements for their A8 sedan [6]. Aluminum also has the advantage over steel of excellent corrosion resistance which is advantageous in cold winter climates and coastal regions where vehicles are subjected to extended salt exposure.

Aluminum alloys applicable to the automotive industry are AA5754 for structural applications, AA5182 for semi-structural and internal closure applications and 6111 for inner and external closure panels [8]. These alloys have been used in the automotive industry for their good strength-to-weight ratio and forming characteristics. For the automotive industry to maximize weight savings and minimize costs, it will be necessary that these alloys be successfully fabricated into TWBs and subsequently formed. The welding of aluminum presents several challenges which include a much higher thermal conductivity than steel, a tenacious refractory surface oxide, and sensitivity to porosity. Many of the common wrought, heat treatable alloys are subject to hot cracking and liquation during fusion welding [9]. Laser welding systems are commonly used to fabricate steel TWBs; however, aluminum has a highly reflective surface which provides poor absorption of the laser beam energy [10,11].

1.2 Welding Processes for Tailor Welded Blanks

Steel tailor welded blanks have commonly been produced with laser beam welding (LBW) processes [5]. Carbon dioxide (CO_2) gas lasers have been the laser of choice for steel TWBs, because they have high power capabilities upwards of 50 kW [11] which allow full penetration butt welds to be made at high productivity rates of up to 12 m/min [5].

5

However, CO_2 lasers have a relatively long wavelength (10.6 μm) that is readily reflected by the surface of aluminum alloys [10-12]. The high surface reflectivity of aluminum can lead to absorption levels in the range of 5 to 12 percent for a CO_2 laser. This can inhibit the formation of a stable weld pool making welding of aluminum difficult. CO_2 laser energy is also susceptible to absorption by the plasma plume created above the weld pool which can further limit the weld penetration capability of the CO_2 laser [11]. Another disadvantage is that CO_2 lasers rely on a series of lenses and mirrors for beam delivery, as the long wavelength is not compatible with fiber-optic cables [11,13]. This type of beam delivery system limits the manipulation and maneuverability of the laser beam [11].

Historically, the power output of Nd:YAG lasers have been too low to achieve high production rates required for automotive TWBs; however, modern Nd:YAG lasers have been developed with power outputs up to 4 kW [11]. The shorter wavelength of Nd:YAG lasers (1.06 μm) provides much better coupling with aluminum alloys and is not as readily absorbed by the plasma plume as CO_2 laser radiation [12]. As a result, full penetration welds can be achieved using a Nd:YAG lasers with a lower power output than a CO_2 laser. The shorter characteristic wavelength of Nd:YAG laser light can be transmitted through fiber optic cables. This feature significantly improves the positioning and maneuverability of the laser beam.

Studies have been performed to investigate the feasibility of welding automotive aluminum alloys for tailor welded blanks using both CO_2 and Nd:YAG lasers. The latter is more promising due to the enhanced absorption of laser radiation [12]; however, both processes have presented several difficulties. Deutsch *et al.* [14,15] reported that single-beam Nd:YAG laser welds on 1 mm thick 5182 aluminum alloy sheet exhibited spiky

under-bead surfaces. No combination of welding parameters could be found to eliminate this surface defect. Deutsch *et al.* [14,15] and Punkari *et al.* [16,17] reported that dual-beam Nd:YAG laser welds could be produced without surface defects on 1 mm thick 5182 and 5754 aluminum alloys using total welding powers of 4.5-5.0 kW and travel speeds of 6-7.5 m/min.

The high energy density typical of laser beams has been reported to cause loss of alloying elements, such as magnesium, by vaporization during CO_2 laser welding [18,19]. Moon and Metzbower [18] reported that the loss of magnesium contributed to a loss in strength in aluminum alloy 5456 since this alloy derives its strength through solid solution strengthening from additions of magnesium. Porosity is another problem that has been reported in laser welding of aluminum alloys. Pores have been reported to be caused by hydrogen gas and occluded vapour pores from magnesium vapours trapped in the weld pool during solidification [15,17,19,20]. Keyhole instability and the generation of occluded vapour pores has also been found to contribute to porosity when welding aluminum alloy sheet [15,19].

Friction stir welding (FSW) is a solid-state welding process that uses a rotating tool that provides frictional heating and mechanical deformation to form a weld. In FSW, a thermomechanically affected stir zone is created along the weld centerline with a narrow heat affected zone beyond the stir zone. The absence of a fusion zone in FSW has been shown to produce high quality welds with improved mechanical properties compared to fusion welding processes [21]. TWBs produced with FSW have been shown to have weld metal with strength and elongation properties comparable to the base metal for non-heat treatable aluminum 5182 and 5754 alloys [21,22]; however, welding speeds attainable with

FSW for TWB applications presently fall below 1 m/min which is inadequate to deal with high production volumes in the automotive industry. As a result, FSW will require significant productivity advances before it will be a viable process for producing TWBs.

Variable Polarity Plasma Arc Welding (VPPAW) and Double-Sided Arc Welding (DSAW) are the highest energy density arc welding processes that are also suitable for welding aluminum alloy sheet. They are the only arc welding processes that have the potential to achieve the high productivity rates required for manufacturing aluminum TWBs. Both of these processes use a square-wave alternating current power supply that cleans the tenacious oxide layer from the surface by cathodic etching [23].

The feasibility of applying VPPAW to the manufacture of TWBs has been investigated by Deutsch [14] and Punkari [16] using 1.6 mm thick AA5182 and AA5754 aluminum sheet. A maximum welding speed near 3 m/min was reported, which was limited by the arc's ability to clean the surface oxide at high speed [14]. A downside to the VPPAW system is the requirement of a stainless steel backing bar to control the under-bead geometry and the inability to clean the under-bead oxide because the arc is not in contact with the under-bead surface. If the oxide layer is not removed through the entire sheet thickness, an oxide inclusion can occur causing a crack-like lack of fusion defect on the underside of the weld. Punkari [16] found that a substantial welding power was required to prevent oxide inclusions which resulted in wide welds with noticeable sagging or drop through. The lower energy density of the VPPAW system also resulted in welds that lacked symmetry through the material thickness resulting in unfavorable angular distortion of the sheets.

Double-sided arc welding, shown schematically in Figure 1.2, is a relatively new arc welding process, that was patented by Zhang and Zhang [24] in 1999. The DSAW process uses PAW and gas tungsten arc welding (GTAW) torches connected directly to the two terminals of a single power supply. The torches are positioned on opposite sides of the work-piece such that the welding current flows from one torch through the work-piece to the opposite torch. Zhang *et al.* [25-28] have reported that keyhole-mode DSAW increased productivity and produced welds with higher depth-to-width ratios than traditional arc welding processes when welding thick plate sections (5 to 12 mm) of stainless steel and aluminum alloys.

In recent studies, Kwon and Weckman [29-31] and Anousheh [32] investigated the feasibility of applying DSAW to conduction-mode welding of AA5182 aluminum sheet ranging in thickness from 1.0 to 1.2 mm. It was noted that the opposing welding torches successfully cleaned the oxide from both sides of the joint and produced visually acceptable welds at speeds up to 3.6 m/s. Lack of fusion defects previously reported to be a problem with PAW by Punkari [16] were not observed with DSAW welds. Through thickness heating was more uniform with DSAW than with VPPAW allowing symmetric welds to be produced with minimal angular distortion of the sheets. The demonstrated potential for welding aluminum sheet and the low capital cost compared to laser welding systems makes DSAW an excellent candidate for welding aluminum TWBs; however, research to date has been limited to DSAW of similar thickness welds and the mechanical properties of these welds have not been characterized. Furthermore, the post weld forming properties, that are vital for TWB applications, have not been characterized for 5182 aluminum alloy sheets welded with the DSAW process.

PAW TORCH

Tungsten Electrode

Copper Plasma Gas Cup

Plasma Gas

Shielding Gas

C̶L̶

Shielding Gas Cup

Weld Pool

Base Metal

Variable Polarity Welding Current

Shielding Gas Cup

C̶L̶

Tungsten Electrode

Shielding Gas

GTAW TORCH
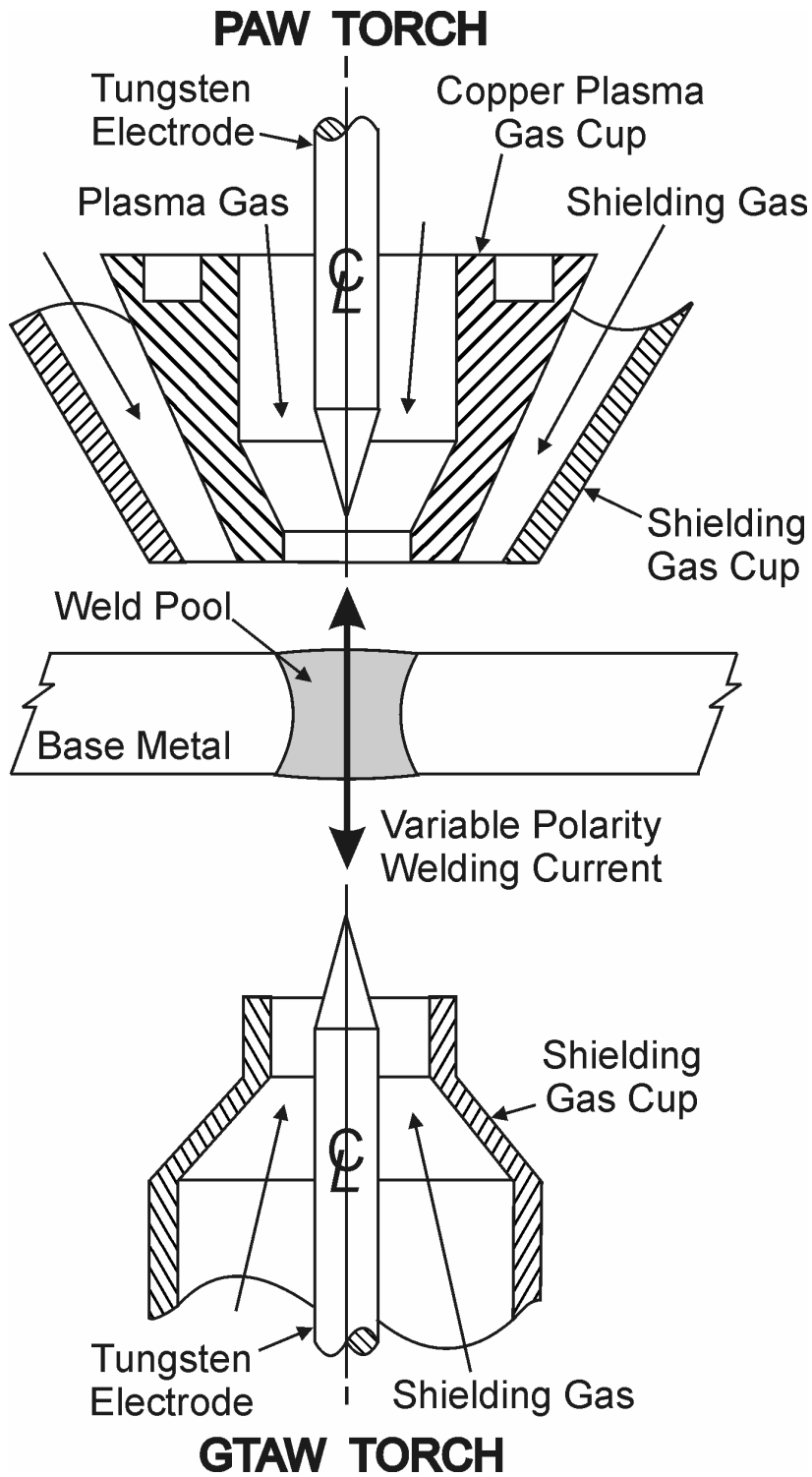
Figure 1.2: Schematic diagram showing the torch and work-piece configuration in DSAW (taken from Kwon [29]).

1.3 Research Objectives

The main objective of the present study was to examine the feasibility of applying double-sided arc welding to the manufacture of automotive aluminum tailor welded blanks. The specific objectives of the research were as follows:

1) Optimize the welding parameters to minimize stress concentrating geometric discontinuities of the weld bead that could limit the post-weld formability.

2) Identify and characterize the range of suitable welding conditions for joining and forming of dissimilar thickness 5182 aluminum alloy sheets.

3) Characterize the mechanical properties of the optimized double-sided arc welds with particular emphasis on the strength, ductility and formability of the weld metal.

1.4 Thesis Organization

This thesis is focused on investigating the feasibility and merits of using a double-sided arc welding system to manufacture aluminum tailor welded blanks. A literature review is presented in Chapter 2 detailing knowledge of GTAW and PAW as it pertains to DSAW of aluminum alloys. Literature applicable to the weld bead geometry and the mechanical performance of aluminum welds is also examined. The experimental equipment and procedures used in this research are presented and described in Chapter 3. Experimental results and corresponding discussions for optimizing DSAW weld bead geometry, identifying the range of welding conditions suitable for welding TWBs with DSAW and characterizing their mechanical properties are presented in Chapter 4. Finally, Chapter 5 summarizes the key findings of this research and proposes the direction for future work.

Chapter 2

Literature Review

2.1 Gas Tungsten Arc and Plasma Arc Welding

A schematic diagram of the Gas Tungsten Arc Welding (GTAW) process is shown in Figure 2.1a. This process utilizes the heat from an electric arc between a non-consumable tungsten electrode and a work-piece to melt and join two pieces of metal. GTAW is known for its ability to produce high quality welds with a variety of materials including reactive metals such as aluminum and magnesium alloys [13,23]. An inert shielding gas (commonly argon or helium) protects the weld pool and the electrode from contamination and oxidation. GTAW can be performed using either direct current electrode negative (DCEN) for maximum penetration, direct current electrode positive (DCEP) for cathodic cleaning of refractory oxides or alternating current (AC) for a balance of penetration and cathodic cleaning [23]. Alternating current is the typical current choice for aluminum alloys whose tenacious refractory surface oxides can lead to fusion defects if not removed during welding.

In 1957, Robert Gage of Union Carbide invented Plasma Arc Welding (PAW) when he discovered that the characteristics of the GTAW process could be substantially changed by constricting the arc [33]. A GTAW and PAW torch are shown schematically in Figure 2.1b. A PAW torch uses a water-cooled copper nozzle with an orifice to constrict the welding arc producing a collimated, high velocity plasma jet and welding arc [13,23,33]. The constriction increases the current density which in turn increases the
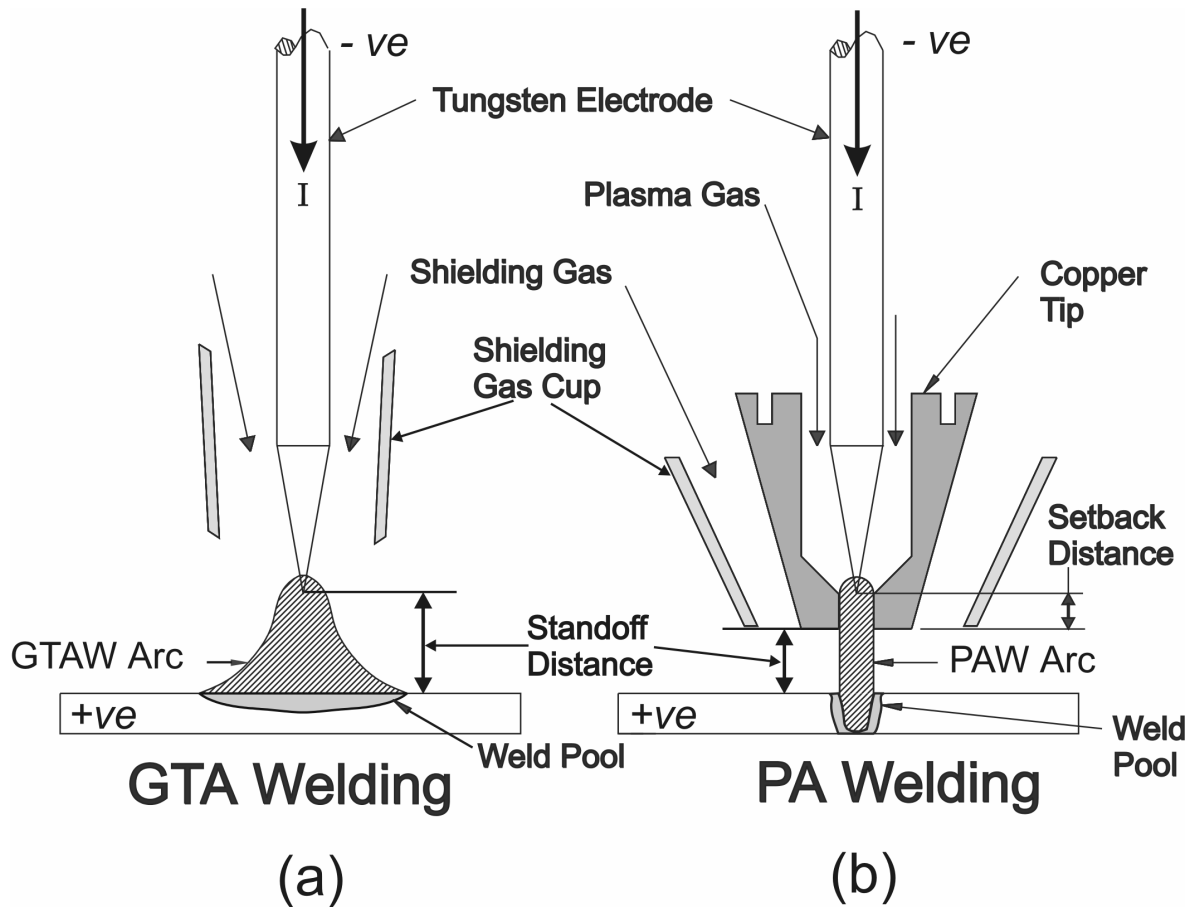
Figure 2.1: Comparison of GTA and PAW welding torches showing arc and weld pool profiles: a) GTA welding and b) PA welding (taken from Deutsch [14]).

energy density and the arc temperature. This allows deeper penetration and higher welding speeds to be achieved compared to GTAW. Unlike GTAW, PAW can be performed in either conduction mode or keyhole mode. The plasma jet is also relatively stiff in PAW, minimizing the effect of the torch-to-work-piece distance and reducing the susceptibility of the arc to deflection caused by low strength magnetic fields.

2.1.1 Arc Physics and Cathodic Cleaning of Oxides

The welding arc is created by a flow of current between a negative electrode known as the cathode to a positive electrode known as the anode. This flow of current causes heating and ionization of the shielding gas used resulting in a superheated mixture of ionized gas and electrons that can reach temperatures as high as 30 000 K [34]. Three distinct regions have been observed in a welding arc; the anode fall region, the cathode fall region, and the arc or plasma column [34]. Each region has a voltage drop associated with it as shown in Figure 2.2. Non-linear voltage drops are observed across the narrow anode and cathode fall regions as a result of thin space charge layers comprised of high electron concentrations in the anode fall region and high concentrations of positive ions in the cathode fall region [34]. The arc column, located between the anode and cathode fall regions, is comprised of neutral and charged particles that conduct the welding current. The voltage drop in the arc column varies linearly with its length [34].
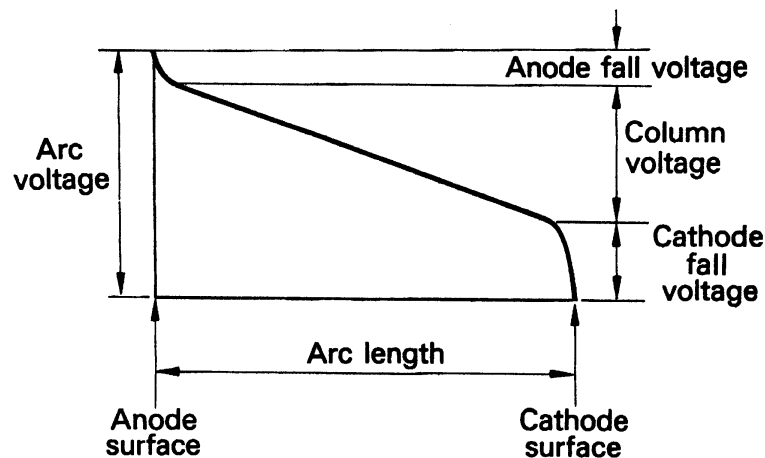
Figure 2.2: Schematic showing the voltage distribution across the welding arc (taken from Lancaster [34]).

14

Significant heating caused by the condensation of electrons occurs at the anode surface. This heating is caused by the transfer of electron potential energy as well as kinetic and thermal energies that the electrons pick up while crossing the arc [34]. As a result, 70% of the arc heating occurs at the anode [23]. For this reason DCEN is preferred to maximize heat input and penetration to the work-piece (anode) in non-consumable electrode processes such as GTAW and PAW.

Cathodic cleaning is the stripping of refractory oxides from metal surfaces, such as aluminum alloys, that occurs with electrode positive polarity when the work-piece is the cathode [35]. Several theories exist to explain the cause of cathodic cleaning; however, the mechanism responsible is under debate by researchers [35-37]. Sputtering of the oxide layer by cathode streamers (a stream of positive ions) has been proposed by Correy [36] as one mechanism of oxide removal. The cathode streamers are transient in nature with a life span on the order of one millisecond during which a small piece of oxide is removed from the metal surface. Cathode streamers preferentially travel along surface scratches and do not tend to jump across surface scratches on a material.

Pang *et al.* [37] have proposed a second theory of cathodic cleaning. They suggest that a high electrostatic field is formed by a collection of positive ions on the surface of the oxide layer [34,35,37] and that the thin electrically insulating oxide layer is broken up by electrons which tunnel through the oxide layer to form an emission site. The electron tunneling causes small vapour jets to form which strip off the oxide from the work-piece generating an oxide free cathode surface.

2.1.2 Conduction and Keyhole Welding Modes

Two classifications exist to identify the mode of welding; conduction and keyhole, as shown in Figure 2.3a and b, respectively. Conduction mode welds occur when the heat imparted to the work-piece is high enough to cause melting, but insufficient to cause significant vaporization of the material. Conduction mode welds are typically characterized as welds with an ideal depth-to-width ratio of 0.5 that exhibit near semi-circular cross sections.

Keyhole-mode welds have high depth-to-width ratios and can be produced by high energy density welding processes such as PAW and LBW. In PAW, the high energy density in combination with a focused plasma jet can produce a vaporized "keyhole" allowing deep, narrow welds to be produced as shown in Figure 2.3b. Molten metal flows around the edge of the keyhole and solidifies at the trailing edge of the weld. Full penetration welds made with keyhole-mode welding tend to be narrower with fusion boundaries straight through the sheet compared to the semi-circular, non-symmetric conduction-mode welds. This helps to minimize weld distortion. Keyhole-mode welding is also common with high energy density laser and electron beam welding processes; however, in the absence of a plasma jet, these processes form "keyholes" strictly through the vaporization of material under the intense energy beams.

2.1.3 Variable Polarity GTAW and PAW

Modern welding power supplies have been developed to produce controllable and stable square-wave alternating current waveforms. These power supplies are ideally suited to welding of aluminum and other reactive metals with the GTAW and PAW processes and
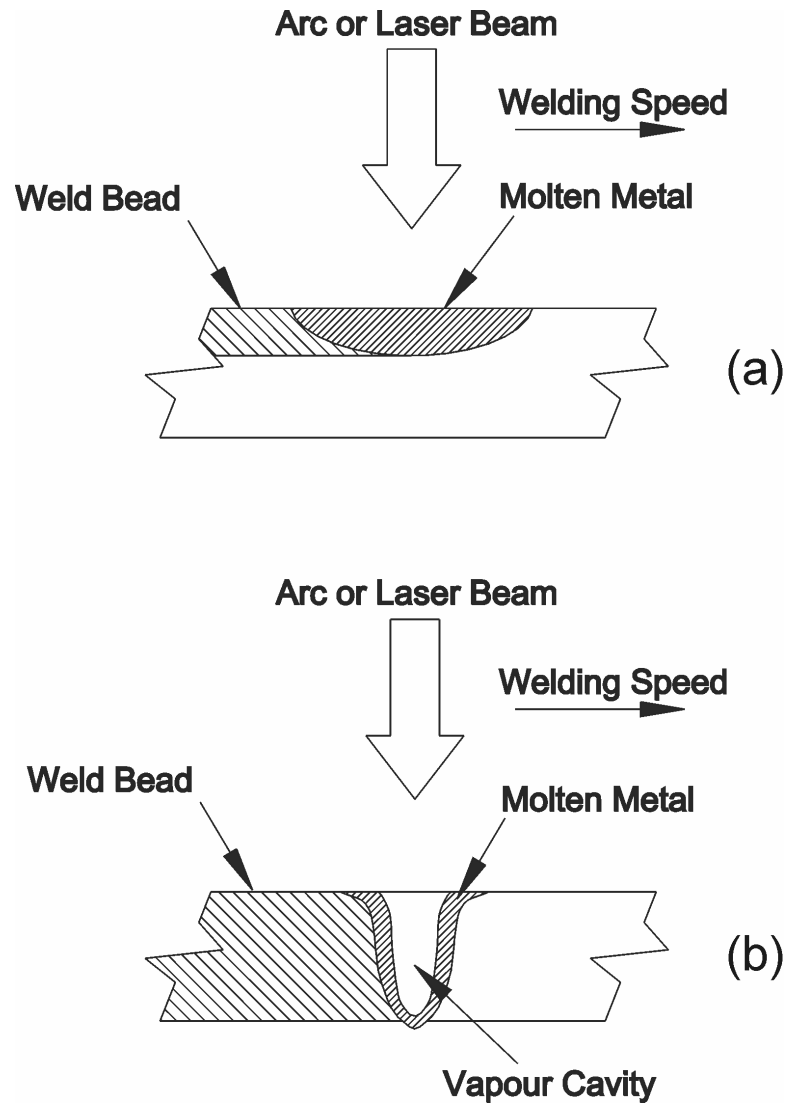
Figure 2.3: Welding modes in PAW and GTAW: a) conduction mode and b) keyhole mode (taken from Punkari [16]).

have several benefits over older sinusoidal AC power supplies. Variable polarity square waveforms do not exhibit the gradual reversal in polarity that causes poor re-ignition of the next half-wave (due to the loss of conductive, ionized plasma gases in the arc) that is common with sinusoidal waveforms [23]. As a result, variable polarity square wave power supplies significantly improve the arc stability in AC welding applications. Variable polarity square waveforms also offer a great deal of adjustability as shown in Figure 2.4.
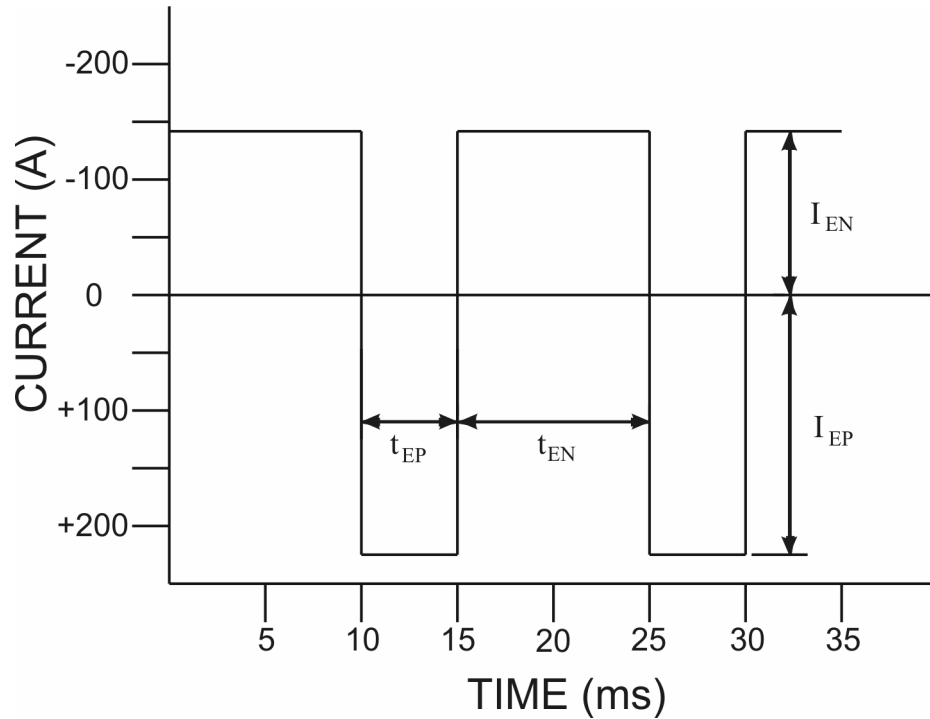
Figure 2.4: Variable polarity square waveform showing the adjustable parameters (taken from Kwon [29]).

These power supplies allow the relative amount of cathodic cleaning to be controlled by adjusting the fraction of time spent in electrode positive, t_{EP}, and the magnitude of the electrode positive current, I_{EP}. The penetration can be controlled by adjusting the fraction of time spent in electrode negative, t_{EN}, and the magnitude of the electrode negative current, I_{EN}. These adjustments allow optimization of the waveform to obtain good oxide cleaning of aluminum alloys while simultaneously increasing the welding speed by maximizing the heat input to the weld.

The non-dimensional parameters θ and β, defined in Equation 2.1 and 2.2, were first introduced by Fuerschbach and Knorovsky [35] to define the fraction of time spent in electrode negative and the electrode negative polarity fraction, respectively. The polarity balance, defined in Equation 2.3 is the fraction of electrode negative polarity power to the

total arc power where $Q_{EN} = I_{EN}V_{EN}(1 − \theta)$ and $Q_{EP} = I_{EP}V_{EP}\theta$. Increasing θ and β will increase the heat input to the work-piece, while decreasing θ and β will increase the cathodic cleaning [14,15,29,35].

$$\theta = \frac{\left|I_{EN}\right|}{\left|I_{EN}\right| + \left|I_{EP}\right|} \tag{2.1}$$

$$\beta = \frac{\left|t_{EN}\right|}{\left|t_{EN}\right| + \left|t_{EP}\right|} \tag{2.2}$$

$$Polarity\ Balance = \frac{Q_{EN}}{Q_{EN} + Q_{EP}} \tag{2.3}$$

2.1.4 GTAW and PAW Variables

The welding variables that directly affect the process in GTAW, shown in Figure 2.1a are: the magnitude and type of the welding current, torch standoff, electrode geometry, and shielding gas type and flow rate. In addition to the GTA variables, PAW has its own unique variables shown in Figure 2.1b which include the electrode setback, orifice diameter, and the orifice gas type and flow rate. Additional variables applicable to variable polarity GTAW and PAW include the AC frequency, θ, β and polarity balance.

The welding current, I, has a direct impact on the welding power (P = I·V), the weld size and penetration. Electrode negative polarity results in higher heat input to the work-piece, while electrode positive polarity results in higher heat input to the electrode [23]. The positive electrode, or anode, in the welding arc experiences greater heating due to the condensation of electrons which transfer the kinetic, potential and thermal energy of the electrons to the anode [34].

The standoff distance is defined as the electrode-to-work-piece distance and the orifice-to-work piece distance in GTAW and PAW, respectively. The standoff distance has a direct influence on the arc voltage. Increasing the standoff will increase the arc voltage for a constant current process which in turn increases the welding power and therefore, the size of the weld pool. However, reduced arc efficiency has been reported with increased arc voltages [38]. This suggests an increase in welding power by the arc voltage will have a lesser effect than a similar increase in power by increasing the welding current.

Welding arcs have been shown to have heat and current densities that closely fit normal or Gaussian distributions [39,40]. Increases in the standoff distances or arc gaps tend to cause the arc to spread which increases the width of the arc and decreases the heat and energy densities impinging on the surface of the weld pool [34,39,40].

Inert shielding gases such as argon or helium are used for GTA and PAW. Helium gas has a higher ionization potential compared with argon which results in higher arc voltages, a hotter arc and greater heat transfer to the work-piece. In PAW, the higher ionization potential of helium tends to limit the welding current flow to the ionized stream of plasma gas [41]. This prevents arc spreading and produces higher energy densities than are observed when using argon shielding gases. As a result, helium has proven to be beneficial for keyhole-mode VPPAW of aluminum plate [42]. However, it was reported by Punkari [16], that helium shielding gases used with VPPAW of aluminum sheet lead to significant undercutting of the weld bead. Shielding gas flow rates should be sufficient to prevent atmospheric air from reaching the weld pool, but not so excessive that atmospheric air and oxygen can be drawn into the shielding gas shroud by turbulent flow. High purity

argon is used for the orifice gas in VPPAW because its lower ionization potential provides excellent arc stability [33].

2.2 Double-Sided Arc Welding

Double-sided arc welding (DSAW) is a variation of GTAW or PAW in which two welding torches are connected to a common power supply. The most common DSAW configuration uses a PAW torch opposing a GTAW torch as shown in Figure 1.2. The welding circuit is completed by two welding arcs allowing the current to flow between the electrodes via the workpiece. DSAW was originally developed by Zhang *et al.* [24-28] to produce keyhole-mode welds in plain carbon steel, stainless steel and aluminum alloy plates ranging in thickness from 5 to 12 mm.

In conduction or keyhole-mode PAW, the current flowing across the arc grounds through the surface of the work-piece with very little current flow entering the keyhole [43]. In DSAW, it has been proposed that two current paths exist; the current can pass through the work-piece as with traditional arc welding processes or in keyhole DSAW, the current can take a unique path through the keyhole [27]. For conduction-mode DSAW, the current must flow through the material. In this case, the voltage drop between the two welding torches, shown schematically in Figure 2.5, is given by [27]:

$$V = V_{EC} + V_{C1} + V_{WA} + V_{WC} + V_{C2} + V_{EA} \qquad (2.4)$$

where V_{EC} is the cathode fall voltage for the gas tungsten electrode, V_{C1} is the gas tungsten arc column fall voltage, V_{WA} is the voltage drop across the anode fall region adjacent to the workpiece, V_{WC} is the voltage drop across the cathode fall region adjacent to the workpiece, V_{C2} is the plasma arc column fall voltage, and V_{EA} is the plasma arc electrode
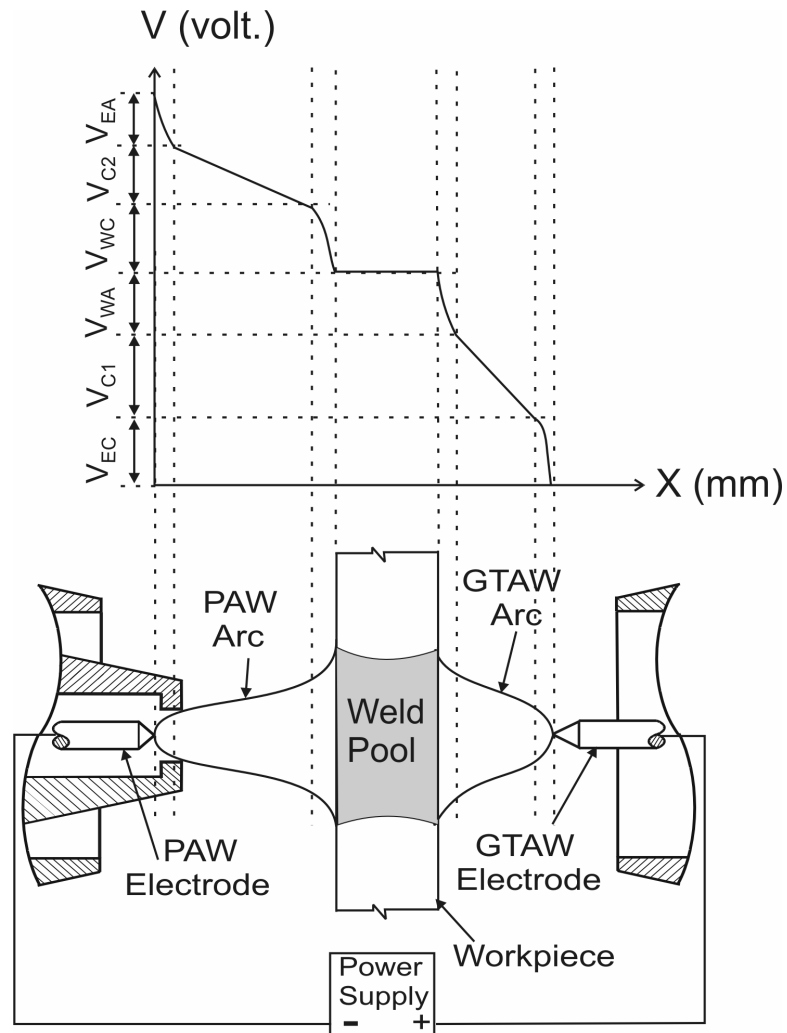
Figure 2.5: Schematic showing the voltage drop between the DSAW torches (taken from Kwon [29]).

anode fall voltage. If the work-piece thickness and resistivity are high, as with steel plates, a measurable voltage drop will also exist across the work-piece.

2.2.1 DSAW of Aluminum Plate

Keyhole-mode DSAW of aluminum alloy plates has been studied and compared to GTAW and VPPAW by Zhang *et al.* [25,44-46]. A variety of welds were produced on mild steel,

stainless steel and aluminum alloy plates with thickness ranging from 5 to 9.5 mm. They reported that increased penetration could be achieved at higher welding speeds than traditional GTAW or PAW. The depth-to-width ratio of the welds increased while the size of the heat affected zone decreased. Increased symmetry through the material thickness, beneficial in reducing post weld distortion, was also reported. The main disadvantage with DSAW is the requirement to access both sides of the weld joint which is not always practical or possible [25].

Zhang *et al.* [25,45] have conducted studies using DSAW to weld 6.4 mm thick 2024, 5052 and 5454 aluminum alloy plates in the flat position. Full and partial penetration welds made using DSAW and VPPAW were compared. It was found that the solidification structure in the partially penetrated welds was completely columnar while the fully penetrated welds exhibited a beneficial columnar-to-equiaxed grain transition at the center of the welds. It was shown that full penetration welds produced with DSAW on 2024 aluminum plate had a finer grain structure in the heat affected zone than full penetration welds made with PAW. The columnar grain structure was also reported to be finer in the welds produced with DSAW. The double-sided arc welds in 5454 aluminum showed no loss in strength compared to the annealed base metal while the ductility was slightly lower than the base metal. The strength and ductility of the welds made with DSAW were slightly better than welds made with PAW, the difference being attributed to the finer grain structure in the doubles-sided arc welds [25,45].

DSAW of 6061 aluminum plate in the vertical-up progression has also been investigated by Zhang *et al.* [44,46]. Welds made with DSAW using the dual GTAW configuration were compared to welds made with VPPAW. It was reported that crack-free

autogeneous welds could be produced using DSAW in the notoriously crack sensitive 6061 aluminum alloy. Crack free welds with VPPAW could not be produced. The double-sided arc welds had a fusion zone comprised of a 70% equiaxed grain structure surrounded by a small columnar region along the fusion boundary. This was notably different from the fusion zone in welds made with PAW which had an 80% columnar grain structure. Fracture surface analysis indicated that the double-sided arc welds with a dimpled, ductile fracture surface had better toughness than the plasma arc welds that failed along the columnar grain boundaries. The improved toughness and decreased crack susceptibility of double-sided arc welds was attributed to the finer equiaxed grain structure. Zhang *et al.* [46] have suggested that the increase in equiaxed grains observed with DSAW could be a result of fluid flow that causes stirring in the weld pool. It has been proposed that fluid flow could be driven by electromagnetic forces caused by the unique current flow through the work-piece; however, this claim has not been verified.

2.2.2 DSAW of AA5182 Aluminum Sheet

The feasibility of applying DSAW to welding aluminum sheet was first studied by Kwon and Weckman [29,30,31]. Conduction-mode butt welds were produced in the flat position using a DSAW system that utilized a PAW torch above and a GTAW torch below the sheets to be welded. The effects of parameters θ and β (with respect to the PAW torch) were studied on 1.15 and 1.2 mm thick 5182 aluminum alloy sheet. Optimal welding conditions were found when θ and β were both set to a value of 0.5. Values of θ and β below 0.5 resulted in poor cathodic cleaning on the bottom (GTAW) side of the weld while values greater than 0.5 led to insufficient cleaning of the top (PAW) side of the weld. It was reported that DSAW was well suited to welding aluminum sheet and good welds could

be achieved at speeds up to 60 mm/s (3.6 m/min) using a total welding power of 3.4 kW [29]. Upper limits on welding speed were shown to be limited by the ability to remove surface oxides rather than the ability to achieve full joint penetration [31].

Anousheh [32] studied the effects of varying torch configurations on DSAW of aluminum sheet to optimize the weld bead geometry. Welds produced with the PAW and GTAW torches positioned above and below the specimens respectively were compared to welds produced with the torches reversed (i.e., PAW torch below and GTAW torch above the work-peice). The torch configuration did not have a detectable difference on the weld bead appearance, drop through or underfill. Weld metal drop through was reported to be reduced with higher welding speeds for a given welding power [32]. Staggering the welding torches to have the PAW torch leading (above the work-piece) and GTAW torch trailing (underneath the work-piece) was reported to reduce weld metal drop through. However, this configuration also substantially increased the volume of hydrogen porosity observed in the DSAW welds. [32].

2.3 Weld Bead Geometry

Weld pool convection or fluid flow, driven by four distinct forces including buoyancy force, electromagnetic Lorentz forces, surface tension force and aerodynamic drag forces from the arc plasma, have been shown to influence the weld pool shape and resulting weld bead geometry of GTAW and PAW welds [47,48]. It has been reported, however, that the weld pool dimensions in high thermal conductivity metals such as aluminum alloys are not significantly influenced by fluid flow [49]. For this reason, the weld bead geometry in flat position DSAW is most likely to be influenced by the forces acting on the molten weld pool rather than fluid flow during welding.

The current flowing between the electrode and work-piece in an arc welding process generates a circumferential magnetic field. The interaction between the current flow and the magnetic field produces a body force known as the Lorentz force which acts towards the centre of the welding arc, constricting the arc plasma [48]. The pressure of the arc plasma opposes the Lorentz force creating an equilibrium condition. The arc divergence between the electrode and work-piece, in GTAW and PAW, cause higher current densities at the electrode than at the work-piece. This causes static gas pressures at the electrode to exceed those at the work-piece creating a plasma jet that flows towards the work-piece. Plasma jets have been found to have velocities up to 120 m/s in GTAW and 320 m/s in PAW [50]. A stagnation pressure is exerted on the work-piece from the impinging plasma jet which is more commonly referred to as the arc pressure or arc force [48]. The arc force is generally believed to be the cause of surface depression of the weld pool experienced during welding and to contribute to fluid flow in the weld pool [51-53].

Measurements of arc forces in GTAW was first performed by Converti [54], who found that the arc force was proportional to the square of the welding current. He reported that the arc force could be determined using:

$$F = \frac{\mu_o I^2}{8\pi}\left(1 + 2\ln\frac{R_2}{R_1}\right)$$ (2.5)

where I is the welding current, μ_o is the permeability of free space, R_1 is the radius of the arc where it contacts the welding electrode, and R_2 is the radius of the arc where it contacts the work-piece. Burleigh and Eager [51] reported that their measurements of arc forces using a variety of work-piece materials were in agreement with the arc force predicted in Equation 2.5.

Weld pool depression has been shown to be extremely small at welding currents below 200 to 240 amperes, while beyond this threshold, the weld pool depression increases quadratically with increasing current [52,55]. In their study of weld pool depression, Rokhlin and Guu [52] reported, that beyond the threshold current the weld pool depression was reported to have a linear relationship with arc force. The measured arc force was found to be equivalent to 20% of the sum of the surface tension and gravitational forces acting on the weld pool. It was concluded that the arc force could not solely account for the GTAW pool depression and that electromagnetic forces must also influence the surface depression.

In DSAW, the weld pool is subject to arc forces on both sides of the welding joint as shown in Figure 2.6. The characteristic full penetration welds produce a square molten weld pool through the material thickness. It can be clearly seen that the molten weld pool is subjected to an arc force from the top torch which is acting with gravity to produce a sag in the bead geometry known as drop through. Combating the weld pool drop through are the arc forces from the lower torch and surface tension between the molten weld pool and the un-melted base metal.

Anousheh [32], investigated the effect of varying the DSAW torch stand off distances and configuration to minimize the weld metal drop through observed during welding. As no literature exists pertaining to the arc forces and pool depression in PAW welds, it was thought that the increased plasma jet velocities could produce higher arc forces. Anousheh [32], compared welds made using 60 amperes with a PAW torch above a GTAW torch to welds made with a GTAW torch above a PAW torch. It was concluded
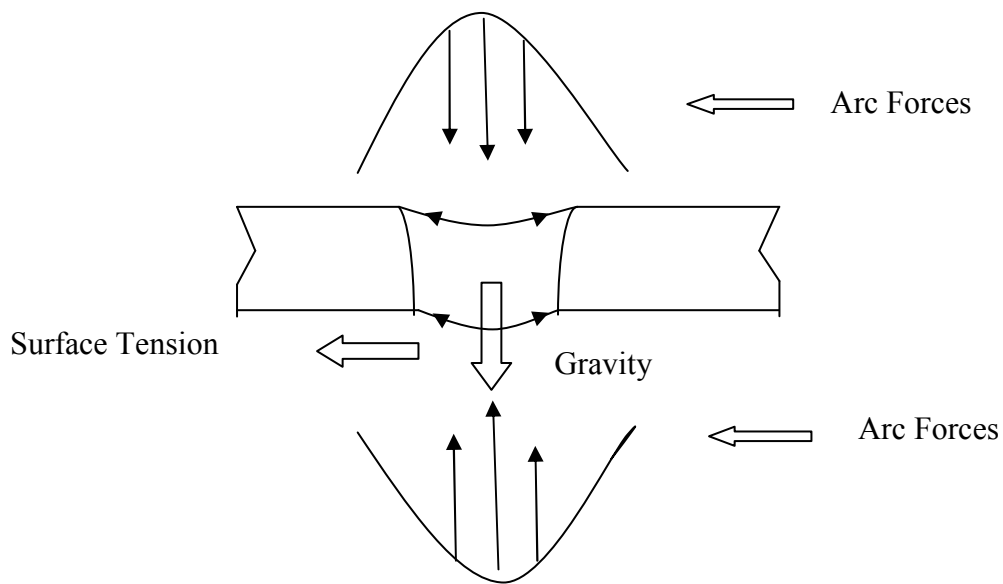
Figure 2.6: Schematic illustration of the forces acting on the weld pool in DSAW (taken from Anousheh [32]).

that the torch configuration did not produce a significant change in the weld bead geometry. It was reported that the most successful method for reducing the weld metal drop through was to reduce the heat input to the weld and hence minimize the volume of molten metal subjected to gravity. In these experiments, equal standoff distances were used for the PAW and GTAW torches. The arc force relationship in Equation 2.6 indicates that increasing the diameter of the arc on the work-piece (R_2) will tend to reduce the arc force. As noted previously, the welding arc tends to widen with increased standoff [39] which suggests that increasing the standoff should decrease the arc force. This is in agreement with work by Savage *et al.* [56] who reported that the arc force against a plate surface is inversely proportional to the electrode-to-work distance. For this reason, it is feasible that increasing the standoff distance for the top welding torch, in the DSAW

welding process while simultaneously decreasing the standoff for the bottom torch could result in a force balance that minimizes gravitational effects on the DSAW weld bead.

2.4 Mechanical Properties of Welded Aluminum Alloys

Numerous studies have been conducted to characterize the mechanical properties of aluminum welds in structural sections as well as automotive sheet metal applications. It has generally been concluded that sound welds can be achieved with yield and ultimate tensile strengths comparable to the strength of the base or filler metal [29,57,58]. Kwon [29] reported weld strengths in excess of 90% of the base metal strength for welds on 5182-O aluminum alloy sheet. Ashton *et al.* [57] also reported minimal loss in strength in their work with aluminum alloy 5086. They reported that no significant loss in strength was observed even in welds containing 1 to 2% porosity by volume. Above the 1 to 2% porosity threshold, decreases in strength have been reported that have been found to be directly proportional to the loss in cross sectional area of sound material [58]. Welds with a few large pores were found to have comparable strengths to welds with the same reduction in cross section area as welds containing numerous small pores.

Porosity has been shown to have much more devastating effects on the weld metal ductility than it does on the strength. Ashton *et al*. [57] found that a 4% volume of porosity reduced the strength of their welds by 17% while decreasing ductility by 51%. They also observed that the ductility was reduced in welds with less than 1% porosity by volume despite no observable decrease in strength. Shore and McCauley [59] also reported that low levels of porosity reduced the ductility in aluminum welds. This differed from their previous work with mild steels that could tolerate 5 to 7% porosity without impacting the mechanical properties.

TWBs produced with ferrous alloys typically have weld strengths greater than the base metal causing the suppression of plastic deformation in the vicinity of the weld allowing the forming behaviour to approach that of the base metal [60]. Formability in aluminum TWBs has a greater dependence on weld defects because aluminum alloys do not exhibit weld strengthening to the same extent as ferrous alloys [61]. The influence of welding defects, namely surface roughness and weld porosity, on strain localization in aluminum TWBs has been studied by Bayley and Pilkey [61]. It was found that the amplitude of surface defects had a much greater influence on strain localization than the wavelength of the surface defects. Porosity was reported to produce a greater reduction in the failure strain than a surface defect of a similar size with pores close to the weld centerline having a greater influence than pores further from the weld centerline. Clearly, minimizing porosity will be vital to preserve the weld metal ductility and formability to allow successful forming of aluminum TWBs.

2.4.1 Formation of Hydrogen Porosity

The stark difference in solubility of hydrogen between liquid and solid aluminum is generally accepted to be the cause of most porosity observed in aluminum castings and welds [62-65]. Porosity is produced in two ways; rejection of hydrogen at the solid-liquid interface can produce interdendritic gas pores in low to moderately supersaturated liquid or the nucleation of gas bubbles ahead of the solid-liquid interface can occur in highly supersaturated liquids [62]. The shape, size and growth rate of cellular-dendrites will determine the shape and size of interdendritic porosity while surface tension and diffusion will control the growth and size of gas bubbles formed ahead of the solidification front [64]. Hydrogen gas bubbles are buoyant and tend to float towards the surface of the weld;

30

however, a large number of the gas bubbles will not reach the surface before the weld solidifies. Fluctuations in the solidification rate have been reported to cause bands of porosity in aluminum welds [66]. A rapid increase in the solidification rate can freeze a band of recently formed gas bubbles at the solid liquid interface before they migrate towards the center of the weld. This simultaneously depletes the number of hydrogen bubbles at the solid-liquid interface promoting the solidification of a band without any pores.

Hydrogen in a molten weld pool can come from a number of sources including: hydrocarbon based oils and greases (from prior material processing), water or moisture absorbed by the aluminum surface oxide, hydrated aluminum oxides ($Al(OH)_3$) that form during extended material storage in humid environments, moisture contamination in the shielding gas, and dissolved hydrogen in the base or filler metals [65]. Moisture and greases are especially problematic as they are rapidly vaporized in the arc and subsequently converted to atomic hydrogen that is readily absorbed by the weld pool [64]. Moisture from the faying surfaces of the base metal can be trapped in the weld pool during welding. This entrapped moisture can undergo several common reactions including:

$$2Al + 3H_2O \rightarrow Al_2O_3 + 3H_2 \qquad\qquad (2.6)$$

$$Mg + H_2O \rightarrow MgO + H_2 \qquad\qquad (2.7)$$

$$Al_2O_3 \cdot H_2O + Mg \rightarrow MgAl_2O_4 + H_2 \qquad\qquad (2.8)$$
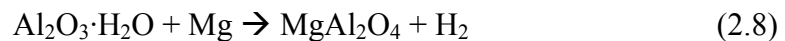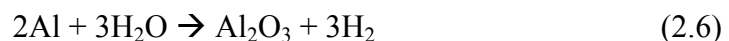
to produce hydrogen in the weld pool [64]. Equation 2.6 shows the reaction between aluminum and water, Equation 2.7 can occur in aluminum alloys with magnesium additions, and Equation 2.8 shows a third reaction that can occur between chemically combined water or water of hydration if temperatures exceed 815°C [64].

Models of hydrogen absorption by the weld pool indicate that gas pickup takes place over an annular area of the weld pool [62]. The center of the pick up region is at or close to the boiling point of the metal as this is the location of maximum arc heating. High aluminum vapour pressure in this region suppresses the absorption of hydrogen gas. The gas absorption increases outside of the central area due to lower temperatures of the molten metal. Further from the center, a maximum absorption region will exist beyond which the absorption will subside until it becomes negligible in regions not directly exposed to the arc. Woods [62] suggested that the size of the annular region where hydrogen is absorbed could be increased by raising the surface temperature by using higher welding currents. His experimental results support this theory as it was reported that increasing the welding current from 100 to 300 amperes produced a linear increase in weld porosity.

Porosity can be minimized by proper surface preparation and welding procedures that prevent hydrogen sources from reaching the arc and weld pool. The American Welding Society [65] stresses the importance of degreasing the surface of aluminum alloys by spraying or wiping with a solvent. Removing heavy and hydrated aluminum oxides immediately prior to welding using chemical or mechanical approaches is also highly recommended. Caustic soda is a common method to chemically remove heavy aluminum oxides; however, special attention is required to rinse and dry the material to prevent the formation of new hydrated oxides. Mechanical oxide removal by manual or power wire brushing with a stainless steel brush has proven quite successful in removing heavy oxides. It should be noted that aluminum rapidly reforms its oxide layer; however, the new layer will not have sufficient time to thicken substantially before welding and should be free of hydrogen sources.

Shielding gas selection and control has also been shown to be an important factor in controlling porosity. Dowd [67] and Collins [68] showed that shielding gases containing a mixture of argon and helium were superior to pure argon or helium. They reported that a mixture containing 50 to 65% helium produced sound welds over a wider operating range than any other shielding gas mixture. Shielding gases with dew points above -40°C have also been shown to contribute to porosity due to the dissociation of water molecules to hydrogen and oxygen in the arc [63]. Finally, Woods [62] reported that increasing shielding gas flow rates from 14 to 50 l/min (30 to 105 cfh) produced slight decreases in porosity, which he suggested could be due to a cooling effect on the arc or weld pool surface.

2.4.2 Properties of Aluminum Tailor Welded Blanks

The ductility of GTAW welds made in 5182-O aluminum alloy TWBs has been investigated by Davies *et al.* [69] using a 1 to 2 mm sheet thickness combination. Longitudinal tensile tests performed on weld metal specimens showed that the weld metal exhibited a true strain of 0.18 at localization, when necking began to occur [69]. Localization strains reported for the base metal were in agreement with nominal properties of 5182 aluminum alloys that exhibit localization strains of 0.24 [69,70]. Miles *et al.* [22] reported localization strains of 0.27, which were consistent with their base metal results for GTAW welded 5182 aluminum TWBs; however, the blanks used for analysis were made from full penetration bead-on-plate welds instead of a butt weld configuration. This could account for the improvement in localization strain compared to the study by Davies *et al.* [69]

The formability of aluminum tailor welded blanks produced with laser and electron beam welding processes has also been widely investigated using limited dome height (LDH) testing [71-74]. The ratio of sheet thicknesses used was found to play a vital role in the failure location during forming of aluminum TWBs. Failure has been reported to occur in the weld for small thickness ratios and progress to failure in the thinner parent sheet as the thickness ratio increases [72]. Formability along the longitudinal axis of the weld is not affected a great deal by the thickness ratio; however, formability transverse to the weld axis can be significantly reduced for smaller thickness ratios (failure expected to occur in the weld metal) in the presence of weld contamination or defects [71]. Forming strain limits for both non-vacuum electron beam welding and dual-beam Nd:YAG laser welded aluminum TWBs that failed in the base metal were found to reach 80-85 % and 75-80 % of the limit strain of the thinner parent metal under longitudinal and transverse loading, respectively [72]. On the other hand, the forming strain limits for aluminum TWBs that failed in the weld were reported to reach only 50-55% of the limit strain of the thinner parent metal under transverse loading [72].

2.5 Summary

It has been shown in past studies conducted by Kwon *et al.* [29,30,31] and Anousheh [32] that DSAW is well suited to welding aluminum alloy sheets in the butt joint configuration. Oxide removal is optimized when a balanced square-wave alternating current is used (i.e., $\theta = \beta = 0.5$). Visually acceptable welds can be produced at speeds up to 3.6 m/min (60 mm/s) on 1.2 mm thick 5182 aluminum alloy sheet with a total welding power of 3.4 kW. Reversing or staggering the welding torches in the direction of welding did not influence

the final weld bead geometry in DSAW at a welding current of 60 amperes; however, staggering the welding torches significantly increased the weld metal porosity.

The application of DSAW to welding dissimilar thickness aluminum alloy sheets in the butt joint configuration has not been previously investigated. Also, the mechanical properties of double-sided arc welds are not well characterized, with particular emphasis on whether the weld quality, strength and ductility will be suitable for the post-weld forming required for automotive TWBs.

Weld metal porosity and surface defects have been shown to be more detrimental to the ductility and formability of aluminum tailor welded blanks than traditional steel TWBs [59,61]. Furthermore, steel TWBs typically have weld strengths greater than the base metal which suppress deformation in the weld and promotes failure in the base metal [60]; however, aluminum alloys do not strengthen during welding which can make the weld region prone to failure [69]. Weld metal failure during forming of aluminum TWBs has been shown to significantly limit the forming limits compared to base metal failure [71,72]. This suggests that any welding process used for manufacturing aluminum TWBs must be capable of consistently producing high quality welds that retain the strength as well as the ductility of the base metal.

In the following chapter, the experimental apparatus and procedures used to evaluate the feasibility of applying DSAW to welding 1.0 to 1.5 mm thick 5182 aluminum alloys sheets for tailor welded blank applications and the test methods used to evaluate the weld quality will be described.

Chapter 3

Experimental Apparatus and Procedures

3.1 Double-Sided Arc Welding System

This research was carried out using a previously designed Double-Sided Arc Welding (DSAW) system [29] that is comprised of seven major components: a constant current AC/DC welding power supply, a plasma arc welding console, a coolant recirculator, a PAW torch, a GTAW torch, a horizontal traversing welding table and a personal microcomputer-based control and data acquisition system. The power supplies, coolant recirculator and microcomputer are shown in Figure 3.1, while the traversing welding table, PAW and GTAW welding torches can be seen in Figure 3.2. Figure 3.3 shows a schematic layout of the major systems.

3.1.1 The Power Supply

A Miller® Aerowave® hybrid AC/DC constant current power supply was used to provide a square-wave AC welding current for this study. The PAW and the GTAW torches were connected to the positive and negative terminals of the power supply, respectively, as shown schematically in Figure 3.3. The power supply provided independent control of the electrode positive current, I_{EP}, electrode negative current I_{EN}, the ratio of cycle time spent in electrode negative, θ, and the AC frequency, f. For this study, β and θ were both set to 0.5 as previous DSAW research using this system showed that these settings provided best operating conditions and the best cathodic cleaning of the aluminum oxide from both sides of the sheet [29].

36

Figure 3.1: DSAW welding system including: power supply, plasma console, pilot arc booster, water recirculator and data acquisition and control system (taken from Kwon [29].)
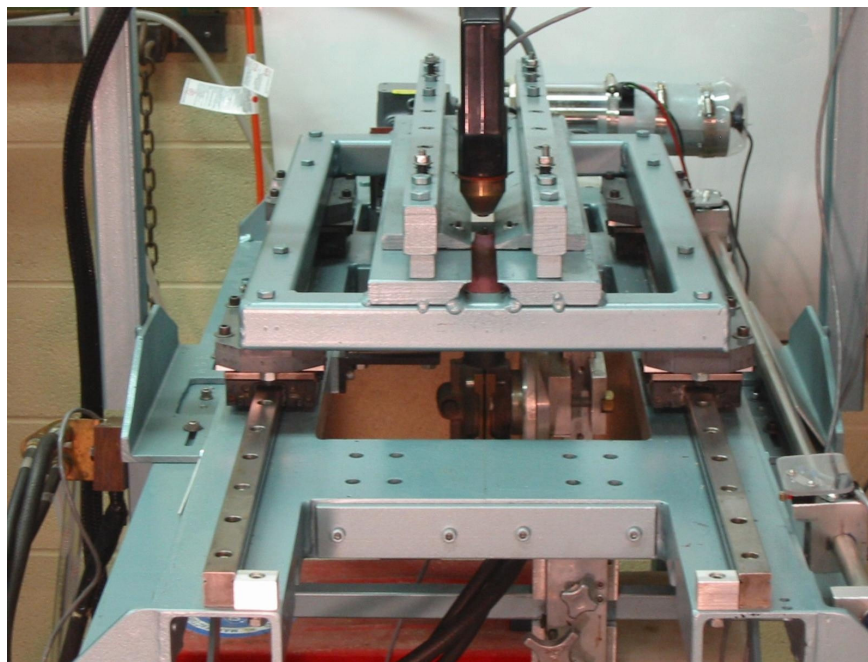
Figure 3.2: DSAW welding table, traversing carriage and PAW and GTAW torches (taken from Kwon [29]).

Shielding Gas
Plasma Gas
Cooling Water In
Cooling Water Out
Welding Current
Pilot Arc Current

Shielding Gas

Plasma Gas

PAW Torch

Welding Table
and Specimens

GTAW Torch

Plasma
Arc
Welding
Console

Pilot Arc
Current
Booster

Cooling
Water

Data
Acquisition
PC

Power
Supply

460 V Input
Power

Cooling
Water

Shielding
Gas

Ⓐ Current Transducer
Ⓥ Voltage Transducer
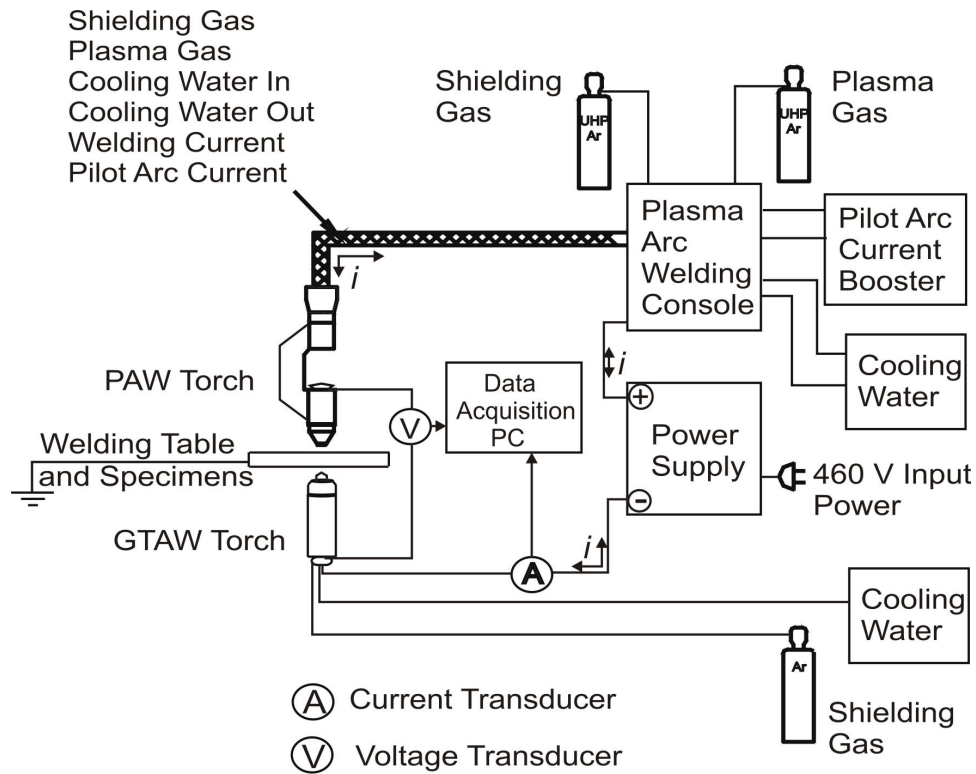
Figure 3.3: Schematic diagram of the DSAW system (taken from Kwon [29]).

A Thermal Dynamics® Thermal Arc® WC 100B plasma arc welding console was used to connect the main welding power supply to the PAW torch. The plasma console also provided control of both the shielding gas and plasma gas flow to the PAW torch as well as the flow of coolant to and from the PAW torch. The main function of the plasma console was to provide the required power and control for the pilot arc that was used to initiate the main welding arc. The pilot arc can be used in either of two modes; normal or continuous. In normal mode, the pilot arc is shutdown once the main welding arc is initiated. In continuous mode, the pilot arc remains on throughout the welding process and after the main welding arc has been shutdown. Continuous mode is intended for producing multiple welds, but is useful for improving the arc consistency when welding

with alternating current [75]. For this reason, all experiments were conducted using the pilot arc in continuous mode.

In a previous study of VPPAW of aluminum sheet [16] using this plasma console and PAW torch, the 12 A pilot arc current supplied by the console was found to be insufficient for maintaining a stable arc in the Thermal Arc® WC100B, Model 300 welding torch used in this study. To solve this problem, a pilot arc current booster circuit was designed and built to increase the pilot arc current from 12 A to 19A. The additional current significantly improved the pilot arc stability and enhanced the reliability of ignition of the main welding arc.

The welding torches were water cooled through the use of a Thermal Dynamics® model HE 100A Coolant Recirculator. This system circulated a coolant consisting of 25% ethylene glycol and 75% de-ionized and distilled water through both torches.

3.1.2 The Double Sided Arc Welding Torches

A Thermal Arc® WC100B, Model 300 PAW torch and a Weldcraft® model WP-27 GTA torch were used in this study. The PAW torch was positioned above the weld specimens on a rack and pinion mechanism which allowed the torch-to-weld specimen distance to be adjusted. The GTA torch was mounted below the weld specimens on a second rack and pinion which allowed the GTA gap to be adjusted. The configuration of the torches and welding specimen is shown in Figure 3.4. The rack and pinion mechanisms were mounted to a stationary frame that kept the welding torches stationary during welding.
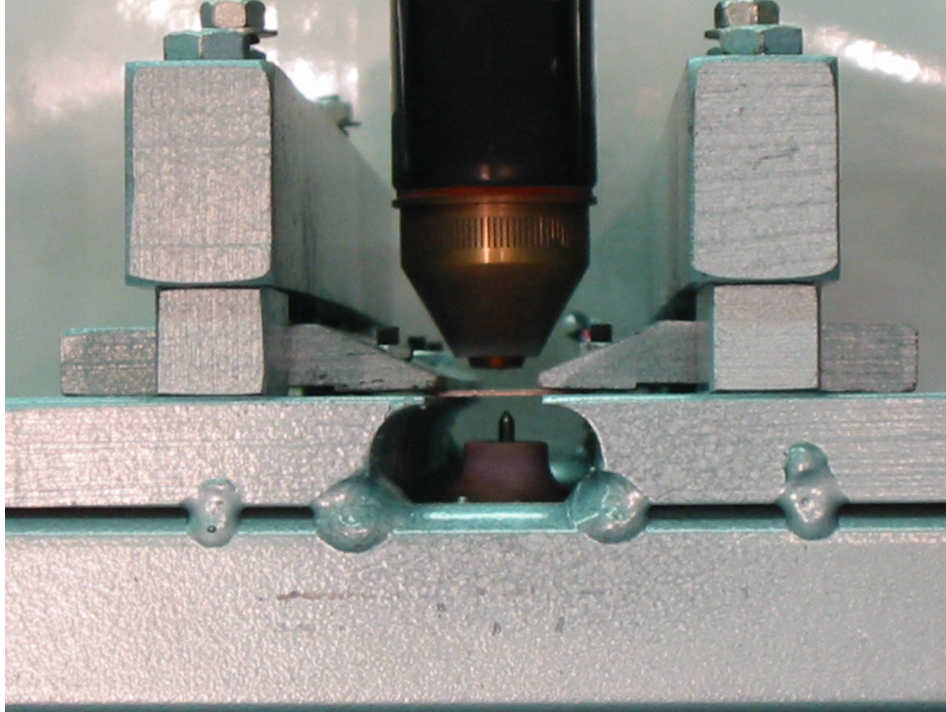
Figure 3.4: The clamping bars used to hold the specimens between the top PAW torch and the bottom GTAW torch (taken from Kwon [29]).

3.1.3 The Double Sided Arc Welding Table and Clamping Fixture

The welding table used for this study consisted of a traversing carriage running horizontally on linear bearings and rails mounted to a stationary frame to provide horizontal movement of the weld specimens between the two torches. A DC servo-motor was connected to a lead screw that was used to drive the carriage. A 10:1 gear reduction between the servo-motor and lead screw was used to move the carriage over a range of desirable welding speeds from 0 to 90 mm/s. The servo-motor was powered by a servo-motor controller that received input signals in the range of ±10 V from a National Instruments PCI 6024E data card connected to a personal microcomputer. The data card was controlled using LabView 6.0 software which enabled the table speed and direction

to be determined. The carriage movement was limited at the extreme ends of the welding table through the use of limit switches. The limit switches allowed a total travel distance of 480 mm and prevented the table from encountering hard mechanical stops at the extreme travel limits.

The welding specimens were secured to the carriage using the clamping system shown in Figure 3.4 and schematically in Figure 3.5. The specimens were pressed down against a fixed 19 mm thick cold rolled steel lower clamping bar by cold rolled steel upper clamping bar. The force for each of the upper clamping bars was provided by six 5/16" diameter 18 threads per inch socket head cap screws. The fixed lower clamping bars were unique to traditional welding tables as they allowed access to the bottom of the weld joint instead of serving as a backing bar for the joint.
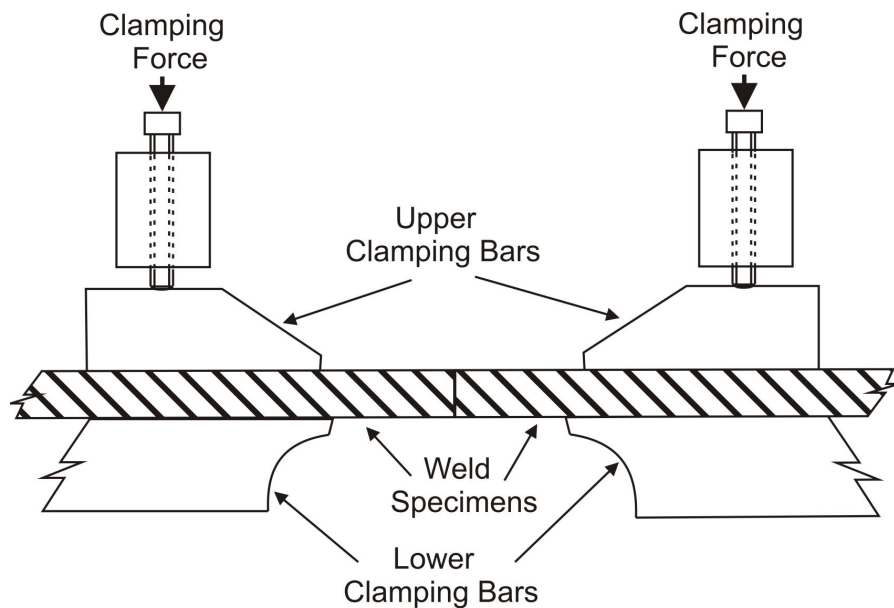
Figure 3.5: Schematic of the weld specimen clamping system (taken from Kwon [29]).

The welding carriage and welding table were electrically grounded in compliance with CSA Standard W117.2-M87 [76] to prevent accidental electrical shocks during welding. This was achieved by connecting the carriage to the stationary table frame with a flexible braided Cu grounding strap which in turn was connected to a copper grounding rod. The welding carriage was electrically isolated from the linear bearings and the lead screw ball bearings through the use of PVC plates between the carriage and bearing connections. This was done to prevent welding current flow through the bearings which could lead to a failure of the bearings and welding table.

3.1.4 The Double Sided Arc Welding Data Acquisition and Control System

A National Instruments PCI 6024 E data acquisition card connected to a personal microcomputer and controlled using National Instruments LabView 6.0 software was used to measure the welding current and voltage, and to control the welding travel speed. A LEM^{TM} LT505-S Hall-effect current transducer capable of 100 mA to 500 A was used to measure the variable polarity welding current. The transducer was connected to measure the current flowing in the cable between the power supply and the GTAW torch. A LEM^{TM} LV100 Hall-effect voltage transducer capable of 200 mV to 50V was used to measure the voltage between the GTAW torch and PAW torch. Voltage leads were installed on the electrode collets on both torches. The current and voltage transducers were factory calibrated to ± 0.1 A and ± 0.01V respectively.

The output signals from the LEM current and voltage transducers were measured using a National Instruments SCXI 1120 signal conditioning module. Schematics of the current and voltage data acquisition circuits are shown in Figure 3.6 and Figure 3.7,
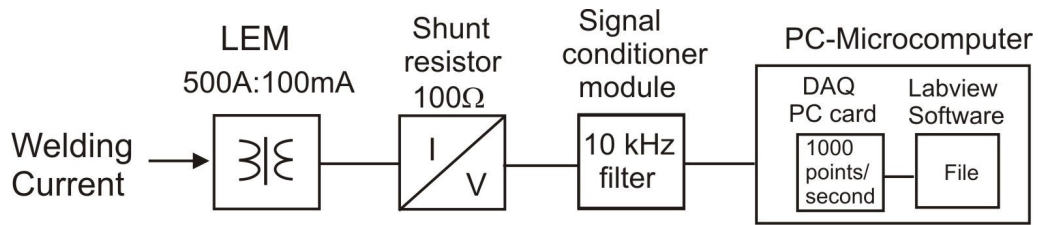
Figure 3.6: Schematic of the circuits used for acquisition and filtering of the measured welding current (taken from Deutsch [14]).
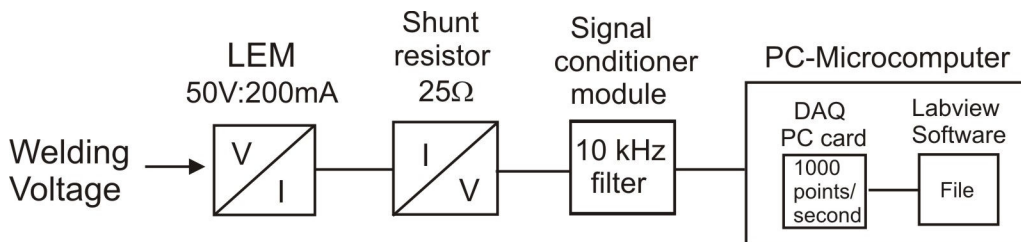
Figure 3.7: Schematic of the circuits used for acquisition and filtering of the welding voltage (taken from Deutsch [14]).

respectively. The signals were passed through a low pass filter with a 10 kHz cut off to protect the National Instruments PCI 6024E data acquisition card from the 25 kHz inverter frequency from the Aerowave® power supply and the high frequency pilot arc starter in the Thermal Arc plasma console.

A data acquisition program based on Labview 6.0 software [29] was used to process the data signals and save the raw data in a spreadsheet file format on a Pentium® III based personal microcomputer. The Labview data acquisition program also prompted the user to input several process controls as shown in Figure 3.8. This screen panel allowed the desired number of data points per channel and the scan rate or frequency of the data collection to be entered. A delay feature was used to allow the weld to reach steady state before starting the data collection. Alternatively, a delay time of 0 ms could

43
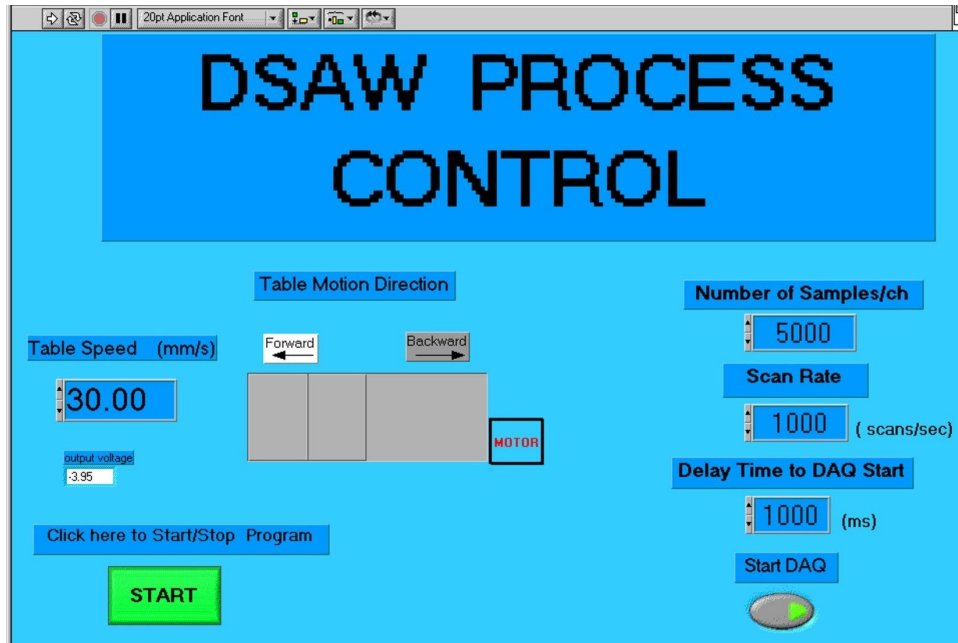
Figure 3.8: The front panel of the Labview program used for specifying the welding direction, travel speed and data collection frequency (taken from Kwon [29]).

be specified if the initial start-up transient data was required. Deutsch [14] demonstrated that a data collection frequency of 1000 Hz was sufficient to acquire accurate measurements and to calculate RMS voltage and current values of both the welding current and voltage signals for a 60 Hz welding current. The data collection frequency was scaled proportionately when higher welding current frequencies were used (i.e., a 2000 Hz data collection rate was used with a 120 Hz welding current).

After specifying the welding speed and data collection parameters on the first panel of the Labview program, the preset welding parameters were entered into the second panel of the Labview program shown in Figure 3.9. This data was recorded in the data file generated by the Labview program for reference at a later time. The welding carriage motion and the data acquisition were initiated by pressing the [Start Test] button on the second panel.
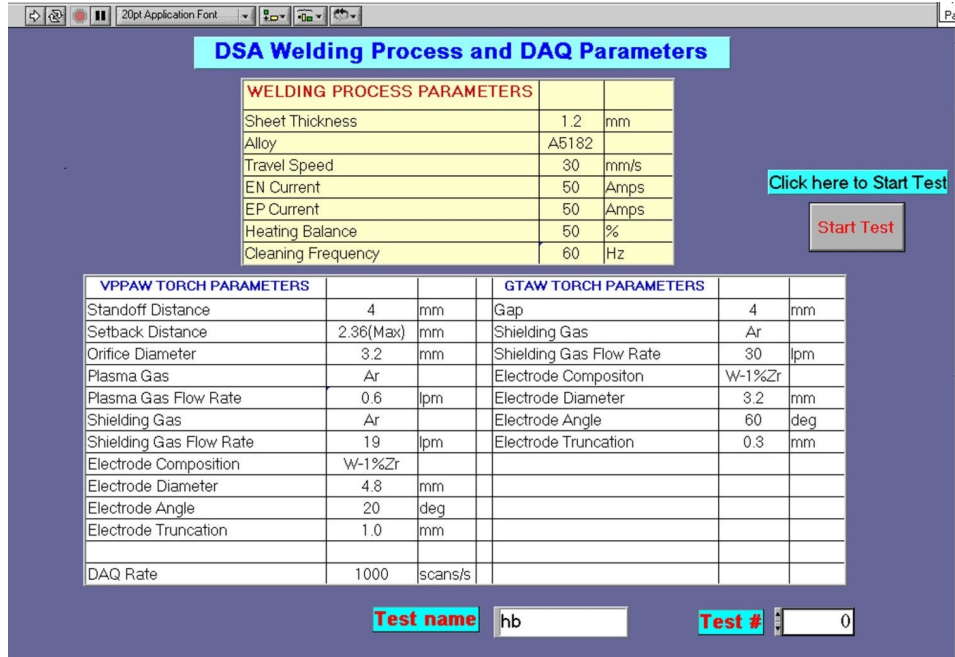
Figure 3.9: The second panel of the Labview program used to enter the fixed welding parameters (taken from Kwon [29]).

After a DSAW weld, the Labview program used the raw voltage and current data to calculate the RMS values of current and voltage based on the following equations:

$$I_{EN\_RMS} = \sqrt{\frac{\sum_{i=1}^{n}(I_{EN}(i))^2}{n}} \tag{3.1}$$

$$I_{EP\_RMS} = \sqrt{\frac{\sum_{i=1}^{n}(I_{EP}(i))^2}{n}} \tag{3.2}$$

$$V_{EN\_RMS} = \sqrt{\frac{\sum_{i=1}^{n}(V_{EN}(i))^2}{n}} \tag{3.3}$$

$$V_{EP\_RMS} = \sqrt{\frac{\sum\limits_{i=1}^{n}(V_{EP}(i))^2}{n}} \qquad (3.4)$$

$$I_{RMS} = \sqrt{\left(I_{EN\_RMS}\right)^2 \theta + \left(I_{EP\_RMS}\right)^2 (1-\theta)} \qquad (3.5)$$

$$V_{RMS} = \sqrt{\left(V_{EN\_RMS}\right)^2 \theta + \left(V_{EP\_RMS}\right)^2 (1-\theta)} \qquad (3.6)$$

where θ is the percentage of each cycle with the PAW torch in electrode negative polarity. The total RMS welding power, P_{RMS}, was calculated as the product of the RMS current and voltage as there was no measurable phase difference between the arc voltage and current. The RMS current and voltage allowed the arc resistance to be determined using Ohm's Law.

Control of the welding carriage was achieved through the use of the Labview program and the National Instruments 6024E card. The Labview program was used to produce a set-point voltage signal in the National Instruments 6024E card ranging between -10 V to 10 V. This signal was sent to a National Instruments SCXI 1138 output module which provided the required set-point voltage for the DC servo-motor controller to produce the desired carriage travel speed. In previous work by Kwon [29], a linear correlation was found between the set-point voltage and measured carriage speed, i.e.,

$$\text{Welding Speed (mm/s)} = 12.75 \text{ x (Set-point Voltage)} - 2.845 \qquad (3.7)$$

Prior to performing any welding experiments, the table speeds were verified at all welding speeds used for this study. No deviations to the above relationship were discovered.

46

Manual positioning of the welding carriage prior to welding was performed using a second Labview program. The front panel of this program is shown in Figure 3.10. A desired travel speed and direction of travel were entered into the program. Upon clicking the start button in the top left corner, the program would output the required set-point voltage to the DC servo-motor controller and drive the DC servo-motor in the desired direction at the desired speed. The program provided the capability to stop and start the table at any time and to reverse the table direction as required.
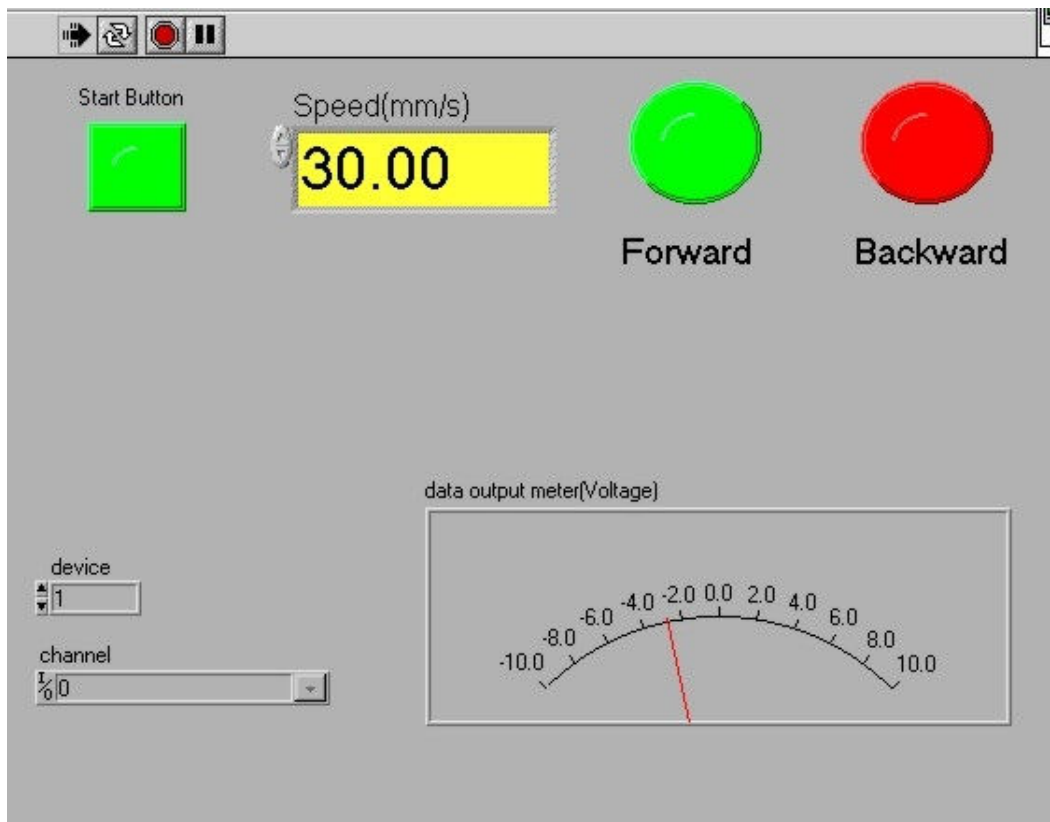
Figure 3.10: Front panel of Labview program used to move the welding carriage manually (taken from Kwon [29]).

3.2 Materials

The material used to conduct this study was non-heat treatable AA5182-O aluminum alloy (cold rolled, annealed and recrystallized) sheet in 1.0 mm and 1.5 mm thicknesses. This alloy, known for its good welding characteristics, can be welded autogeneously and does not exhibit the crack sensitivity characteristic of other wrought alloys such as the 6000 series aluminum alloys [77,78]. This alloy has been used for some automotive applications due to its strength and good formability characteristics [8]. The nominal composition of this alloy is shown in Table 3.1 and some of its mechanical and physical properties are shown in Table 3.2 [70]. This alloy derives its strength and ductility through solid solution strengthening from its main alloying element, magnesium.

Table 3.1: Nominal composition (wt%) of AA5182-O [70].

Alloy	Mg	Mn	Fe	Si	Cu	Cr	Zn	Ti	Zr	Al
5182-O	4.50	0.35	0.35	0.2	0.15	0.15	0.25	0.1	<0.01	Bal.

Table 3.2: Nominal thermal and mechanical properties of AA5182-O [70].

T_s (K)	T_l (K)	ρ (Mg/m^3)	c_p (J/kg·K)	ΔH_f (KJ/Kg)	Surface Tension (N/m)	σ_Y (MPa)	UTS (MPa)	Elongation (%)
850	911	2.65	904	396	0.605	138	275	25

3.2.1 Welding Specimens

Three sizes of welding specimens were used throughout this study. Samples used for determining operating parameters and characterizing the weld bead were performed on

samples measuring 35 mm x 220 mm. Specimens welded for transverse tensile testing measured 150 mm x 430 mm and samples welded for limiting dome height testing were 125 mm x 250 mm. All specimens were sheared to size, perpendicular to the rolling direction as this was found by Deutsch [14] to provide the best cathodic cleaning of the aluminum oxide from the weld metal. Rolling lubricants and other contaminants were removed from the surface with acetone followed by a rinse with methanol to prevent contamination problems during welding.

3.3 Experimental Procedures

The experimental procedures common to all experiments in this study are outlined below while procedures unique to a given experiment will be discussed later. It should be mentioned that for tailor welded blank applications; geometric discontinuities across a weld should be minimized to prevent stress localization that could promote premature failure during post weld forming operations. Figure 3.11a shows the geometric discontinuity and drop through that exists when welds are produced with the bottom surfaces of the 1 and 1.5 mm thick sheets aligned prior to welding as was done previously by Kwon [29] and Anousheh [32] for DSAW of similar thickness sheets. For this reason, it was decided to align the top surfaces of the sheets prior to welding to determine if this would improve the weld bead geometry. Figure 3.11b shows the resulting weld bead geometry produced when the top sheet surfaces are aligned prior to welding. This was found to reduce the weld metal sag that extends below the lowest point of the sheet surfaces from approximately 30 to 9% of the material thickness. Consequently, it was decided to align the top surfaces of the sheet specimens for all subsequent welding experiments on dissimilar thickness sheets.
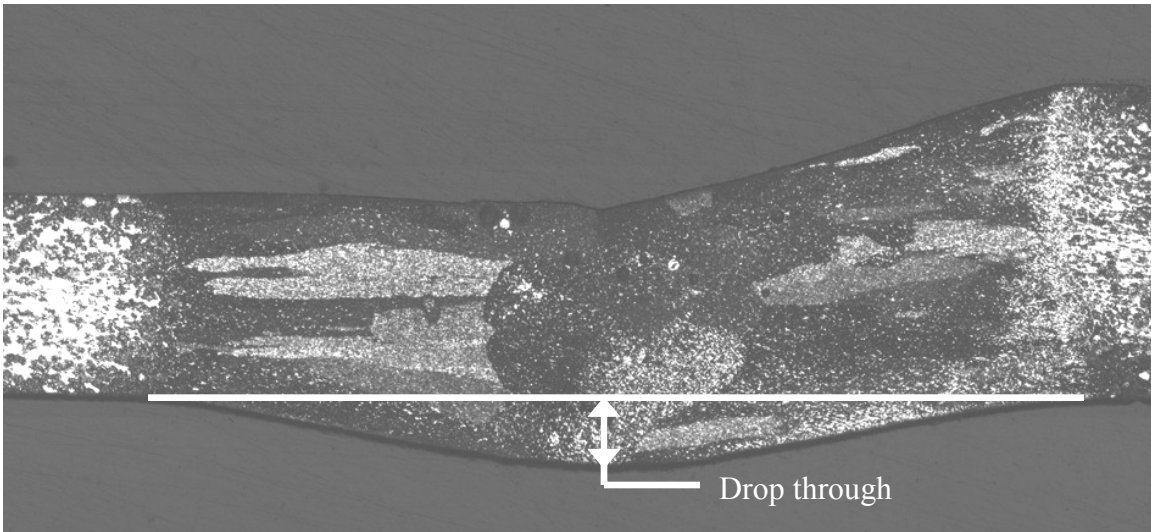
(a)
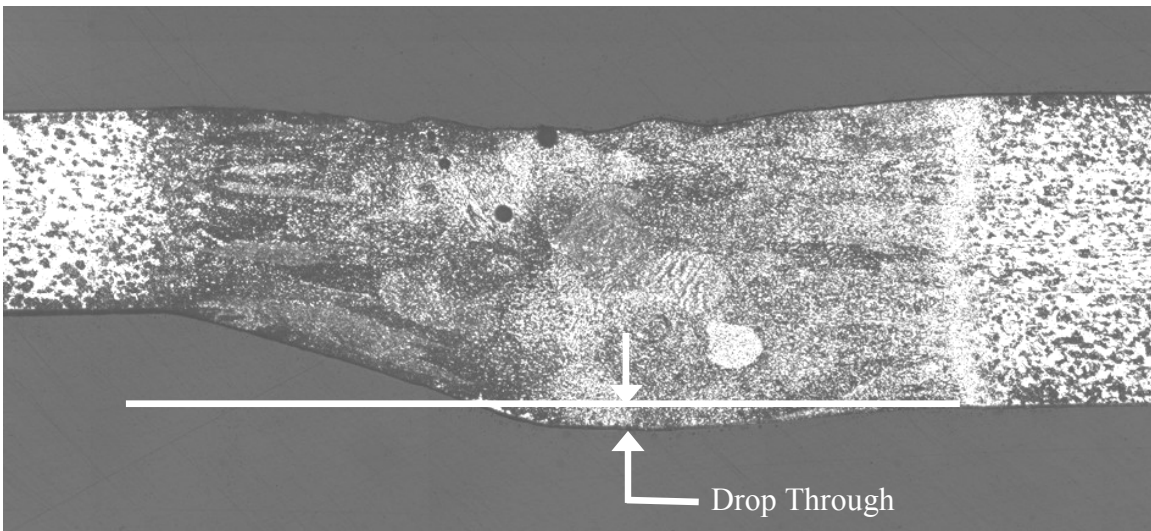
(b)

Figure 3.11: Weld cross sectional geometry illustrating the difference in weld metal drop through for welds produced between 1 and 1.5 mm thick AA5182-O aluminum alloy sheets with a) bottom of sheet surfaces aligned prior to welding, and b) top of sheet surfaces aligned prior to welding

The following are a list of the experimental procedures that were followed for all welding experiments:

1. A sharpened and truncated electrode was placed in the PAW torch at a measured setback distance. Another sharpened electrode was placed in the GTAW torch. The PAW torch standoff distance and the GTAW arc gap were set using gage blocks of desired thicknesses.

2. The electrodes were conditioned using a free standing arc between the welding torches for a period of 5 minutes. This was done to allow slight melting of the electrode tip, as would be experienced during welding experiments, to allow the electrodes to reach a steady-state balled tip condition that would provide consistent results between welds within an experimental subset.

3. The GTAW torch was aligned with the center of the carriage. The PAW torch was then aligned with the GTAW torch and the center of the carriage.

4. Weld specimens were cleaned by wiping with acetone followed by methanol.

5. For weld specimens with similar sheet thicknesses the following sequence was used to clamp the specimens. First, a removable alignment jig was inserted in the specimen holder to align the edge of the specimen directly between the two welding torches. One specimen was then placed against the alignment jig and clamped in place against the alignment jig by tightening six 5/16" diameter - 18 threads/ inch socket head cap screws to a torque of 27 N·m (20 ft-lb) using a pneumatic ratchet. Once the first specimen was secured, the alignment jig was removed and the second specimen was pushed against the first specimen and clamped securely in place.

6. For weld specimens with dissimilar sheet thickness, the following process was used to ensure the top surfaces of the sheets were flush prior to welding. First, a removable alignment jig was inserted in the specimen holder. A 1.5 mm shim was inserted in the empty specimen holder as shown schematically in Figure 3.12. The 1.0 mm specimen was then inserted in the specimen holder, aligned with the jig and clamped securely in place. The alignment jig was removed, a 1.0 mm shim inserted and then the 1.5 mm specimen was inserted into the specimen the specimen holder, pressed against the 1.0 mm specimen and clamped in place as shown in Figure 3.13.

7. The fume extraction system, the power supply, plasma console and coolant recirculator were turned on.

8. Purging of the plasma gas was completed for 5 minutes (due to the low flow rate and requirement for high purity gas) for the first weld of an experimental set and 30 seconds prior to each consecutive weld. Shielding gas and plasma gas flow rates were adjusted on the plasma console and high pressure shielding gas cylinders.

9. The welding parameters were adjusted at the power supply and entered in the second panel of the data acquisition and control program (see Figure 3.9).

10. The plasma console was switched into run mode and the pilot arc was started by pressing the high-frequency arc start button on the pilot arc current booster.

11. The main welding arc was initiated as a free standing arc between the two torches by turning on the welding current.
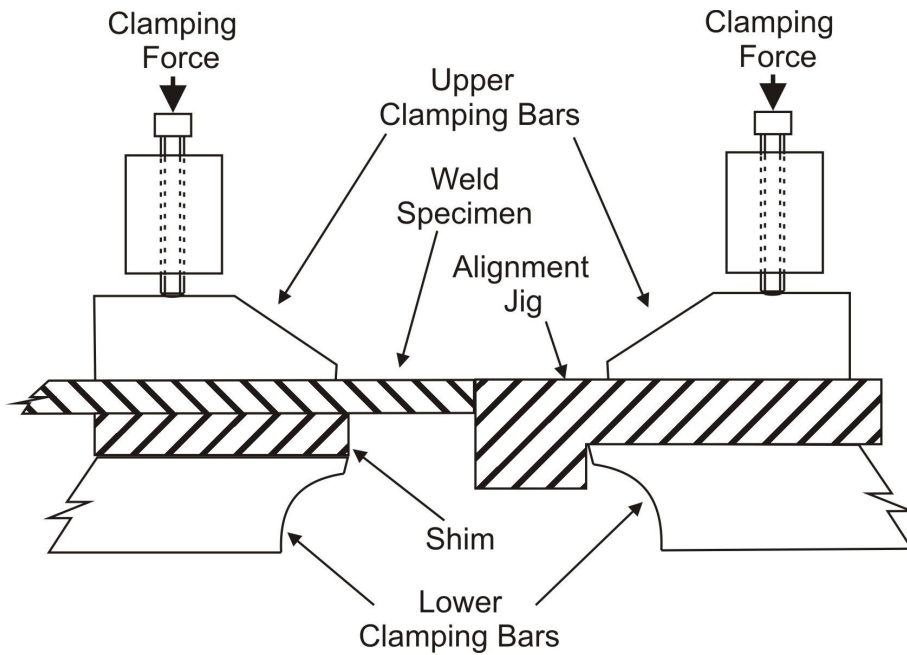
Figure 3.12:   Schematic showing the shim and alignment jig used to align the thin specimen with the welding torches.
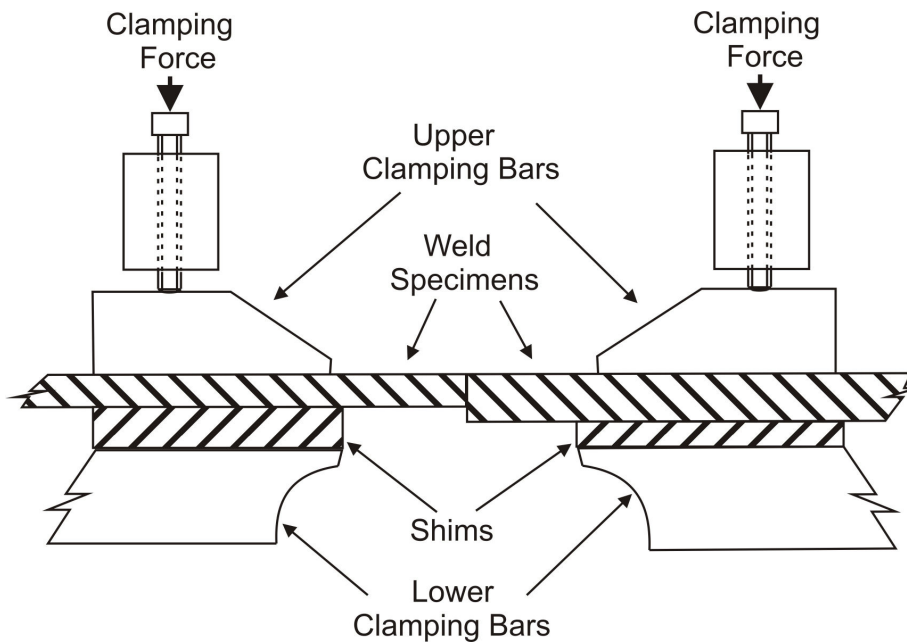
Figure 3.13:   Schematic showing the shims used to align the top surfaces of the specimens prior to welding.

12. The Labview control and data acquisition systems was started causing the welding table to move at a constant, preset speed and the data acquisition system recorded the welding voltage and current during the DSAW weld.

13. The welding table was manually returned to the start position using the second Labview program for manual control of the carriage.

14. The welded specimen was removed from the clamps.

Experimental Series A: was performed to investigate the effects of the PAW torch standoff and the GTAW arc gap on the resulting weld bead. A matrix of 16 conditions with PAW standoff and GTA gaps ranging from 1.5 mm to 6.0 mm in 1.5 mm increments was studied. Three replications were made at each combination of standoff and arc gap. PAW standoff and GTA gaps greater than 6.0 mm were not studied because the voltage required for these long arc lengths exceeded the voltage capabilities of the Miller Aerowave® power supply of ±44 V. The experiments were completed using a constant RMS welding power of 3.0 kW at a welding speed of 30 mm/s. The weld specimens used for this experimental series were all 35 mm x 220 mm x 1.5 mm thick AA5182-O sheet. All other parameters were held constant at the values listed in Table 3.3.

Experimental Series B: was performed to compare welds made with a ground (sharpened) tip electrode and a blunt tip electrode as shown in Figure 3.14. This was of interest because it was learned that VPPAW is typically carried out with a blunt tip electrode to improve weld consistency and electrode life [79,80], which is the opposite of DCEN PAW where a sharpened electrode tip is recommended [75,81]. To accommodate

Table 3.3: Constant preset welding parameters used for the PAW and GTAW welding torches.

TORCH PARAMETER	PAW	GTAW
Setback Distance (mm)	4	-
Orifice Diameter (mm)	3.2	-
Plasma Gas	UHP Ar	-
Plasma Gas Flow Rate (lpm)	0.45	-
Shielding Gas	Ar	Ar
Shielding Gas Flow Rate (lpm)	19	19
Electrode Composition	W-0.8% Zr	W-0.8% Zr
Electrode Diameter (mm)	4.8	4.8
Electrode Included Angle (deg)	20	60
Electrode Truncation (mm)	1.0	1.0
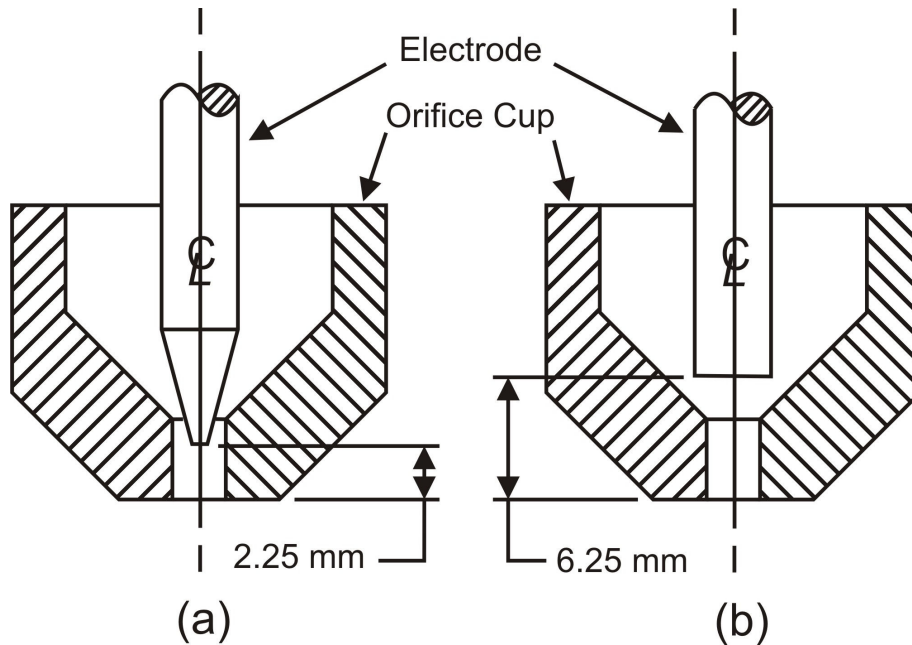
Figure 3.14: Schematic showing electrode setback required to prevent electrode-to-orifice cup short circuiting for: a) a ground electrode, and b) a blunt electrode.

the larger diameter of a blunt tip, the setback distance in the PAW torch had to be increased to prevent the electrode from short circuiting with the orifice cup. Three electrode conditions were compared: ground 20 degree included angle with 1 mm truncation at 2.25 mm setback (see Figure 3.14a) and ground 20 degree included angle with 3.2 mm truncation at 5 mm setback, and a blunt electrode with a 6.25 mm setback (see Figure 3.14b). The effect of the PAW orifice size was also investigated using 2.4 and 3.2 mm diameter orifices. The PAW standoff and the GTA gaps were held constant at 4 mm as determined in Experimental Series A. Welds were made on 1.5 mm AA5182 at 3.0 kW RMS total welding power with a travel speed of 30 mm/s. All other variables were held constant as in Experimental Series A. All studies completed after Experimental Series B used a 2.4 mm diameter PAW orifice, 20 degree included angle with a 3.2 mm truncation at a 5 mm setback for reasons that will be discussed in a later chapter.

Experimental Series C: consisted of a series of experiments to identify the operating window for butt welding dissimilar sheet thicknesses of 1.0 mm and 1.5 mm. Two experimental subsets were considered; the range of suitable welding speeds and power, and the effect of offsetting the welding torches from the joint centerline. To identify the range of suitable welding speeds and power, welds were made at total RMS powers of 1.8 to 4.6 kW in increments of 0.4 kW. Welding speeds used were from 10 to 70 mm/s in increments of 10 mm/s. For a given power, when a welding speed produced a weld with excessive heat input producing blowholes, further tests at slower travel speeds (increased heat input) were not conducted. Similarly, at high welding speeds (for a given welding power) when inconsistent weld beads due to insufficient heat input or

inconsistent cathodic cleaning of the oxide was produced, further tests at even higher speeds (lower heat inputs) were not conducted. The specimens used in these experiments were 1.0 mm and 1.5 mm thick AA5182 alloy sheet. Duplicate welds were produced on larger specimens (to allow determination of the mechanical properties) for the range of welding speeds that produced acceptable welds at 2.6 kW and 4.2 kW, and for the range of welding powers that produced acceptable welds at a constant speed of 40 mm/s.

The effects of the torch-to-joint alignment in the transverse direction on the weld dimensions and quality were investigated by making DSAW welds with the torches at various preset positions in the transverse direction relative to the weld joint. A sample with the torch and joint aligned was defined as having zero offset. Moving the torches over the thinner 1.0 mm sheet was defined as a negative offset while moving the torches over the thicker 1.5 mm sheet was defined as a positive offset. This study was performed to determine how the weld bead was affected by focusing the heat at different positions relative to the joint. Welds were produced at offsets of -2, -1, 0, 1 and 2 mm for five different welding conditions. Three of the welding conditions were completed at a constant heat input of 75 J/mm with different welding powers and travel speeds of 2.2, 3.0, and 3.8 kW at 30, 40 and 50 mm/s, respectively. The remaining experiments were run at 2.2 kW welding power with travel speeds of 20 and 24 mm/s. All other variables were held constant as identified in Experimental Series B.

Experimental Series D: was conducted to investigate the effects of abrasive cleaning of the weld specimens prior to welding on the volume of porosity in the completed weld. Control samples were welded using specimens that had been degreased using acetone and methanol. Abrasive cleaning was performed on a second set of specimens, immediately

prior to welding, using a bench grinder and a 200 mm (8 inch) diameter stainless steel wire brush with 0.3 mm diameter bristles. Welds were produced using a welding power of 3.0 kW and welding speeds of 30 and 50 mm/s. Weld quality was analyzed with a particular emphasis on the area fraction of porosity present on transverse cross sections. Experimental Series E: was carried out to optimize the welding process and examine the resulting properties of the optimized DSAW welds. Welds were produced using total welding powers of 2.6 to 4.2 kW in increments of 0.4. Travel speeds ranged between 30 and 90 mm/s in increments of 10 mm/s. 35 mm x 220 mm specimens were used for this study which had been brushed immediately prior to welding. Additional welds were produced using welding powers of 1.3, 1.8, 2.2, 2.6 and 4.2 kW, with welding speeds between 15 and 80 mm/s. These welds were used for radiographic testing, tensile testing and formability testing.

3.4 Post Weld Analysis of Double-Sided Arc Welds

3.4.1 Metallographic Examination

All of the metallographic specimens used in this study were prepared using the same procedure. Transverse sections were prepared by cutting specimens at least 50 mm from the end where steady-state weld conditions were present. Specimens were cut using a shear to obtain a straight cut. The sheared samples were set in a 32 mm diameter mount produced using Leco Castolite^{TM} polyester resin. Specimens were ground using a Struers Pedemax-2^{TM} automatic grinder/polisher with 180, 600, 800, and 1200 grit silicon carbide papers and water as a lubricant. To ensure all mechanically deformed material

from the sheared surface was removed, specimens were ground down 3 mm prior to polishing.

Polishing was carried out in two stages. The first polishing stage was completed using 1 micron alumina with a Leco PEFA polishing cloth and water as a lubricant. This was followed by polishing with Leco 1 micron diamond aerosol spray, a Leco Lecloth polishing cloth and Leco diamond lapping oil as a lubricant. Final polishing was completed using colloidal silica with glycerol as a lubricant. Polished specimens were etched with Keller's reagent to reveal microstructure and Beck and Co-workers reagent to reveal grain and macrostructure [82]. Compositions for these etchants are shown in Table 3.4 and Table 3.5, respectively.

Table 3.4 Keller's reagent for microstructure examination [82].

Chemical	HNO3	HCl	HF	H2O
Quantity	2.5 ml	1.0 ml	1.5 ml	95 ml

Table 3.5: Beck and Coworker's reagent for macrostructure and grain examination [82].

Chemical	Glycerin	HCl	HF	HNO3	Saturated aq. FeCl3 solution
Quantity	20 ml	30 ml	7 drops	0.5-1.0 ml	2 ml

An IMAGE-PRO 4.5^{TM} image analysis system was used in conjunction with an OLYMPUS^{TM} optical microscope and an OLYMPUS^{TM} C-35AD-4 digital camera to examine the polished specimens. This system was used to measure weld widths, the fusion zone area, micro-hardness indentations and to analyze the area fraction of porosity.

These measurements are shown schematically in Figure 3.15. The IMAGE-PRO 4.5^{TM} system was also used for taking photomicrographs of the DSAW welds specimens.
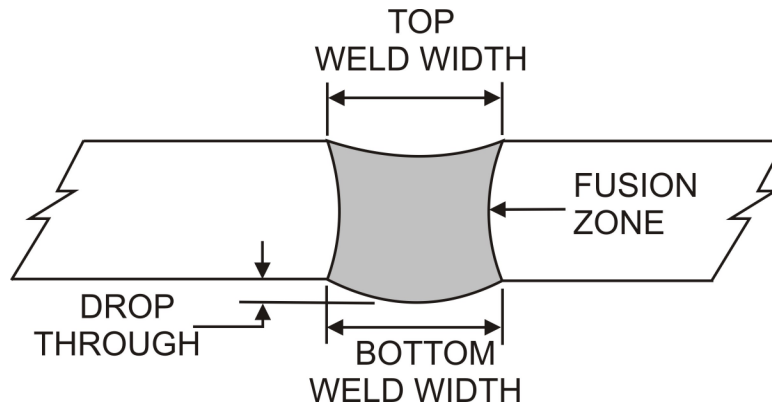
Figure 3.15: Typical measurements for characterizing DSAW welds.

Macro level pictures were taken using a Nikon Coolpix^{TM} 8800, 8 Mega-pixel digital camera. The camera was mounted on a stand that held the camera steady while providing vertical height adjustment. Specimens were illuminated using 4 desk lights to eliminate shadows and provide high quality images.

3.4.2 Mechanical Property Evaluation

Mechanical testing was performed on a series of specimens from Experimental Series C: 2.6 kW welding power at 20, 30, 40 and 50 mm/s, 4.2 kW welding power at 40, 50 and 60 mm/s, and 40 mm/s with welding powers of 3.0, 3.4 and 3.8 kW. Mechanical properties were characterized using Vickers Micro-hardness and tensile testing.

Micro-hardness tests were performed as per ASTM E92 Standard Test Method for Vickers Hardness of Metallic Materials. One specimen was tested for each of the ten welding conditions listed above. Tests were conducted using a Leco® MHT Series 200

Vickers micro-hardness tester using a 200 gram-force load. Diamond indents were made across the weld extending a minimum of five indents into the base meal on each side of the weld as shown in Figure 3.16. A constant spacing of 0.254 mm (0.010") was used between indents. Indentations were measured using the OLYMPUS^{TM} optical microscope and IMAGE-PRO 4.5^{TM} system previously described.

Transverse tensile testing was performed as per ASTM E 8M-04 using a standard sheet specimen where the weld was located in the centre of the gauge length. The specimens are shown schematically in Figure 3.17. A total of 5 specimens were tested at each of the welding conditions listed above. Five base metal samples were also tested for base metal thicknesses of 1.0 mm and 1.5 mm. Tests were conducted using an Instron model 4026 tensile machine using a crosshead speed of 10 mm/min. Raw data files were saved to a personal microcomputer for analysis at a later time.
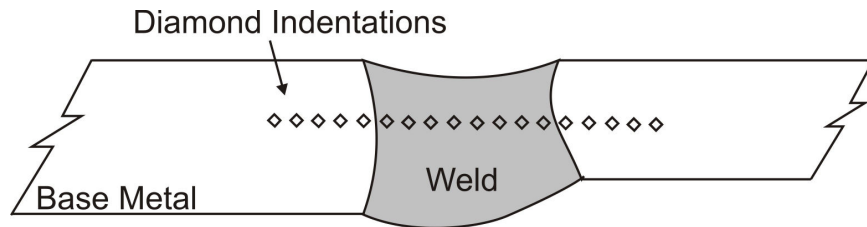
Figure 3.16: Vickers micro-hardness indentation pattern used.
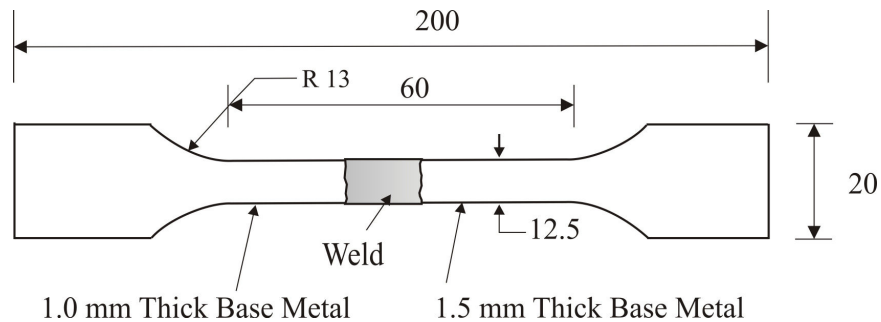
Figure 3.17: ASTM E 8M-04 modified half size tensile specimen (dimensions in mm).

A series of tensile tests were also carried out for Experimental Series E to characterize the tensile strength and elongation properties of optimized DSAW welds. Transverse tensile tests were carried out on welds made with total welding powers of 2.6 and 4.2 kW. Longitudinal tensile tests were also carried out to evaluate the yield strength, ultimate tensile strength and the elongation properties of the weld metal. The specimens used for this study were based on the ASTM E 8M-04 quarter-size specimen to accommodate a 25 mm extensometer; however, the gage width of the specimens was determined by the width of the weld for a given welding condition.

3.4.3 Formability Testing

Post weld formability tests of simulated TWBs produced with 1.0 to 1.5 mm thick 5182 aluminum sheets were performed using a MTS limiting dome height (LDH) test fixture [83]. LDH tests were carried out on welds made with a total welding power of 2.6 kW and welding speeds of 30, 40, and 50 mm/s. Five samples at each welding condition were tested and compared to results from 5 repetitions of 1.0 and 1.5 mm thick base metal samples. Test specimens were welded together and then cut to a square measuring 203 x 203 mm (8 x 8 inch) with the weld line along the centre of the specimen. A 0.5 mm thick shim was used to ensure uniform clamping was achieved on the thin sheet side of the specimen, to prevent draw-in or wrinkling of the thin sheet. A clamping force of 440 kN was used to secure the specimen. The travel speed of the 101 mm diameter hemispherical dome punch was set to 0.25 mm/s (0.01 in/s).

3.4.4 SEM-EDS Analysis

The chemical compositions across the fusion zone of weld specimens were analyzed using a JEOL JSM-6460 Scanning Electron Microscope (SEM) with Energy Dispersive Spectrometry (EDS). Four specimens were considered; 2.6 kW at 20 and 50 mm/s to examine welds with high and low net heat input at low welding power and at 4.2 kW at 40 and 60 mm/s to examine welds with high and low net heat input at high welding power. The analysis was set up to identify the weight percentage of the following elements: magnesium, manganese, iron, silicon, and zinc using a work distance of 12 mm.

3.4.5 Optical Surface Profiling

Drop through measurements of weld specimens made for Experimental Series A were carried out using a Wyko NT 1100 Optical Surface Profiler. A 2 mm wide three dimensional (3D) surface profile was made across the bottom of each of 3 replicates of the 16 welding conditions in Experimental Series A. A representative two-dimensional slice of the surface profile was saved in a spreadsheet file format for further analysis.

To determine the drop through from the surface profile, the 2D data was plotted on an X-Y axis. Distortion of the welded specimens prevented them from sitting flat on the optical profiler. Consequently, the base metal on either side of the weld was not at the same measured height on the plot as shown in Figure 3.18. To account for this and to obtain a true drop through measurement, a construction line was used to connect the base metal on each side of the weld. The largest perpendicular distance between the surface profile and the construction line was then identified as the true drop through for the specimen.
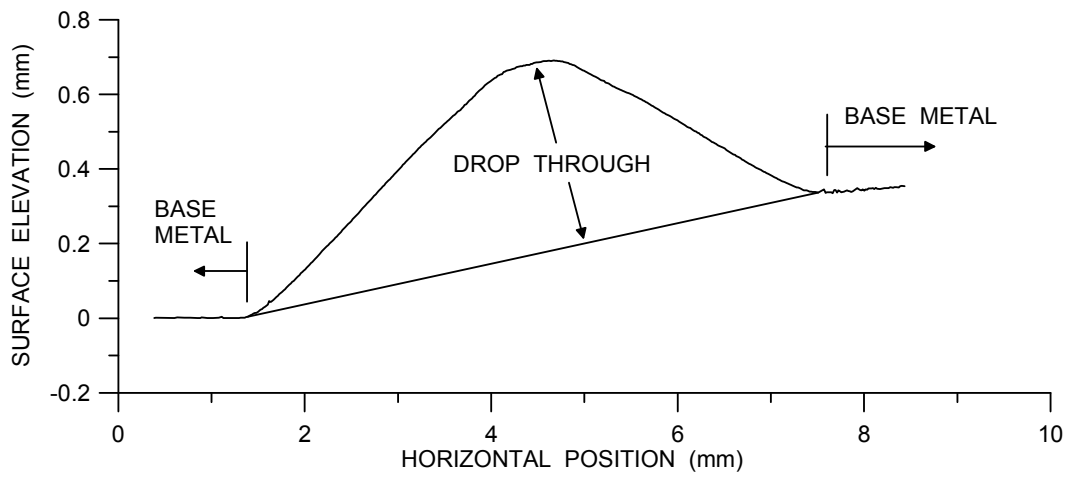
Figure 3.18: Illustration showing the drop through value determined from the optical surface profile data.

Chapter 4

Experimental Results and Discussion

This chapter is divided into five main sections corresponding to the five experimental series outlined in the previous chapter. In Experimental Series A, the effects of welding torch standoff distance were examined. The effects of changing the welding electrode geometry were studied using Experimental Series B. Experimental Series C was used to investigate the joining of dissimilar sheet combinations and Experimental Series D was used to explore the effects of stainless steel wire brushing to remove the oxide from the specimens prior to welding. Finally, Experimental Series E was used to investigate the mechanical properties of the weld metal and post-weld formability of 5182 aluminum alloy TWBs produced using the DSAW welding process.

4.1 Effects of Torch Standoff

The effect of varying the welding torch standoff was investigated to determine if the arc forces, which act in opposite directions on the weld pool in DSAW, influence the final weld bead geometry. The force exerted by an arc has been shown by Converti [54] to vary as a function of the radius of the arc at the weld pool surface and the radius of the arc at the electrode. The effective width of a welding arc has been shown to increase with increasing torch-to-workpiece distance resulting in lower current density [39,40]. For these reasons, an experimental matrix was used to evaluate whether independently changing the PAW torch and GTAW torch standoff distances would influence the

sagging of the molten weld pool (in a horizontal welding position), by changing the ratio of PAW to GTAW arc forces.

A total of 16 possible torch standoff configurations were evaluated using fixed torch standoff distances of 1.5, 3.0, 4.5, and 6 mm. Preliminary tests revealed that a significant voltage change accompanied a change in standoff distance which directly impacts the total welding power and heat input to the weld. For this reason, it was decided to use a constant welding power for all experiments instead of a constant welding current. This was done so drop through results would not be affected by varying the size of the weld pool and hence the volume of molten metal subjected to gravitational forces. All welds were produced on 1.5 mm thick sheet using a total welding power of 3.0 kW and a welding travel speed of 30 mm/s.

4.1.1 Effects of Torch Standoff on Oxide Removal

Changes in the torch standoff were observed to influence the width of the cathodically etched region produced during welding. Figure 4.1 shows the bottom surface (GTAW side) of welds produced using GTAW torch standoff distances of 1.5 and 6.0 mm. Welds produced using a small torch standoff exhibit a very small cathodically etched region beyond the weld fusion boundary. Meanwhile, larger GTAW torch standoff distances produced wider cathodically etched regions for comparable width welds as shown in Figure 4.1b. Wider cathodically etched regions were not found to improve or degrade the consistency and visual quality of the weld bead.

The top surface (PAW side) of welds produced with PAW torch standoff distances of 1.5 and 6.0 mm are shown in Figure 4.2. When the PAW torch standoff was at its minimum of 1.5 mm, no evidence of cathodic etching beyond the edge of the weld
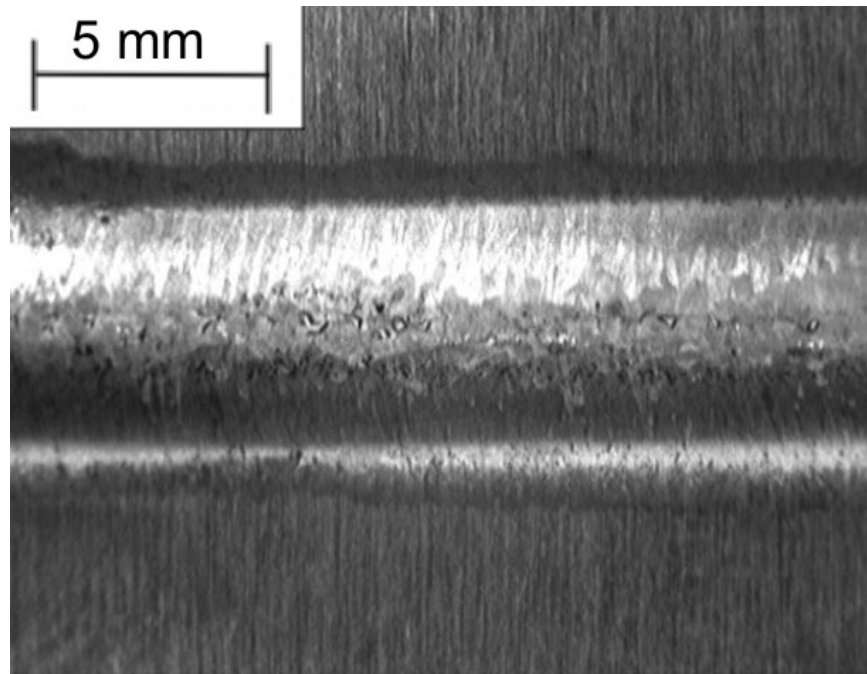
(a)
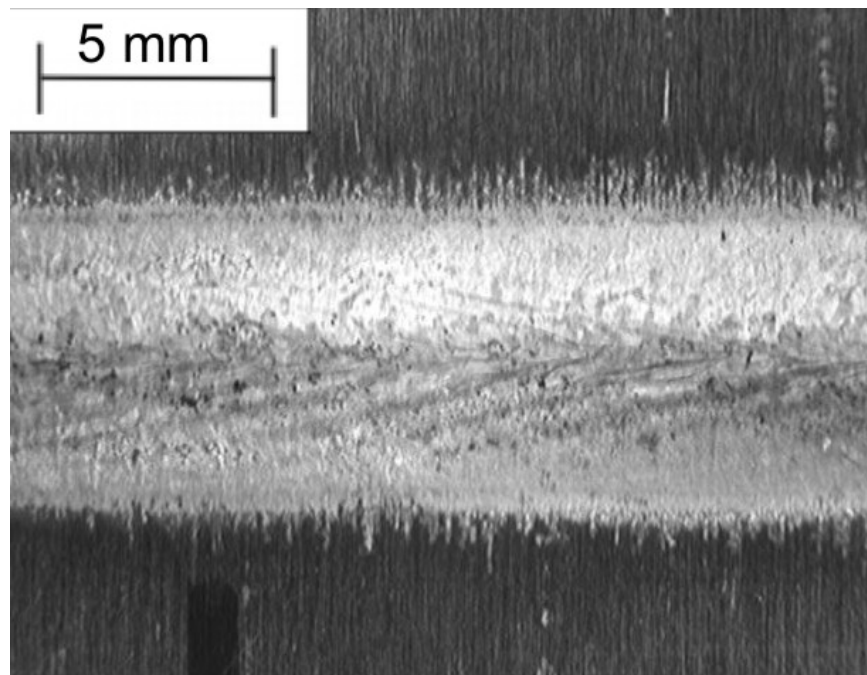
(b)

Figure 4.1: Images of GTAW (bottom) side of welds showing variations in the amount of cathodic cleaning when using torch standoff distances of a) 1.5 mm, and b) 6.0 mm.
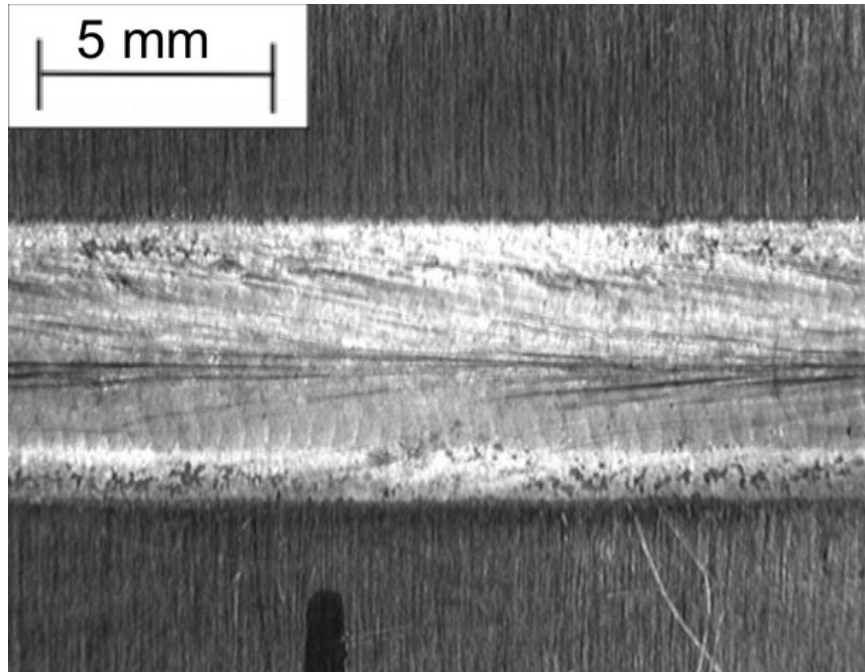
(a)
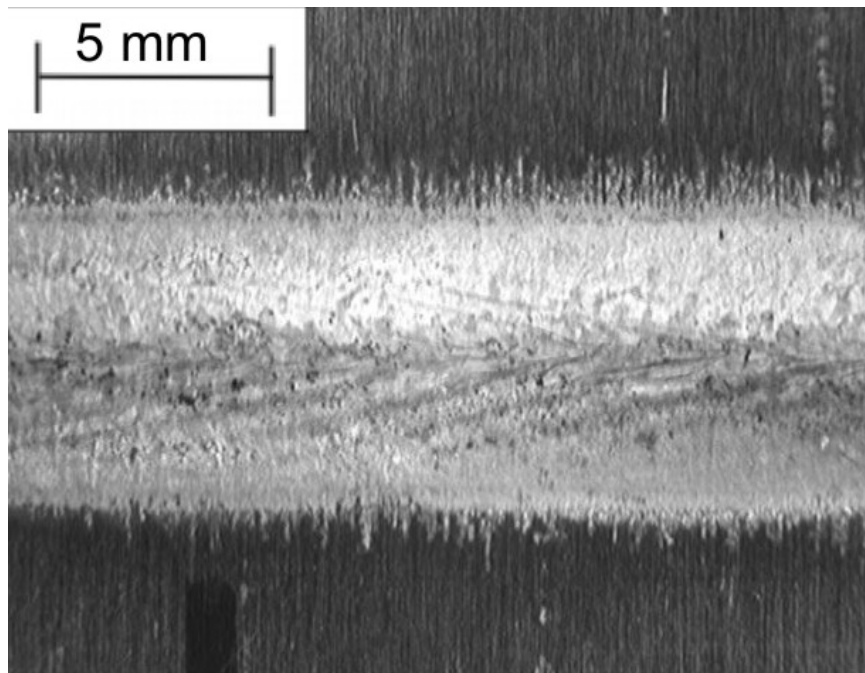
(b)

Figure 4.2: Images of PAW (top) side of welds showing variations in the amount of cathodic cleaning when using torch standoff distances of a) 1.5 mm and b) 6.0 mm.

fusion boundary was observed. Similar to the GTAW side of the weld, increased standoff distances resulted in cathodic etching beyond the edge of the weld. However, Figure 4.1 and 4.2 show that comparable torch standoff distances result in narrower cathodically etched regions for the PAW torch than for the GTAW torch. The weld widths in both cases are comparable.

As may be seen in Figure 4.1, the surface quality of the weld bead was not greatly influenced by the GTAW torch standoff. Long and short standoff distances produced a weld bead with a smooth and consistent surface. The PAW torch standoff was observed to have a more noticeable effect on the weld surface, as can be seen in Figure 4.2. A 1.5 mm PAW torch standoff produced a pronounced ripple pattern on the weld surface compared to larger torch standoff distances. PAW torch standoff distances greater than 3.0 mm all had similar surfaces to the weld shown in Figure 4.2b. Consistent weld beads were observed for all PAW torch standoff distances used in this study.

The increase in width of the cathodically etched region with increased torch standoff can be attributed to a change in the width of the current distribution across the welding arc. Increased torch standoff has been shown in previous studies to produce greater spreading or distribution of the welding arc [34,39,40] as shown schematically in Figure 4.3. Greater spreading of the welding arc will result in an increase in the surface area of the weld specimens that is in contact with the arc, causing an increase in the cathodically etched area during welding. Anousheh [32], also reported that increased torch standoff produced a wider cathodically cleaned region, in his study of DSAW.

The reduction in cathodic etching observed on the PAW side of the weld, compared to the GTAW side of the weld can be attributed to the stiff, columnar arc that is
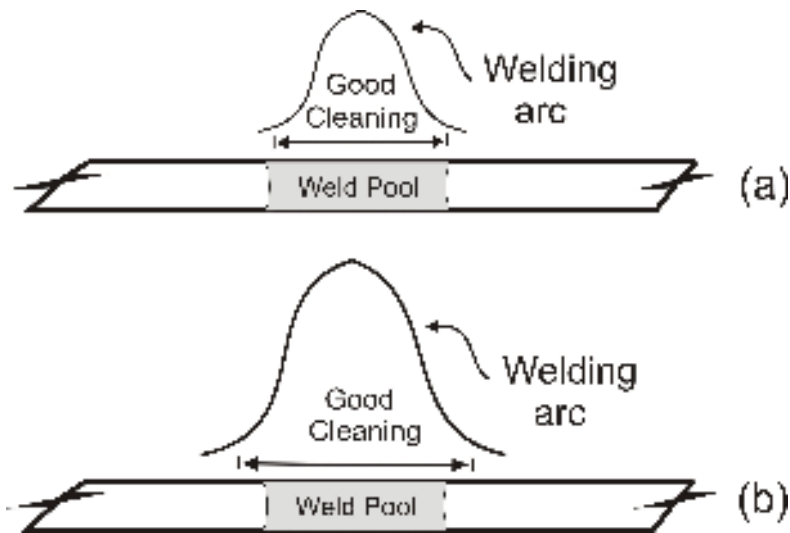
Figure 4.3: Schematic showing the relative distribution of the arc and cathodically cleaned region for a) small welding torch standoff distances and b) large welding torch standoff distances.

produced by the constricting orifice on the PAW torch. The restricted arc has a current density with a smaller arc distribution coefficient than GTAW, which accounts for the narrower cathodically etched region observed. The restricted arc in PAW also has higher plasma velocities that increase the pressure exerted on the weld pool during welding [33]. Therefore, welds produced with the shortest PAW torch standoff would have been subjected to the greatest arc pressure and corresponding aerodynamic drag forces. This could account for the more defined surface ripple texture observed on welds produced with the shortest PAW torch standoff distance.

These results indicate that narrow welds with lower net heat input could benefit from the use of smaller welding torch standoff distances. Decreasing the standoff distance will decrease the width of the arc while increasing the current density and cathodic cleaning intensity. Based on the above results; the effectiveness of cathodic

cleaning should be maximized when the torch standoff distances allow good oxide cleaning across the width of the weld, but with minimal etching of the oxide beyond the edge of the weld.

4.1.2 Effects of Torch Standoff on Weld Bead Geometry

The top and bottom weld widths were measured in three locations along each of the three replications of the 16 different torch standoff conditions. The bottom weld widths have been plotted against the GTAW standoff and the PAW standoff in Figure 4.4 and Figure 4.5, respectively. Figure 4.4 shows that the bottom weld width was not affected appreciably by the GTAW torch standoff distance while smaller PAW torch standoff distances did produce a slight increase in the bottom weld widths compared with larger PAW torch standoff distances. The trend of decreasing bottom weld width with increased PAW torch standoff can also be seen in Figure 4.5. Figure 4.5 also shows that increases in the GTAW torch standoff resulted in a slightly narrower bottom weld width; however, the 1.5 mm GTAW torch standoff is an exception to this trend.

The top weld widths are presented in Figure 4.6 and Figure 4.7. The top weld width exhibited a decreasing trend with increasing GTAW torch standoff. The minimum PAW torch standoff produced the smallest top weld width for all GTAW torch standoff values. No discernable difference in top weld width was observed for PAW torch standoff values of 3.0, 4.5, and 6.0 mm. These results indicate that the bottom weld width is influenced primarily by the PAW torch standoff, while the top weld width is influenced primarily by the GTAW torch standoff distance. The smallest welds were produced when both the PAW and GTAW torch standoff distances were set to 6 mm (the largest total arc gap).

71

Figure 4.4: Bottom weld width versus GTAW torch standoff for welds produced with a total welding power of 3.0 kW and travel speed of 30 mm/s.

Figure 4.5: Bottom weld width versus PAW torch standoff for welds produced with a total welding power of 3.0 kW and travel speed of 30 mm/s.

Figure 4.6: Top weld width vs GTAW torch standoff for welds produced with a total welding power of 3.0 kW and a travel speed of 30 mm/s.

Figure 4.7: Top weld width vs PAW torch standoff for welds produced with a total welding power of 3.0 kW and a travel speed of 30 mm/s.

The total voltage drop between the welding torches was recorded during welding and the average voltages obtained for each torch standoff configuration are presented in Figure 4.8. The arc voltages increased with the standoff distance which can be attributed to an extension of the column fall region of the top and bottom welding arcs. The column fall region is known to have an approximately linear voltage drop with the length of the welding arc [34], allowing the following linear regression model to be fitted to the experimentally obtained voltage measurements for torch standoff distances in millimeters for a constant PAW torch electrode setback of 2.25 mm:

$$\text{Arc Voltage} = 27.27 + 0.672(\text{GTA Standoff}) + 0.528(\text{PAW Standoff}) \qquad (4.1)$$

The constant value in the regression model represents the voltage drop across the anode and cathode fall regions in both arcs as well as the column fall region contained within the PAW torch (due to the electrode setback). The linear regression model was found to have a coefficient of determination (R^2) of 0.97. The arc length coefficient obtained for the PAW arc voltage compares closely to a previous study of arc voltage in PAW by Deutsch [14]. The lower arc length coefficient obtained for the PAW standoff compared to the GTAW standoff could be associated with continuously running pilot arc in the PAW torch. The continuous pilot arc will ionize the plasma gas as it exits the torch providing an ionized plasma jet which could reduce the resistance and hence the voltage across the arc gap for the PAW torch.

Due to the characteristic change in arc voltage for different torch standoff distances, the ratio of the total welding power (held constant across all experiments) supplied by the GTAW and PAW torches varied slightly for different combinations of torch standoff. For example, increasing the GTAW torch standoff would increase the

74
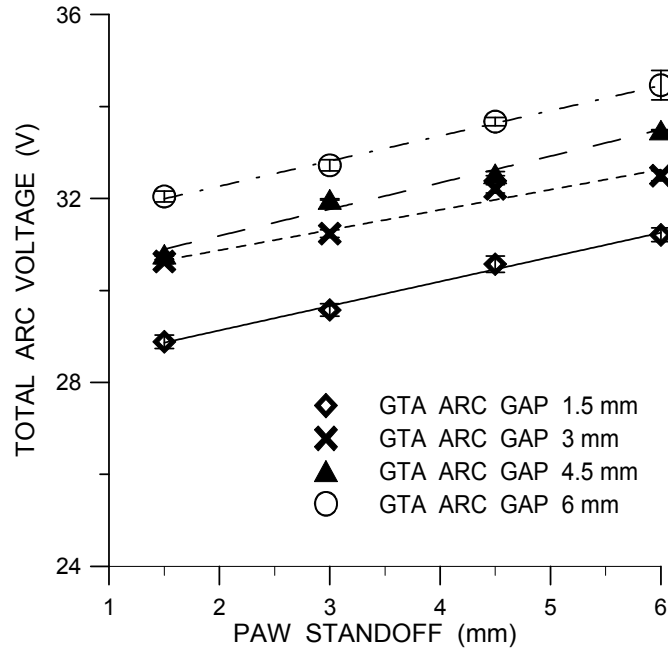
Figure 4.8: Total arc voltage between the PAW and GTAW welding torches for varying torch standoff distances.

column fall voltage of the GTAW arc. For the constant welding power used in this experiment, an increase in total arc voltage required a decrease in the total welding current. As a result the portion of the welding power supplied by the GTAW torch increased while the welding power supplied by the PAW torch decreased. The decrease in the ratio of power supplied by the PAW torch explains why the width of the top weld (produced by the PAW torch) decreased when the GTAW torch standoff was increased. The reverse case is also true explaining why the bottom weld (GTAW) width decreased when the PAW torch standoff was increased.

The decrease in top and bottom weld width observed with increasing GTAW and PAW torch standoff distances can be attributed to a decrease in the welding arc efficiency. Increases in arc voltage are known to reduce the efficiency of the welding arc and have been observed by several researchers [34,38]. The decrease in efficiency is

caused by increased radiation and convection heat loss from the longer welding arc to the surroundings. Deutsch [14] also reported that increases in PAW torch standoff resulted in smaller weld widths when using 5182 aluminum alloys. For these reasons, it is expected that the decrease in weld widths observed in this experiment with increasing standoff distance were caused by decreasing arc efficiencies.

An optical profiler was used to characterize the bottom weld surfaces and determine the resulting weld metal drop through for each torch standoff configuration. The drop through versus the GTAW torch standoff and the PAW torch standoff are presented in Figure 4.9 and Figure 4.10, respectively. The weld metal drop through versus GTAW torch standoff, shown in Figure 4.9, shows a slight decrease in drop through as the GTAW torch standoff is increased. The decrease in drop through with increasing GTAW torch standoff is most dominant for the welds produced with a PAW torch standoff of 1.5 mm. Figure 4.10 shows that weld metal drop through measurements were consistent for all PAW torch standoff values used in this experiment, but a slight decrease in the spread of the data is observed for larger PAW standoff distances

The slight decreases in drop through observed in this experiment occur at the same torch standoff configurations that produced the narrowest welds (long standoff distances). As these welding conditions have the lowest arc efficiencies, it is believed that the slight decreases in weld metal drop through are directly related to the size of the weld pool. The narrower welds produced using longer standoff distances were found to have cross sectional areas about 8% smaller than the largest welds produced at short standoff distances. This decrease in the size of the weld pool would have decreased the
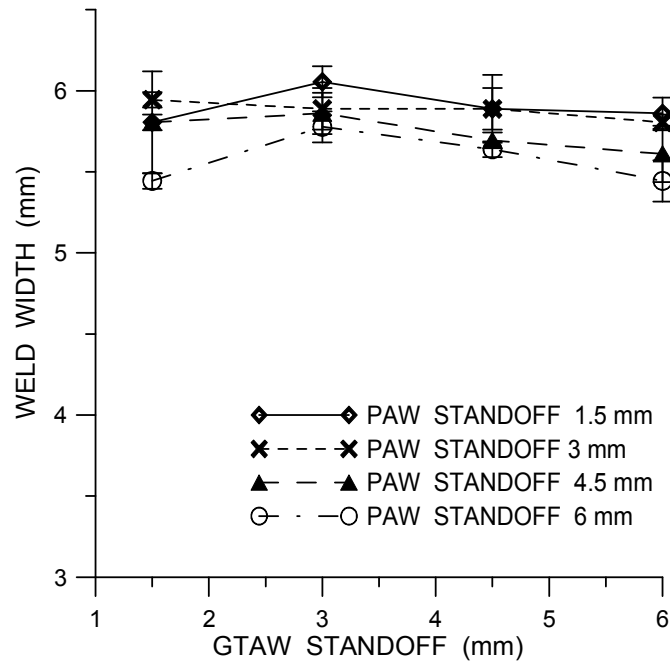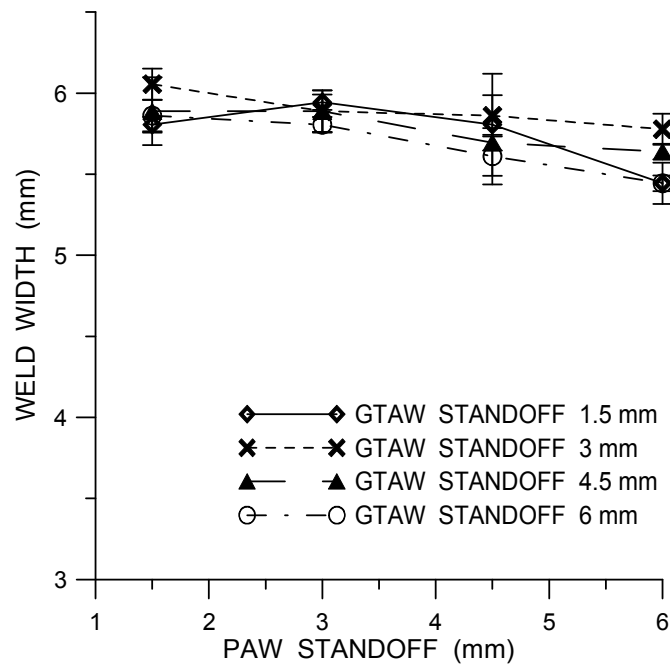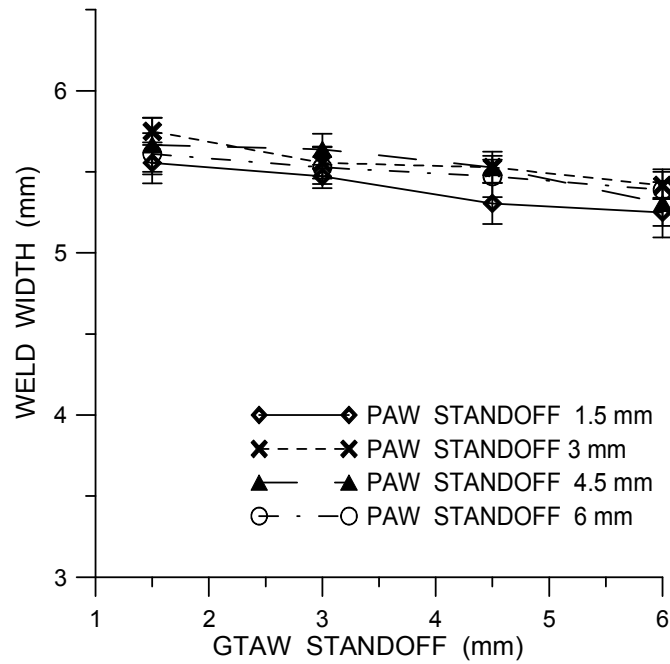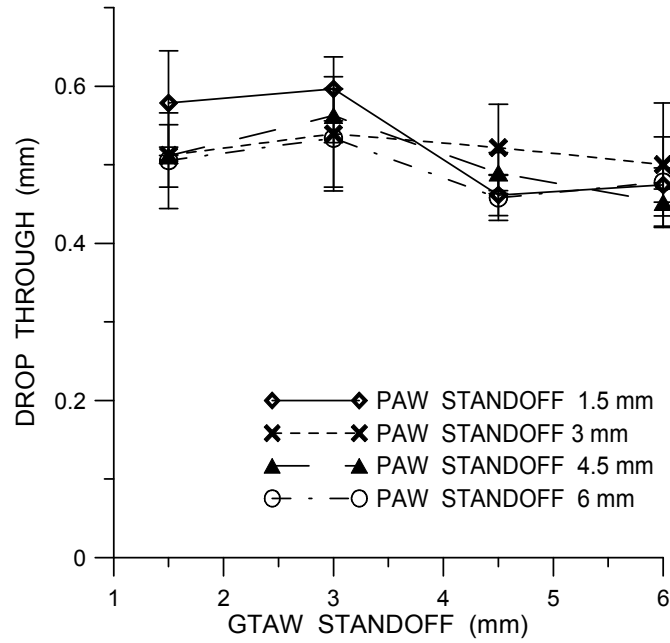
Figure 4.9: Weld metal drop through versus GTAW torch standoff for welds produced with a total welding power of 3.0 kW and a travel speed of 30 mm/s.
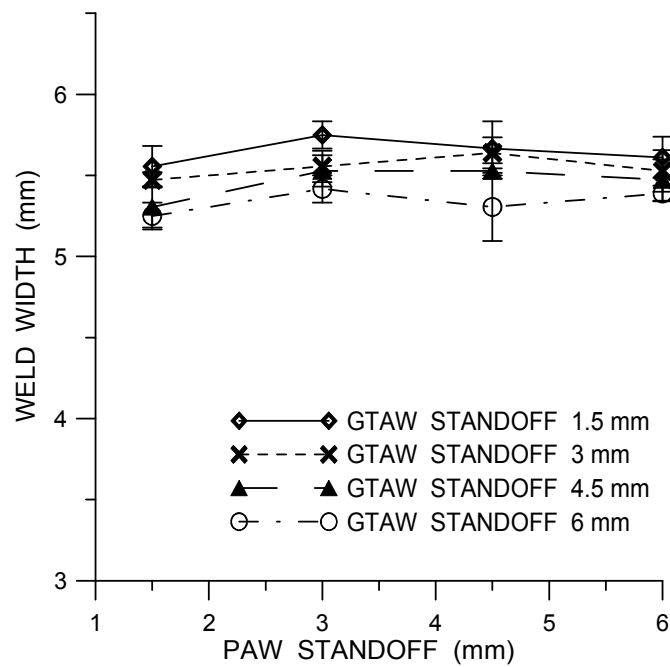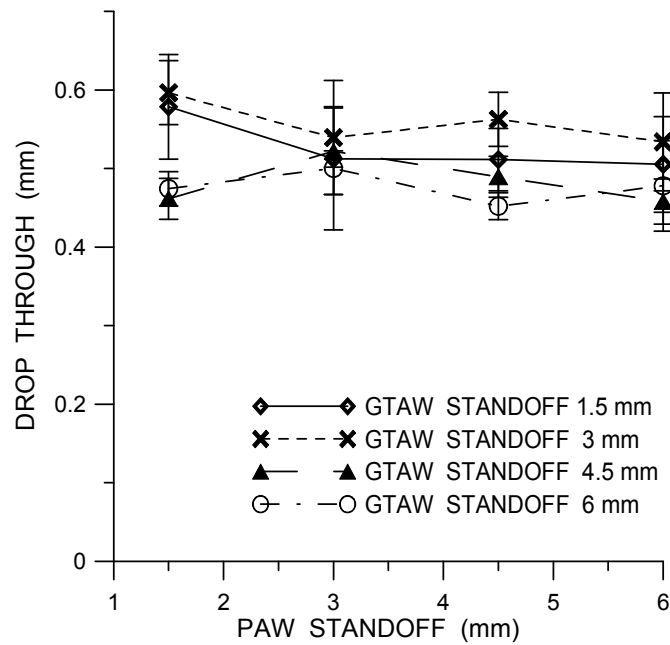

Figure 4.10: Weld metal drop through versus PAW torch standoff for welds produced with a total welding power of 3.0 kW and a travel speed of 30 mm/s.

77

volume of molten metal subjected to gravitational force and the extent of the weld metal drop through.

The results of this study suggest that the weld metal drop through observed in the DSAW welds made in the horizontal position is primarily influenced by gravity and surface tension. Varying the standoff distances of the top and bottom welding torches to change the magnitude of the arc force did not produce an observable difference the resulting drop through of the weld bead. The welding current used in these experiments ranged between 87 A and 104 A which lies well below a reported threshold welding current of 200 A required to produce any significant weld pool depression using GTAW [51,52]. Therefore, the lack of influence of arc gap on weld metal drop through, observed in this experiment, agrees with previous understanding of the effects of arc forces in GTAW. This experiment also suggests that the arc forces in PAW do not influence the weld bead geometry for welding currents below 104 A.

Another factor that could explain the limited influence of the arc force on the resulting weld geometry is the length of the weld pool compared to the radius of the welding arc. The ripple pattern on the welds shown in Figure 4.2 can be used to estimate the length of the weld pool at approximately 8 to 10 mm. Meanwhile, the power density of the welding arc in GTAW has been reported to approximate a Gaussian distribution with the power density of the arc falling rapidly beyond an arc radius of 2 mm for a torch standoff of 4.7 mm [39,40]. This suggests the molten weld pool extents well beyond the region under the influence of the welding arc forces. The weld pool will be expected to sag as it emerges from the region influenced by the arc forces and the final weld bead geometry will be influenced primarily by gravity and surface tension forces.

The experiments in the remainder of this thesis were carried out using welding torch standoff distances between 3 mm and 4.5 mm for two main reasons. First, although no significant trend was observed between the torch standoff and the resulting weld metal drop through, less variation was observed in the data collected for torch standoff distances exceeding 3 mm. The second reason is the importance of cathodic cleaning for weld pool stability. The results suggested that the cathodically cleaned region was narrower that the weld pool itself for torch standoff distances less than 3 mm, justifying the use of a slightly larger standoff distance.

4.2 Effects of PAW Electrode Geometry

A comparative study was done to examine the effects of changing the W-0.8% Zr PAW torch electrode from a conical tip with a 20° angle and 1 mm truncation to a 4.8 mm diameter blunt tip (diameter of the electrode). This change was investigated for a number of reasons. First, traditional direct current electrode negative (DCEN) PAW is performed with an electrode that has been ground to a point [75,81]. For DCEN welding applications the work piece is the anode and approximately 70 % of the total arc heat goes into the work piece and only 30 % into the electrode (cathode) [23]. In this case, heating of the electrode is not sufficient to cause melting of the electrode tip thereby allowing the tip of the electrode to maintain its shape for long periods of operation. However, VPPAW, with a balanced AC waveform ($\theta = \beta = 0.5$) introduces an average of 50% of the arc heat into the anode and 50% into the cathode for each current cycle. As a result, the electrode tip can overheat and a molten ball of tungsten can form at the end of the electrode. As welding powers are increased, the size of the molten ball on the electrode increases causing rapid electrode deterioration. In extreme cases, it can even

cause the electrode to short circuit with the orifice cup, hindering the operation of the welding torch. Deutsch [14] and Punkari [16] reported very high rates of electrode tip degradation when using conical electrodes for VPPAW welding of 5182 and 5754 aluminum alloy sheet. They also reported a lack of reproducibility between experiments caused by the change in electrode tip geometry. The motivation for investigating use of a blunt tip electrode came from a number of recommendations that VPPAW should be performed with a blunt electrode to prevent melting and balling of the electrode tip [79,80]. A blunt electrode tip increases the cross sectional area of the electrode tip. This increases the heat transfer away from the tip, thus extending the electrode life by preventing the formation of a molten ball during welding. Therefore, it was of interest to see if changing the electrode tip condition would impact the resulting weld quality or geometry.

The geometry of the blunt electrode required increased setback to prevent direct contact between the electrode and orifice cup as shown in Figure 3.14. Therefore, a number of welds were produced using a ground electrode and increased electrode setback so that a direct comparison could be made between welds produced using the ground and blunt electrodes. The effects of using two different constricting orifice diameters were also compared. This was done to see if the width of the weld could be reduced by increasing the constriction and hence increasing the power density of the welding arc. All welds were produced on 1.5 mm thick sheets with a total welding power of 3.0 kW and at a travel speed of 30 mm/s. The constant welding power was achieved by adjusting the preset welding current to account for the different arc voltages that were produced from the different electrode tip conditions and setback distances.

80

Table 4.1 presents the average voltage and current measurements recorded by the data acquisition system for 3 welded specimens at each test condition. The average weld widths measured for the top and bottom welds (3 measurements per specimen for a total of 9 measurements per welding condition) are also presented in Table 4.1. With a 3.2 mm diameter orifice, increasing the electrode setback from 2.25 mm in Test #1 to 6.25 mm in Test #2 was found to increase the total arc voltage from 30.6 to 35.3 V for an increase of 4.7 V. An increase in voltage would normally be expected due to the increase in the length of the column fall region of the PAW torch. However, this increase in voltage is more than double the 2.1 V increase predicted by the linear regression fit obtained from the previous torch standoff experiments (see Equation 4.1) for an increase in the plasma arc length of 4 mm. Deutsch [14] reported similar increases in voltage to those obtained in this experiment for increased electrode setback. He also reported that the increase in voltage for an increase in electrode setback was greater than that observed for the same increase in torch standoff distance; however, no explanation for this effect has been proposed thus far.

Table 4.1: Electrode geometry, setback and orifice diameters tested to examine their effects on welding arc voltage and resulting weld dimensions.

Test No.	Electrode Truncation (mm)	Electrode Setback (mm)	Orifice Diameter (mm)	V_{RMS} (V)	I_{RMS} (A)	Top Weld Width (mm)	Bottom Weld Width (mm)
1	1	2.25	3.2	30.6	100.6	5.28 ± 0.20	5.14 ± 0.36
2	1	6.25	3.2	35.3	86.3	4.44 ± 0.17	4.25 ± 0.25
3	4.8 (Blunt)	6.25	3.2	36.4	83.6	4.25 ± 0.13	3.97 ± 0.23
4	1	2.25	2.4	32.1	95.3	5.11 ± 0.31	5.00 ± 0.22
5	4.8 (Blunt)	6.25	2.4	38.7	79.0	4.00 ± 0.25	4.10 ± 0.22
6	3.2	5	2.4	38.0	79.1	-	-

In Test #3, the ground electrode was switched to a blunt electrode with a 6.25 mm electrode setback and a 3.2 mm diameter orifice. This caused an increase in total arc voltage of approximately 1 V. Examination of the ends of the ground and blunt electrode shown in Figure 4.11 and Figure 4.12, respectively, reveals that the tip of the ground electrode heated up so much that it melted and formed a hemispherical ball of molten metal during welding, whereas, the blunt electrode only had a small molten spot. The decreased size of the molten spot on the blunt electrode suggests that the tip of the blunt electrode is cooler than the tip of the ground electrode.

Examination of the electrode negative and electrode positive components (V_{EN_RMS} and V_{EP_RMS}) of the total RMS voltages in Test #2 and #3 revealed that the increase in voltage experienced with a blunt electrode was primarily caused by a stark increase in V_{EN_RMS}. V_{EN_RMS} was found to increase from 34.9 V to 38.1 V when switching from a ground electrode tip to a blunt electrode tip. During electrode negative polarity, the electrode is the cathode and must supply energy in the form of heat to evaporate electrons from the surface [34]. In the GTAW and PAW welding processes, this occurs primarily by thermionic emission from the tungsten electrode. The cooler electrode tip associated with the blunt electrode would reduce the thermionic emission of electrons from the electrode, thereby requiring a greater potential field to sustain the same welding current flow. Therefore, the increase in voltage associated with a blunt electrode is most likely caused by the welding power supply compensating for the decrease in thermionic emission of electrons from the PAW electrode to maintain the preset welding current.

Figure 4.11: Image of a ground 4.8 mm diameter electrode after welding showing the shape of the molten balled tip formed during welding.

Figure 4.12: Images of a blunt 4.8 mm diameter electrode after welding showing little evidence of significant melting of the electrode tip during welding.

The top and bottom weld widths of welds produced in Test #1 and Test #2 were both observed to decrease in width when the PAW electrode setback of the ground electrode was increased from 2.25 mm to 6.25 mm. A further decrease in weld width was observed when a blunt tip electrode was used in Test #3. The decrease in the bottom weld width was caused by a decrease in the fraction of the total welding power supplied by the GTAW torch. This decrease was caused by the need to use lower welding currents to offset the increased voltage associated with the PAW electrode changes while maintaining a constant welding power. The decrease in top weld widths with increased electrode setback can be attributed to a decrease in arc efficiency caused by increased

83

heat loss to the water cooled copper orifice on the PAW torch. Deutsch [14] also reported that welds produced with VPPAW showed decreasing weld widths as the electrode setback distance was increased.

Comparing Tests #1 versus #4 and Tests #2 versus #5, it was observed that decreasing the size of the PAW torch orifice from 3.2 to 2.4 mm resulted in a slight increase in the arc voltage and decreased the width of the top weld. No appreciable change in the bottom weld width was observed. The decrease in the top weld width is likely a result of the increased energy density of the arc due to the smaller constricting orifice. Increasing the constriction of the PAW arc has been widely accepted to cause a decrease in weld width while increasing the penetration [23,33]. Although the arc voltage did increase which could contribute to a decreased arc efficiency and produce a narrower weld, the bottom weld width remained constant despite having a lower heat input from the GTAW torch (due to decreased welding current to maintain a constant power). This would suggest that the heat from the PAW torch was penetrating deeper into the weld pool, contributing heat to the lower part of the weld pool and compensating for the decrease in heat input from the GTAW torch. This observation suggests that the use of two opposing plasma torches, with small orifice diameters, could be beneficial for reducing the heat input to the weld thereby minimizing the width of the fusion zone.

The increased voltage associated with using the blunt electrode at a 6.25 mm setback and the smaller 2.4 mm diameter orifice presented a practical problem for the welding power supply used in this study. Although the steady-state welding voltage was below the ±44 V capability of the constant current power supply, the start-up transient voltage was observed to exceed 44 V when the PAW torch was in electrode negative

polarity as shown in Figure 4.13. On several occasions, this spike in the voltage caused the power supply to shut down. Kwon [29], was the first to report and explain the start-up voltage transient that occurs when using DSAW to weld 5182 aluminum sheet. During start-up, a free-standing arc is produced between the two welding torches. The arc voltage of the free standing arc is lower than the steady state welding voltage because there are only anode and cathode fall regions at the electrodes. During the transition between the free-standing arc and steady state welding conditions, Kwon [29] reported that the welding arc would wrap around the leading edge of the work piece. The arc wrapping around the work piece occurs because the increase in the length of the column fall region initially produces a lower voltage potential between the welding torches than coupling with the material. Eventually, the length of the arc reaches a point where the voltage potential between the torches would be lower for an arc coupled with the work piece. At this point a maximum voltage is observed as the arc begins to couple with the work piece. The voltage subsequently falls to the steady state voltage as a stable weld pool is established. The steady welding voltage is greater than the free-standing arc voltage due to the additional cathode and anode fall regions that now exist at the top and bottom surfaces of the weld pool.

To eliminate the problem of the power supply cutting out during the start-up transient, an electrode ground to a 20° included angle and truncated to a 3.2 mm diameter was used. This electrode geometry allowed the setback distance to be reduced to 5 mm which in turn reduced the arc voltage. This electrode is compared to a blunt electrode in Figure 4.14. It can be seen that a larger molten spot existed on the partly ground electrode, but the melting was not sufficient to form a molten ball at the electrode tip.
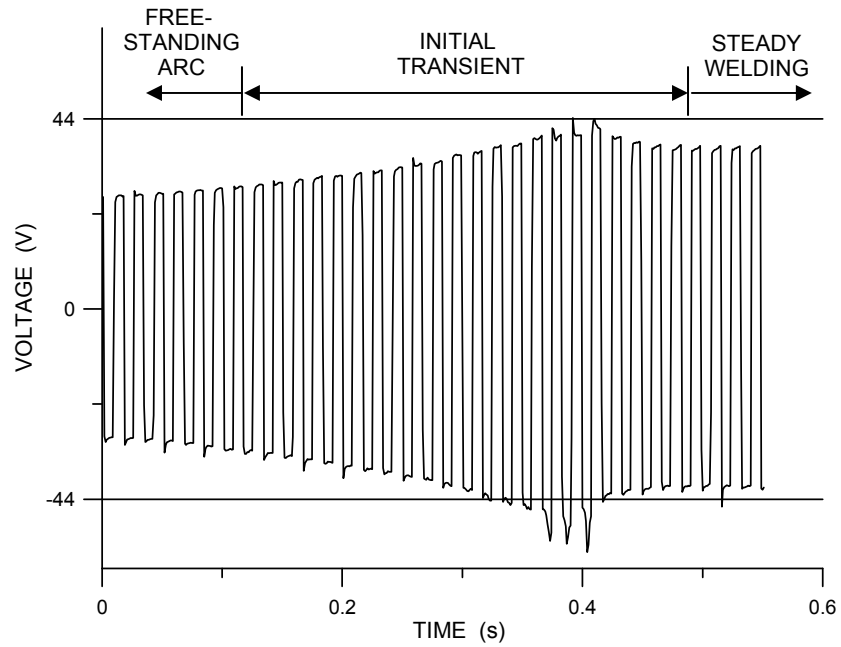
Figure 4.13: Start-up voltage transient is observed to exceed the ±44 V output capability of the welding power supply when a blunt electrode with a 6.25 mm electrode setback distance is used.
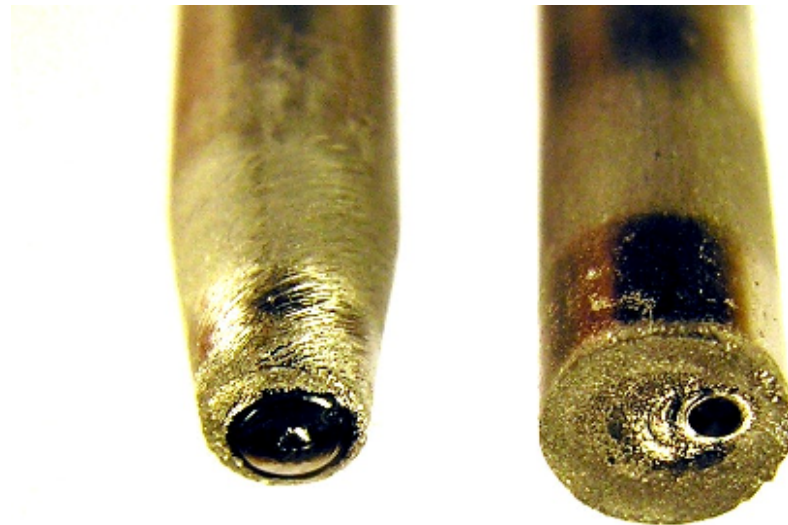
Figure 4.14: Ground electrode truncated to 3.2 mm diameter shown on left with larger molten spot than blunt electrode shown on right.

The larger molten spot is also believed to be responsible for improving thermionic emission in electrode negative polarity to reduce the electrode negative voltage during the start-up transient and steady state welding. No difficulties with the power supply shutting down were observed using the partly ground electrode. Consequently, all further welds produced in this study utilized the partly ground electrode. This electrode condition was also found to provide good consistency between results with minimal electrode deterioration. Therefore, the 2.4 mm diameter PAW torch orifice was selected for all further welds because it was found to have a tendency to reduce the weld width. It was thought that minimizing the weld width would be important as this would improve the melting efficiency of the process and help minimize residual stresses and weld distortion.

4.3 Joining Dissimilar Sheet Thicknesses

Double sided arc welding (DSAW) has not previously been applied to welding of dissimilar thickness sheet in the butt-joint configuration for tailor welded blank (TWB) applications. The following investigation was performed to identify the range of acceptable welding parameters for joining 1.0 mm thick 5182 aluminum alloy sheet to 1.5 mm thick sheets of the same material grade. The mechanical properties of the welds were evaluated using micro-hardness and tensile testing. Metallographic analysis and SEM-EDS were used to characterize the solidification structure of the weld.

4.3.1 Range of Suitable Welding Conditions

As described in Section 3.3, a series of welds were produced using total welding powers from 1.8 to 4.6 kW and at travel speeds between 10 and 70 mm/s. These welds were used to identify the range of acceptable welding conditions for joining 1.0 to 1.5 mm

thick 5182 aluminum sheet. The range of welding speeds and powers that produced visually acceptable DSAW welds is shown in Figure 4.15. In general, the welding speed increased with increased welding power. The maximum welding speed that produced acceptable welds was 70 mm/s and was attained when using a welding power of 4.6 kW. For each welding power a minimum welding speed was found to exist. Below this welding speed blowholes were created due to excessive heat input. Slightly lower heat inputs created excessively wide welds (greater than 10 mm) that exhibited centerline cracks upon cooling. As the speed was increased above the blowhole and centerline crack threshold, good welds were produced. The width of the good welds decreased as the welding speed was increased as a consequence of lower net heat input per unit distance during welding. A maximum welding speed was also found for each welding power. Above, the maximum welding speed, inconsistent arc coupling was observed and an inconsistent weld bead was produced. The net heat input for acceptable quality welds was found to be between 60 and 110 J/mm.

The top and bottom weld surfaces of welds produced with 2.6 kW total welding power at welding speeds from 10 to 50 mm/s are shown in Figure 4.16 and Figure 4.17, respectively. As the welding speed increased, the top and bottom weld widths decreased as a result of decreasing net heat input per unit distance to the weld. The wide welds produced at 20 mm/s did not show any cathodic etching beyond the edge of the top weld surface or fusion boundary. This suggests that the weld width has exceeded the width of the arc between the weld pool and the PAW torch. Welds produced at 30 and 40 mm/s showed evidence of cathodic etching beyond the weld on both the top and bottom surfaces of the base metal and in both cases, good consistent welds were obtained. The
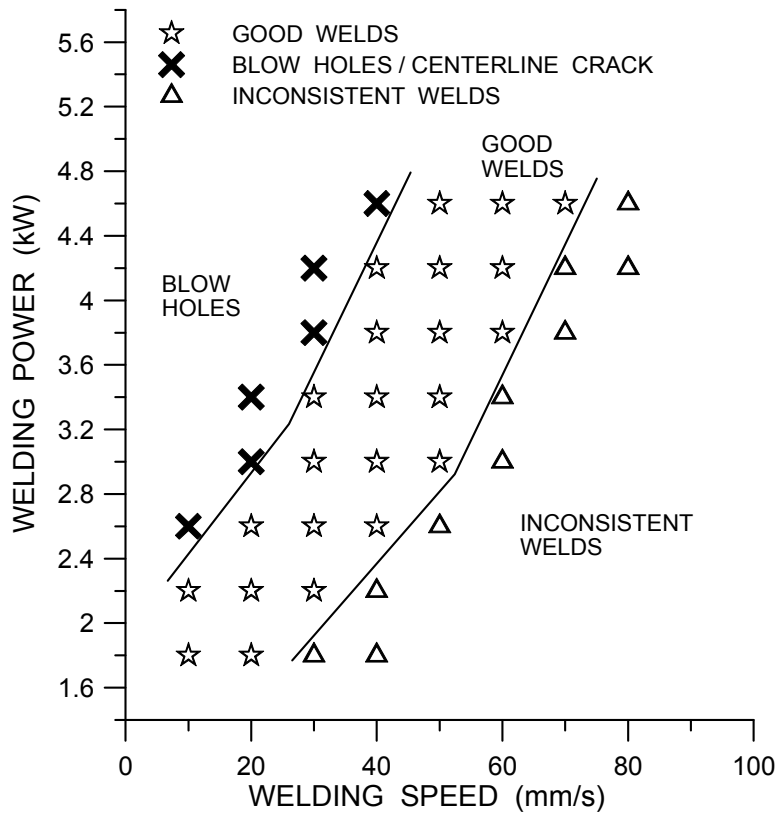
Figure 4.15: Range of visually acceptable welding conditions for joining 1.0 to 1.5 mm 5182 aluminum alloy sheet.

welds produced at 50 mm/s were erratic with inconsistent arc coupling and cathodic cleaning of the oxide. As well, a few locations can be observed where the original faying surface of the weld joint was not melted resulting in lack of fusion of the sheets.

The surfaces of the welds produced in this experiment exhibited black spots along the weld center line on the top and bottom weld surfaces as can be seen in Figure 4.16 and Figure 4.17. Leong *et al.* [74] also reported the formation of dark black spots on the surface of their laser welded 5182 aluminum alloy sheets. They identified these regions to be rich in magnesium and oxygen using energy dispersive x-ray spectroscopy. For this reason, the black spots observed on weld surfaces in this study are believed to be

(a)

(b)

(c)

(d)

(e)

Figure 4.16: Top surfaces of welds made using a constant power of 2.6 kW and welding speeds: (a) 10 mm/s, (b) 20 mm/s, (c) 30 mm/s, (d) 40 mm/s, (e) 50 mm/s.

90
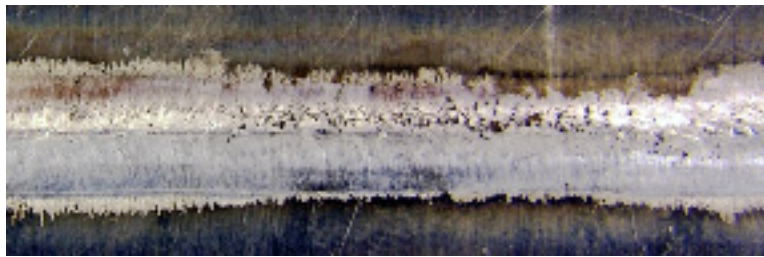
Figure 4.17: Bottom surfaces of welds made using a constant power of 2.6 kW and welding speeds: (a) 10 mm/s, (b) 20 mm/s, (c) 30 mm/s, (d) 40 mm/s, (e) 50 mm/s.

magnesium oxides. As welds with these black spots did not show poor strength (as will be shown later), they were not deemed to be weld defects and no further analysis was completed to confirm their identity.

Cathodic etching was observed along the edge of the weld similar to that observed during the torch standoff study and in previous DSAW studies by Kwon [29] and Anousheh [32]. However, the cathodically etched regions on either side of the weld were not symmetric for welds produced on a dissimilar sheet thickness combination of 1.0 to 1.5 mm thick sheets. The cathodically etched region was generally wider on the thicker 1.5 mm sheet than on the thinner 1.0 mm sheet. Top and bottom weld surfaces that illustrate this effect are shown in Figure 4.18. Both the top (PAW) and bottom (GTA) weld surfaces showed preferential etching of the surface of the thick sheet with the latter being the most pronounced. This trend was observed at all welding powers used in this study; however, the effect was less dominant on welds with widths greater than 8 or 9 mm. Above this weld width, very little etching was observed beyond the weld edge, likely due to the weld pool exceeding the width of the welding arc.

The preferential cathodic etching observed is believed to be caused by arc attraction to the edge of the 1.5 mm sheet. With the top surfaces of the sheets aligned in the clamping fixture, the bottom edge of the thick sheet will be closer to the GTA electrode creating a shorter path for the current travel which in turn causes the arc and cathodic etching to favour the bottom surface of the thicker sheet. The less pronounced preferential etching of the top surface of the thick sheet can be attributed to the narrower and more focused plasma arc and the flush alignment of the top sheet surfaces during welding.
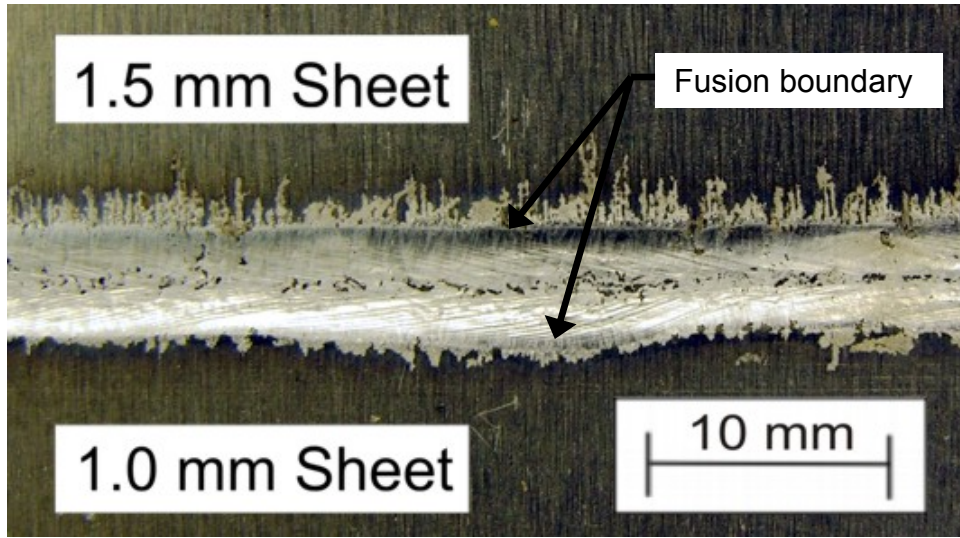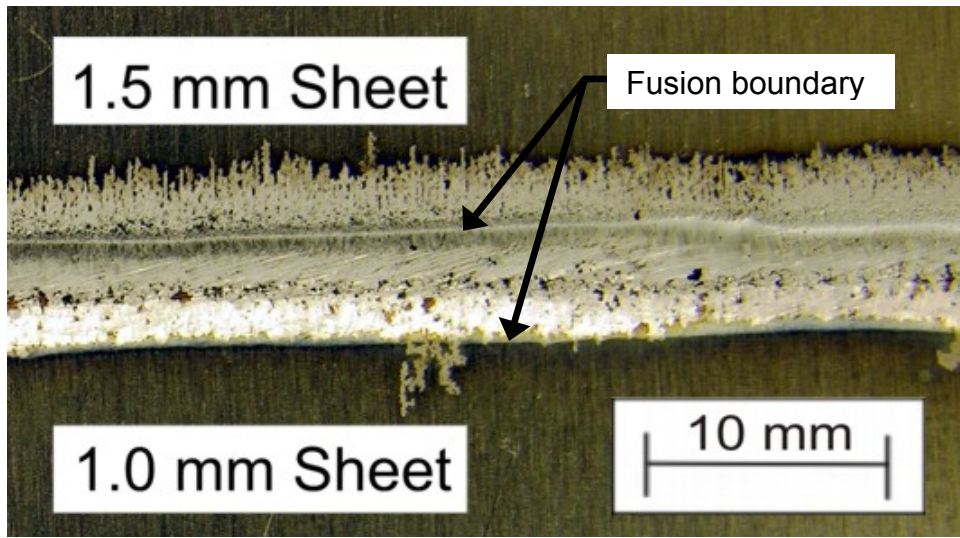
Figure 4.18: Preferential cathodic etching of the thick sheet is observed on: a) the top weld surface and b) the bottom weld surface.

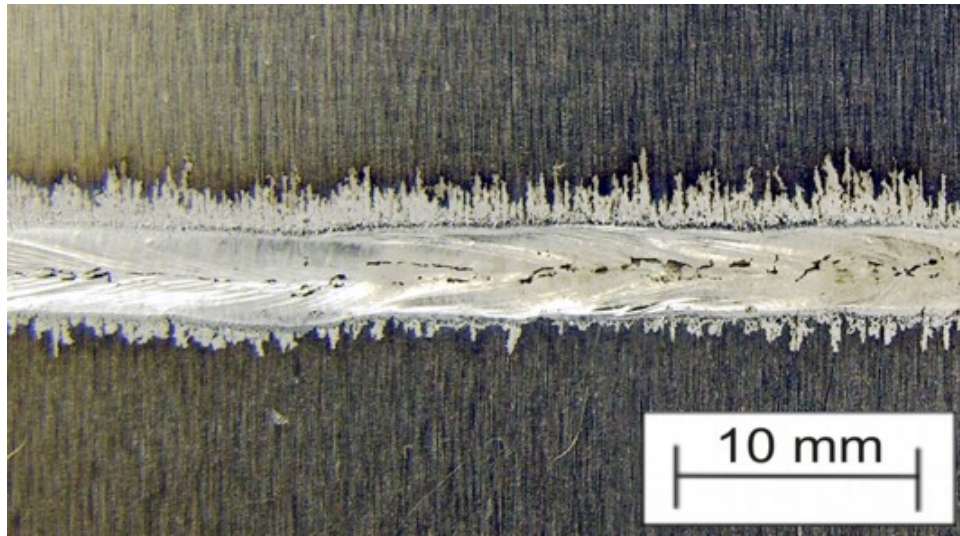The transition to inconsistent welds at higher welding powers was observed to be limited by the stability of the bottom (GTA) weld. Representative images of the top and bottom weld surfaces of an inconsistent weld are shown in Figure 4.19. It is seen that the top weld produced by the PAW torch exhibits a fairly consistent bead with minimal wandering. Meanwhile, the bottom weld shows that cathodic cleaning, the weld pool and fusion were inconsistent along the length of the weld. These results can be explained by the balance of power between the two welding torches. The PAW arc is longer due to the electrode set-back in the torch resulting in a greater voltage between the PAW torch and the work-piece than the voltage between the GTAW torch and the work-piece. Voltage measurements obtained for welds produced at a 3.0 kW total welding power indicated that the PAW torch-to-work-piece voltage was 64% of the total arc voltage between the two welding torches. Consequently, the welding power is split 64% to the top of the weld and 36% to the bottom for the constant current and balanced waveform used in this study. The lower power input to the bottom weld explains why the bottom weld was the limiting case for the transition from good to inconsistent welds. This observation also suggests that the upper limit for welding travel speed could be increased if a DSAW system with two PAW torches was used to provide an equal power split between the top and bottom welds.

4.3.2 Effects of Welding Torch-to-Joint Alignment

A series of tests were carried out to evaluate the weld quality and bead geometry of welds produced with the welding torches offset from the joint centerline. This was done because it was thought the weld bead might be improved by concentrating the heat towards the thicker sheet to promote additional melting of the thicker sheet and to

(a)

Lack of Fusion
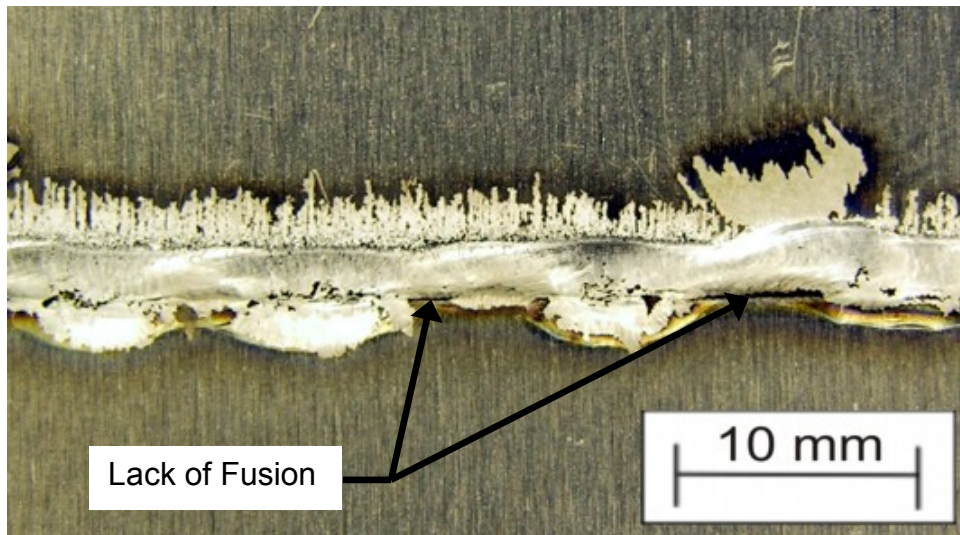
(b)

Figure 4.19: Representative weld showing that the transition from acceptable to inconsistent quality welds was not controlled by: a) the top PAW weld but instead by b) the bottom GTAW weld.

provide the weld metal required to provide a smooth transition from the thick to the thin sheet. In this study, a positive welding torch offset indicates that the welding torches were focused on the thicker sheet, negative offset indicates the torches were focused on the thinner of the two sheets and zero offset indicates the torches were aligned with the edges of the two sheets. The following five torch-to-joint configurations were used: -2 mm, -1 mm, 0, +1 mm, +2 mm.

Five welding conditions were examined to cover varying welding speeds and net heat inputs. Welds were made using 2.2 kW total welding power and speeds of 20, 24, and 30 mm/s (net heat inputs of 110, 92, 75 J/mm) to examine the effect of decreasing the heat input while varying the torch-to-joint alignment. The effect of varying welding powers was examined to investigate whether the torch-to-joint alignment was influenced by the welding power. This was done using a constant net heat input of 75 J/mm with welding power and speed combinations of 3.0 kW at 40 mm/s, and 3.8 kW at 50 mm/s.

All of the welds produced with zero offset exhibited consistent, good quality weld beads similar to those described previously in Section 4.3.1. A torch-to-joint alignment of -1 mm produced blowholes in the thinner sheet along the faying surfaces of the two work pieces as shown in Figure 4.20. Very little melting of the thicker 1.5 mm sheet was observed indicating that minimal heat transfer to the thicker work-piece was occurring. The cause of the blowholes was initially suspected to be simply a result of applying excessive heat to the thinner work-piece; however, Kwon [29] and Anousheh [32] both reported successful welding of 1 mm and 1.15 mm thick sheet at the same welding powers and travel speeds. As a result, excessive heat input does not seem to be the sole cause of the blowholes that were observed.
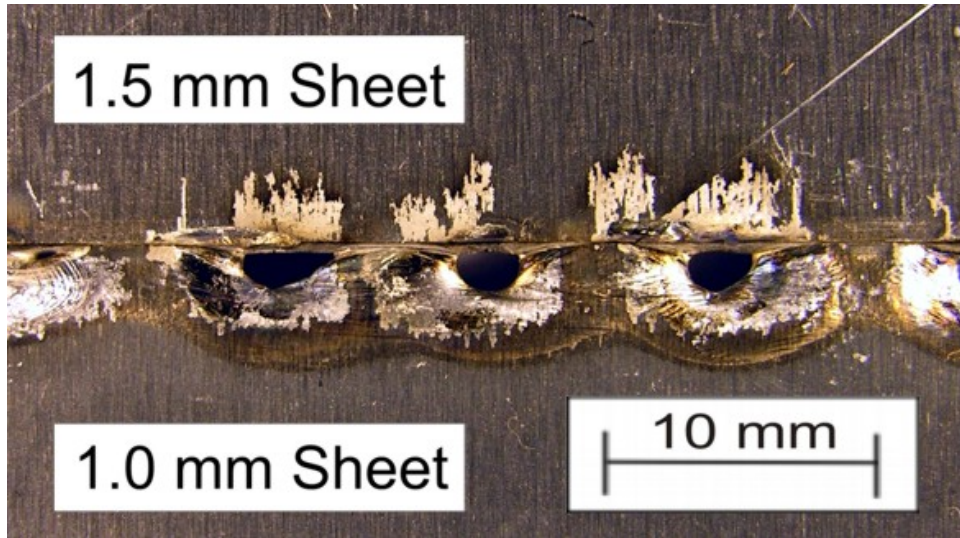
Figure 4.20: Top weld surface produced with welding torches offset 1 mm towards the 1.0 mm thick sheet resulting in blowholes using a net heat input of 75 J/mm.

With the welding torches centered over the thin sheet, very little heat from the welding arc is being transferred to the thick sheet. As the thin sheet starts to melt and form a molten weld pool, surface tension will prevent wetting of the surface oxide on the cold thick sheet. As a result, very little heat conduction will occur from the weld pool to the thick sheet. This will lead to rapid overheating of the thinner sheet causing an excessively wide weld pool and the formation of blowholes. Once the blowhole has been created, the DSAW welding arc will preferentially travel through the hole as this provides the path of least resistance between the welding torches [30]. This will temporarily limit the heat transfer to the weld pool leading to a pattern of blowholes separated by regions with very little melting, similar to the weld shown in Figure 4.20. The same blowhole trend was also observed with a torch-to-joint alignment of -2 mm for welds produced with a net heat put of 75 J/mm.

Examining the bottom surfaces of the welds produced at torch-to-joint alignments of -1 mm and -2 mm, shown in Figure 4.21, it is observed that the cathodic etching on the thicker 1.5 mm sheet was not reduced by moving the welding torch away from that sheet. The cathodic cleaning on the bottom of the thicker work-piece was actually better than that observed on the thinner work-piece. This evidence further supports the attraction of the welding arc to the sharp edge that exists due to the difference in material thicknesses. However, the arc attraction does not appear to transfer sufficient heat to the thicker piece to cause melting.
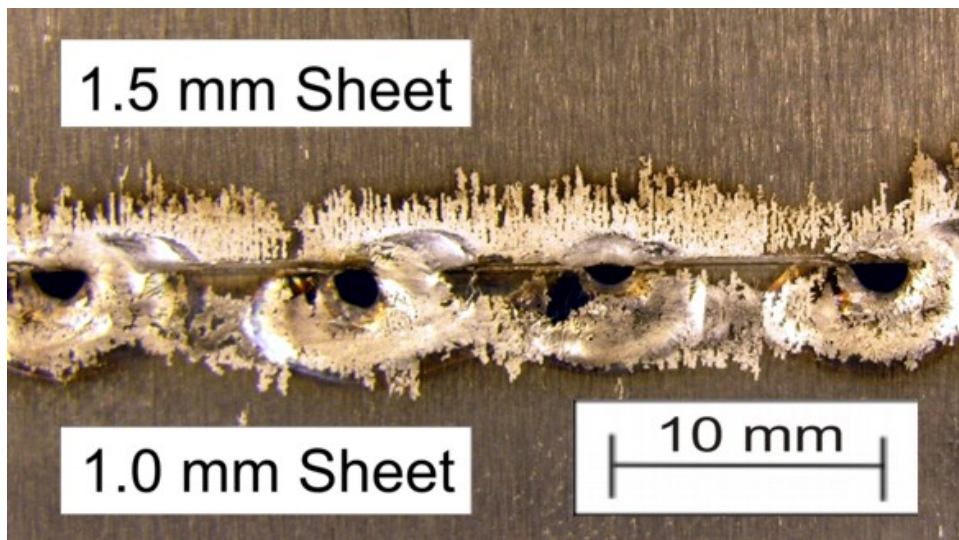
Figure 4.21: Substantial cathodic etching is observed on the bottom of the 1.5 mm sheet despite the welding torches being centered over the 1.0 mm sheet at a distance of 2 mm from the joint centerline.

Torch-to-joint alignments in the positive direction for welds produced with a net heat input of 75 J/mm showed a different trend than welds with torch-to-joint alignments in the negative direction. A torch offset of +1 mm produced an acceptable quality weld as can be seen in Figure 4.22. The weld bead was offset onto the thicker sheet; however,

98
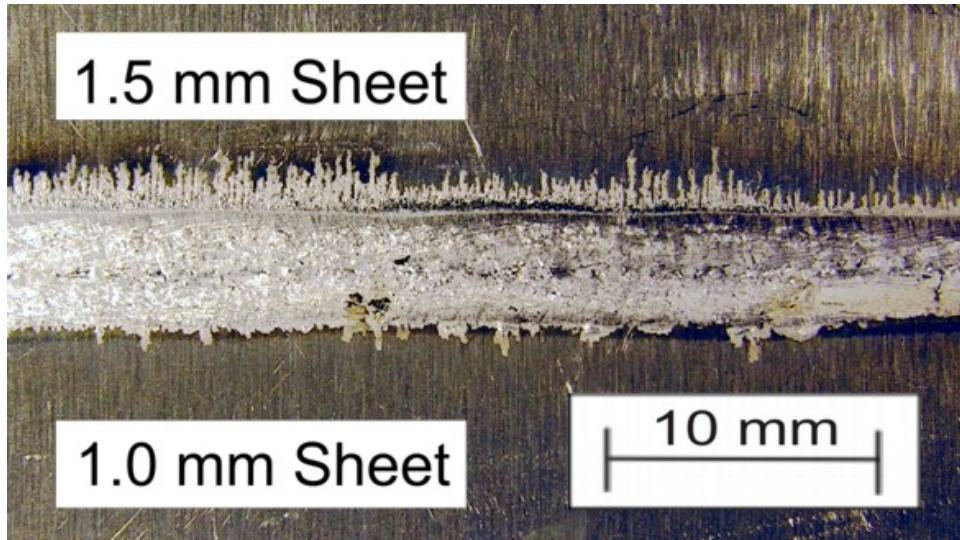
(a)
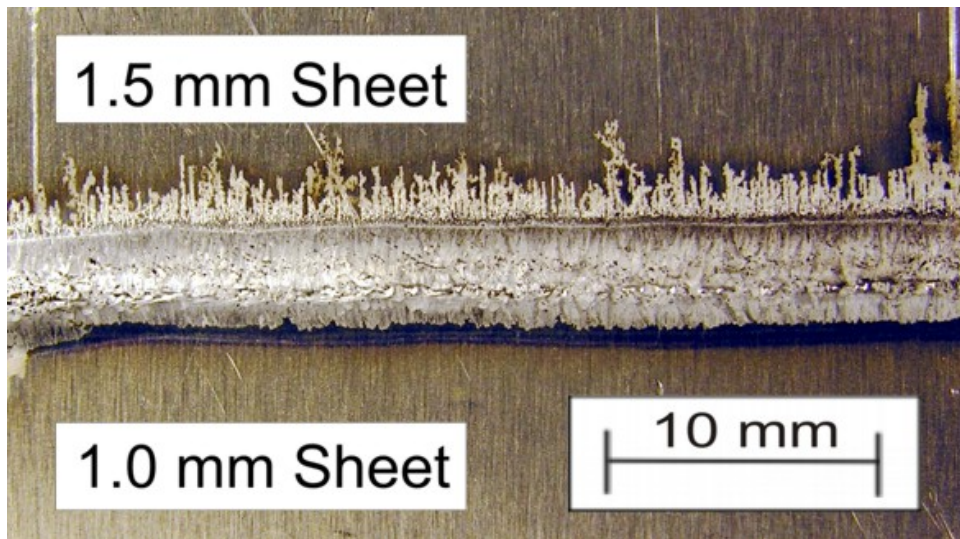
(b)

Figure 4.22: Good quality weld produced with a net heat input of 75 J/mm and the welding torches offset towards the 1.5 mm sheet by 1 mm, showing a) top weld surface and b) bottom weld surface.

the edge of the 1.0 mm sheet was melted during welding and a consistent weld bead produced along the length of the weld. Offsetting the torches even further to +2 mm produced a similar result as torch-to-joint offsets in the negative direction. This is shown in Figure 4.23. Melting occurred primarily on the thick sheet and a regular pattern of blowholes was produced. The occurrence of blowholes in this torch configuration is also believed to be caused by the failure of the weld pool to wet the opposing sheet, limiting heat conduction away from the weld and causing the thicker sheet to overheat.
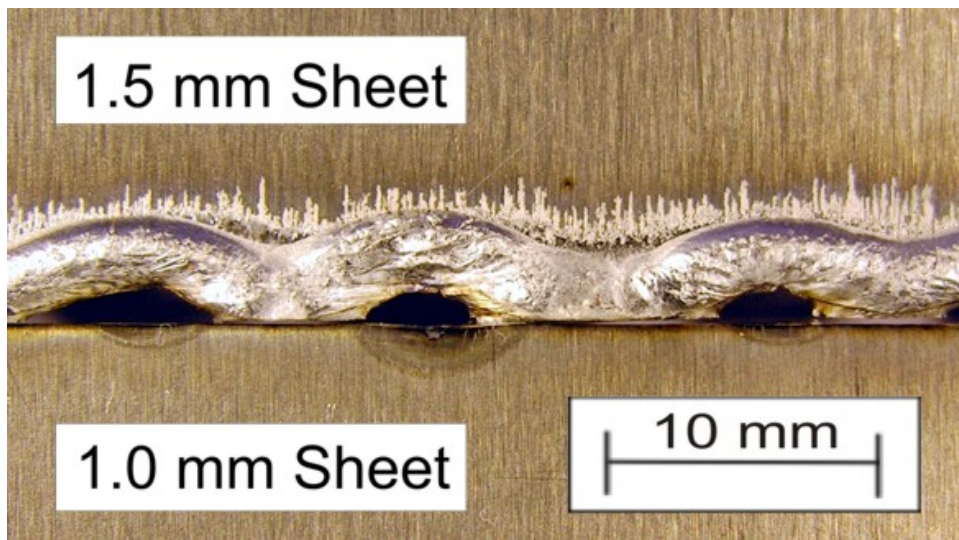
Figure 4.23: Top surface of a weld produced using a 75 J/mm net heat input and a 2 mm torch offset towards the thicker sheet showing blowholes from

Increasing the welding heat input to 92 J/mm and 110 J/mm was observed to increase the range of torch-to joint offset distances that produced acceptable welds. For torch-to-joint alignments of -1 mm, sufficient heat was input to the weld to cause melting of the thick sheet leading to the formation of a consistent weld pool and eliminating the blow through defect that was observed at a lower heat input of 75 J/mm. At a torch-to-

joint alignment of -2 mm, blowholes were again observed and limited melting of the thick work-piece occurred. Torch-to-joint alignments of +1 mm and +2 mm both produced good welds at the higher heat input; however, the welds were clearly centered on the thicker work-piece. The improvement in the torch-to-joint tolerance that was observed with increased heat input to the weld is attributed to the increased width of the weld pool which promotes heat transfer to the work-piece farthest from the joint. This allows a stable weld pool to be formed by melting both sheets during welding. The exception to this occurs when the torches are centered over the thin sheet. In this case, the torches and are too far from the joint for sufficient heat transfer to the thick sheet to occur before the thin sheet overheats.

For the 1.0 to 1.5 mm sheet thickness ratio examined above, no noticeable benefit was observed by offsetting the welding torches from the joint. Offsetting the welding torches from the joint had a tendency to cause welding defects; however, slight offsets towards the thick sheet were not detrimental to weld quality. Offsetting the welding torches towards the thicker sheet might be more beneficial when welding materials with a larger difference between sheet thicknesses; however, for the 1.0 to 1.5 mm thickness ratio used in this study, the best weld quality was consistently obtained when the welding torches and the welding joint were aligned with each other. As a result, all further welding for this thesis was carried out using a torch-to-joint alignment of zero millimeters.

4.3.3 Properties of Dissimilar Thickness DSA Welds

A detailed investigation was performed on the visually acceptable welds produced with 2.6 kW and 4.2 kW total welding power and different welding speeds as well as welds

produced at a constant speed of 40 mm/s but different welding powers (See Figure 4.15). These conditions were selected to examine the effects of welding speed and welding power on the weld dimensions, hardness and strength of the welds produced using a variety of welding conditions.

4.3.3.1 Weld Dimensions

The weld widths for top and bottom weld surfaces have been plotted in Figure 4.24 and Figure 4.25. The top and bottom welds were nearly identical in width for all welds produced with welding powers of 2.6 kW and 4.2 kW. There was also agreement in the top and bottom weld widths for welds produced at varying powers with a constant travel speed of 40 mm/s. For welds produced at 2.6 kW and 4.2 kW total welding power, the weld width decreased with increased travel speed. This effect is expected as increasing the travel speed will decrease the energy input to the weld per unit distance, causing a decrease in the volume of melted metal. Likewise, the weld widths shown in Figure 4.25 were wider when a greater welding power was used because an increase in welding power increased the net heat input per distance for welds produced at a constant travel speed. These results are in good agreement with the findings of Kwon [29] in her study on DSAW of similar thickness aluminum alloys.

4.3.3.2 Melting Ratio

The melting ratio is defined as the fraction of the total welding power used to melt the weld pool and can be used to compare the process efficiency for different welding
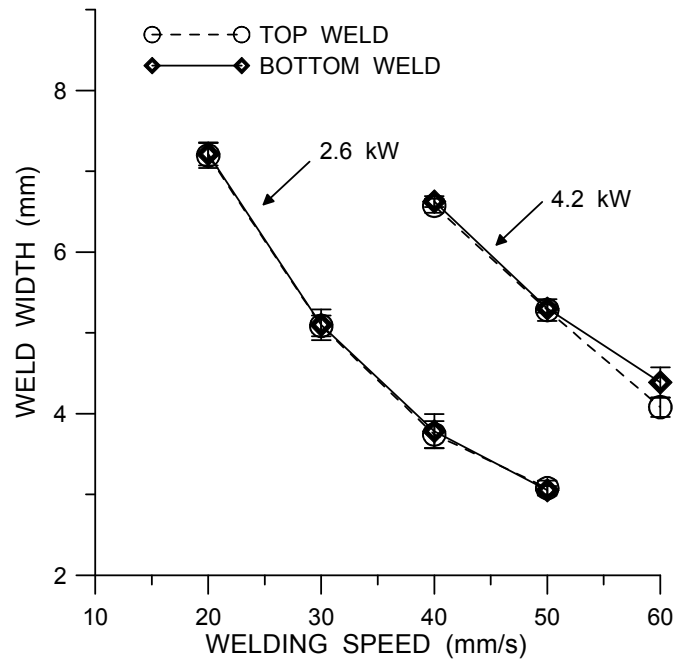
Figure 4.24: Top and bottom weld width versus welding speed for total welding powers of 2.6 kW and 4.2 kW.
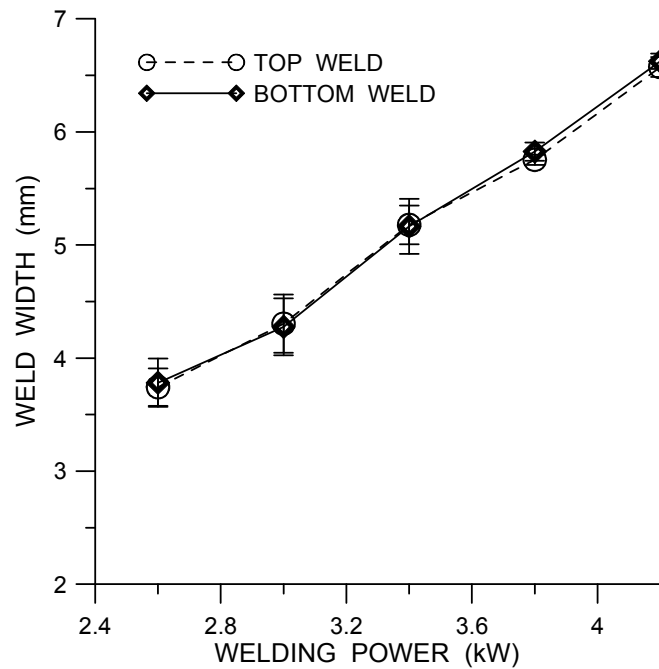

Figure 4.25: Top and bottom weld width versus welding power for a constant welding travel speed of 40 mm/s.

conditions. Melting ratio can be calculated using the following equation:

$$Melting\ Ratio = \frac{A_W \times V_W \times \rho \left(C_p \times \Delta T + \Delta H_f\right)}{P_W} \qquad (4.1)$$

where A_W is the cross sectional area of the weld, V_W is the welding speed, ρ is the density, C_p is the specific heat, ΔT is the difference between the liquidus temperature, T_l, and the ambient temperature prior to welding, ΔH_f is the latent heat of fusion, and P_W is the welding power. The thermal properties for 5182 aluminum alloys are listed in Table 3.2. The ambient temperature in the welding lab used for calculations was 295 K.

Figure 4.26 shows the melting ratio versus welding speed for total welding powers of 2.6 kW and 4.2 kW. For welding powers of 2.6 kW and 4.2 kW, the melting ratio shows a decreasing trend as the welding speed increases. The decrease in melting ratio also coincides with the transition towards inconsistent weld beads. For this reason, the decrease in melting ratio observed could be related to the inability of the arc to completely remove the surface oxide. An increase in the melting ratio was observed as the welding power was increased which is shown in Figure 4.26 and Figure 4.27.

The range of values found for the melting ratio in this study are notably higher than those reported by Deutsch [14] for PAW of the same alloy. In his study, melting ratios between 0.07 and 0.13 were found when using a polarity balance of 0.5 (equal electrode negative and positive powers) and $\theta = 0.5$ (equal time spent in electrode negative and positive). The increase in melting ratio observed with DSAW (for the same values of θ and polarity balance) is most likely due to the symmetric heating of the weld and the absence of a backing bar that was found by Deutsch [14] and Punkari [16] to act as a large heat sink during PAW of aluminum sheet. The melting ratio values obtained
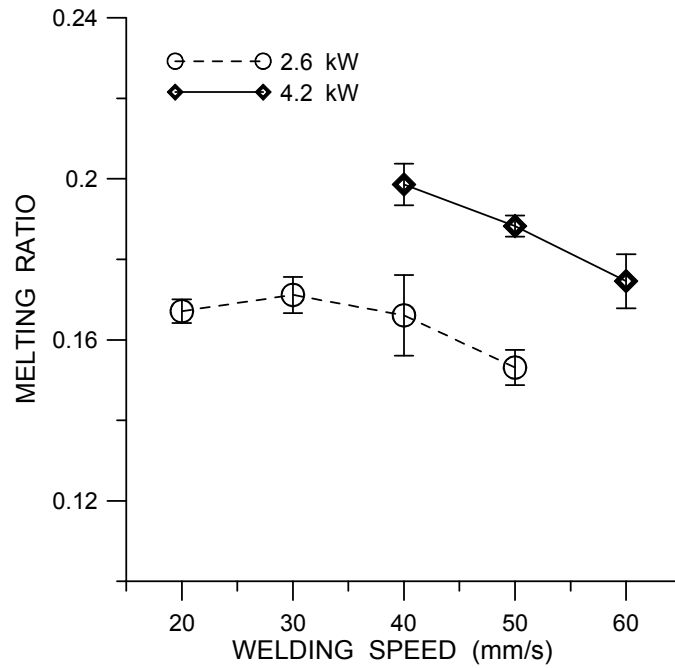
Figure 4.26: Melting ratio versus welding speed for welds produced with total welding powers of 2.6 kW and 4.2 kW.
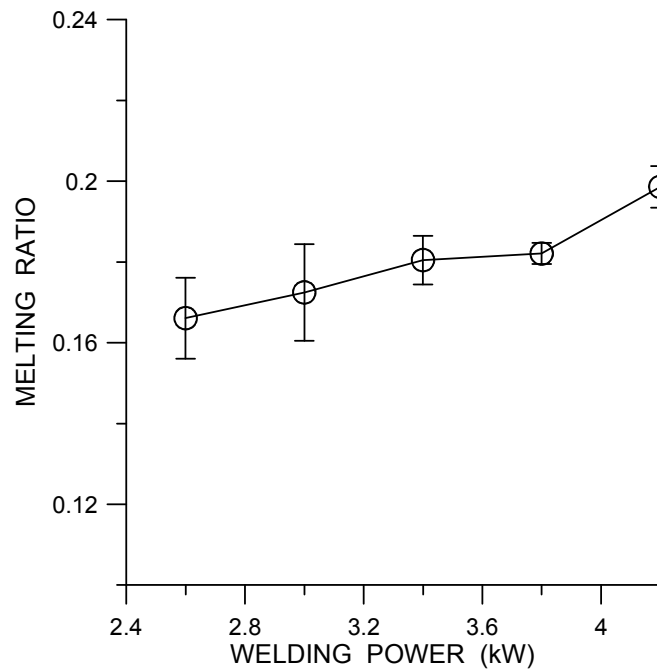

Figure 4.27: Melting ratio versus welding power for welds produced at a constant travel speed of 40 mm/s.

105

in this study also compare closely to values of 0.12 to 0.2 reported by Deutsch [14] and Punkari [16] for dual beam Nd:YAG laser welding of 5182 aluminum alloy sheet.
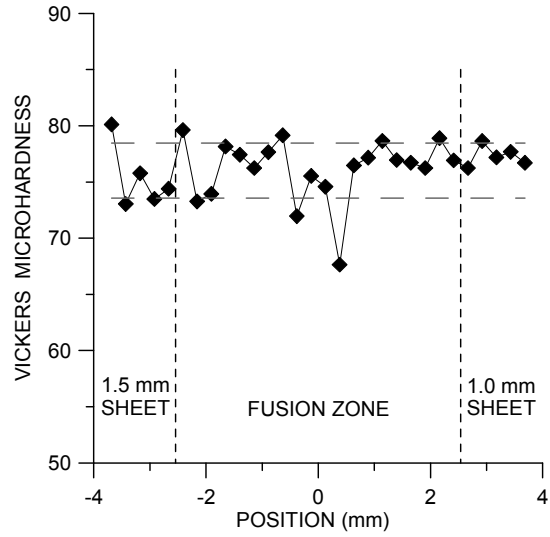
4.3.3.3 Microhardness

Vickers microhardness results for welds produced with a total welding power of 2.6 kW are presented in Figure 4.28. The hardness profiles show that the weld metal hardness closely matches that of the base metal. No noticeable increase in hardness was observed at the fusion boundary or across the weld metal. Also, no evidence of a softened heat affected zone was detected.

The lack of softening adjacent to the weld is not unusual for 5182-O aluminum alloys as it is not considered to be a heat treatable alloy [77]. Also, the material used in this study had been annealed and recyrstallized (O-temper) prior to welding, so softening would not be expected during welding. Some researchers [16,29] have reported increases in hardness at the weld fusion boundary when welding 5182 aluminum alloys. The slight increase in hardness was attributed to the formation of Mg_2Al_3 along the grain boundaries that can occur with elevated temperatures [77]; however, no evidence of this phenomena was observed in this study. The occasional low hardness measurements observed in the fusion zone in Figure 4.28 could be caused by hidden gas pores or solidification pores below the hardness indent, although this is not known for certain. The microhardness results of all specimens produced at a welding power of 4.2 kW and welds produced at varying powers at a constant speed of 40 mm/s were similar to those shown in Figure 4.28. These results have been included in Appendix A.
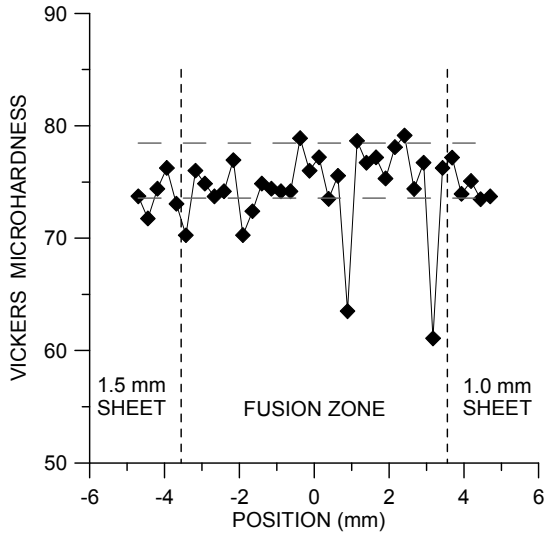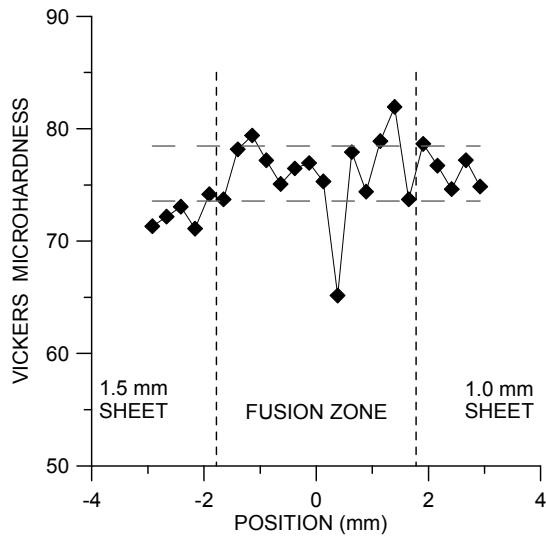
Figure 4.28: Vickers microhardness results for welds produced with a total welding power of 2.6 kW and welding speeds of: (a) 20 mm/s, (b) 30mm/s, (c) 40 mm/s, (d) 50 mm/s. The horizontal lines on each plot represent plus and minus one standard deviation of the average base metal hardness.

4.3.3.4 Tensile Strength

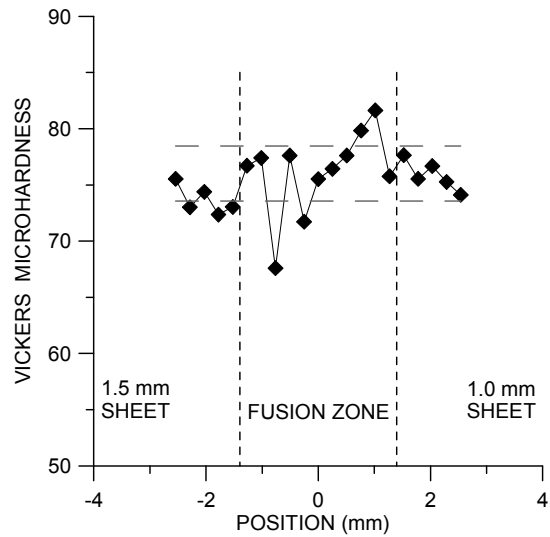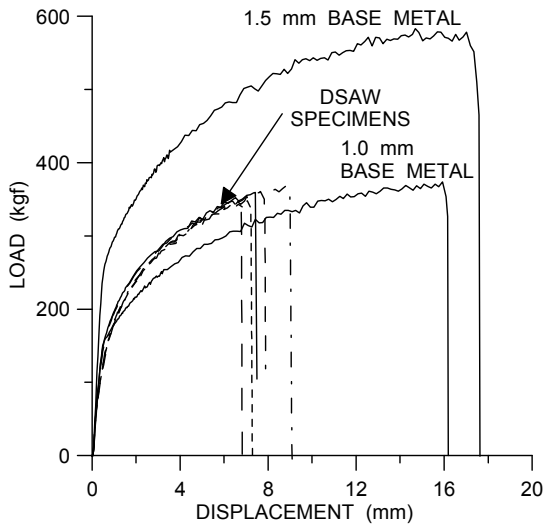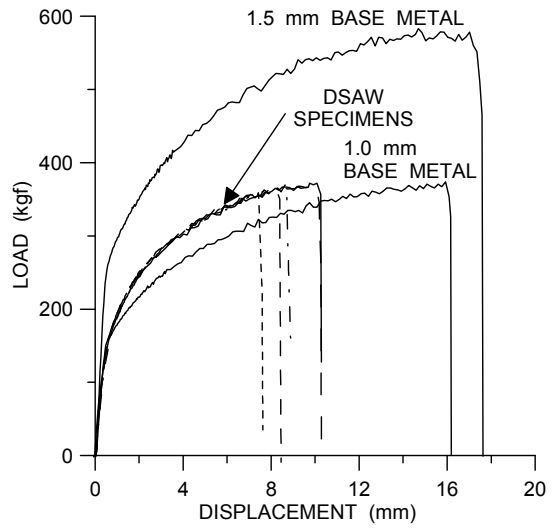Transverse tensile load-displacement curves have been used instead of stress-strain curves to analyze the strength of 5182 aluminum alloy TWBs produced with DSAW due to the three unique sections (1.0 mm thick sheet, 1.5 mm thick sheet, DSAW weld) contained in the gage length of the tensile specimen (see Figure 3.17). Transverse tensile load-displacement curves for welds produced at total welding powers of 2.6 kW and 4.2 kW are shown in Figure 4.29 and Figure 4.30. It can be seen that the yield and ultimate strengths of the DSAW weld specimens generally approach the strength of the thinner base metal; however, it can also be seen that the welds produced at 4.2 kW welding power and higher travel speeds of 50 mm/s and 60 mm/s show a notable decrease in tensile strength and displacement at failure. Specimen failure was observed to occur across the weld near the fusion zone centerline for all welding conditions

To make a more meaningful comparison of the weld strength, the joint efficiency has been used to compare the failure loads for welds produced under different welding conditions. In this study, the joint efficiency has been defined as the failure load of the welded specimens as a percentage of the failure load for the thinner parent material. Joint efficiency results are presented in Figure 4.31 for welds produced with constant powers of 2.6 kW and 4.2 kW, and Figure 4.32 for welds produced at a constant travel speed of 40 mm/s. These results indicate that joint efficiencies greater than 94% were attained for all welds produced at 2.6 kW and all welds produced at 40 mm/s (with welding powers between 2.6 kW and 4.2 kW). The joint efficiency of the welds produced at 50 and 60 mm/s using a welding power of 4.2 kW were significantly lower with the joint efficiency falling to 82% and 65%, respectively.

108
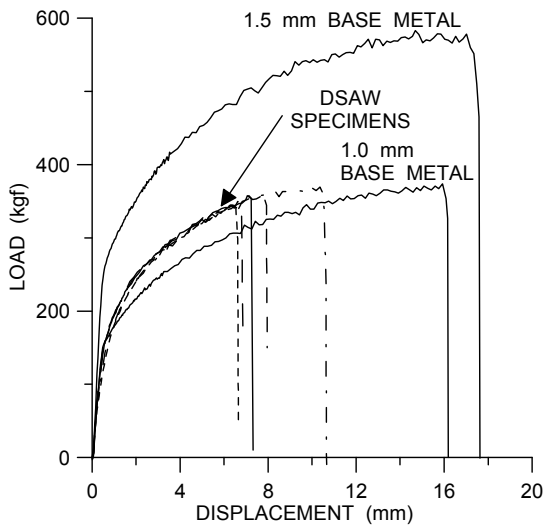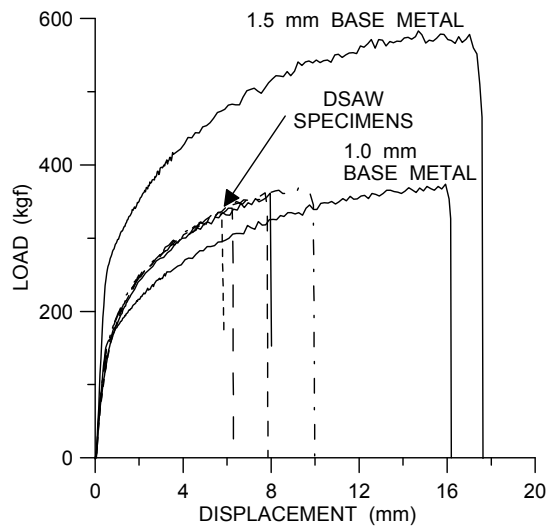
Figure 4.29: Load displacement curves obtained from transverse tensile tests of welds produced with 2.6 kW total welding power at travel speeds of (a) 20 mm/s, (b) 30 mm/s, (c) 40 mm/s, (d) 50 mm/s.
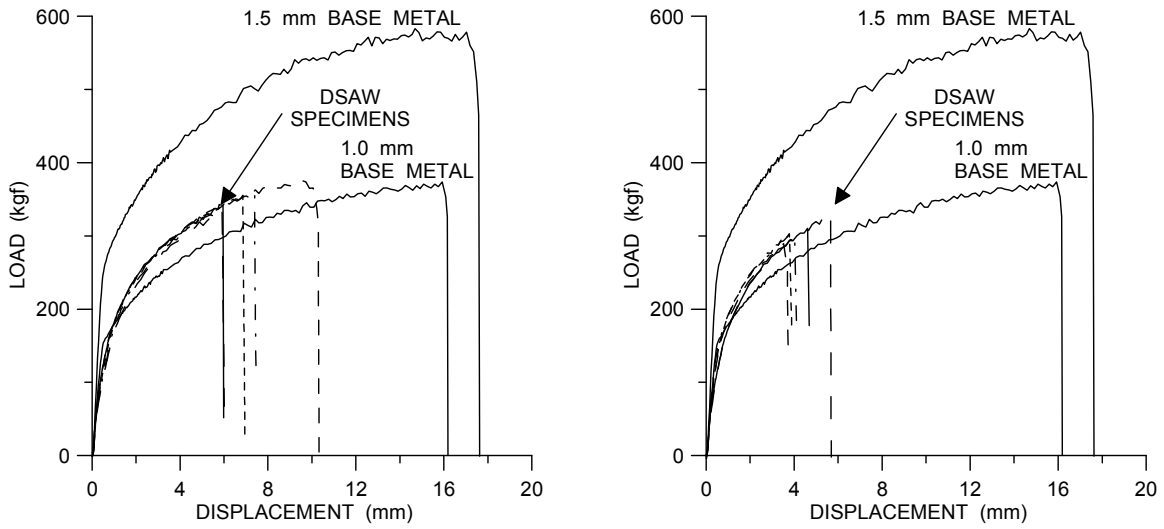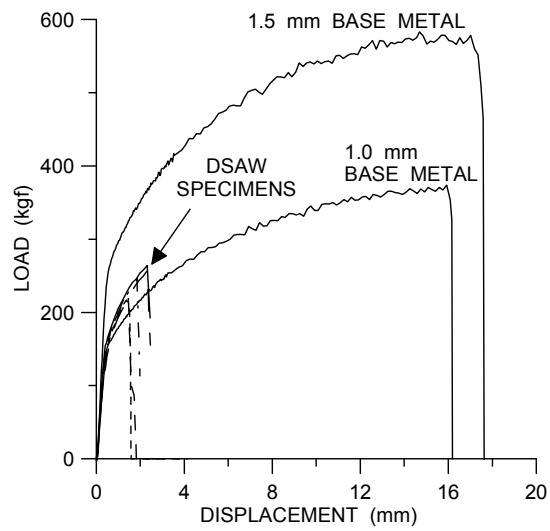
Figure 4.30: Load displacement curves obtained from transverse tensile tests of welds produced with 4.2 kW total welding power at travel speeds of (a) 40 mm/s, (b) 50 mm/s, (c) 60 mm/s.
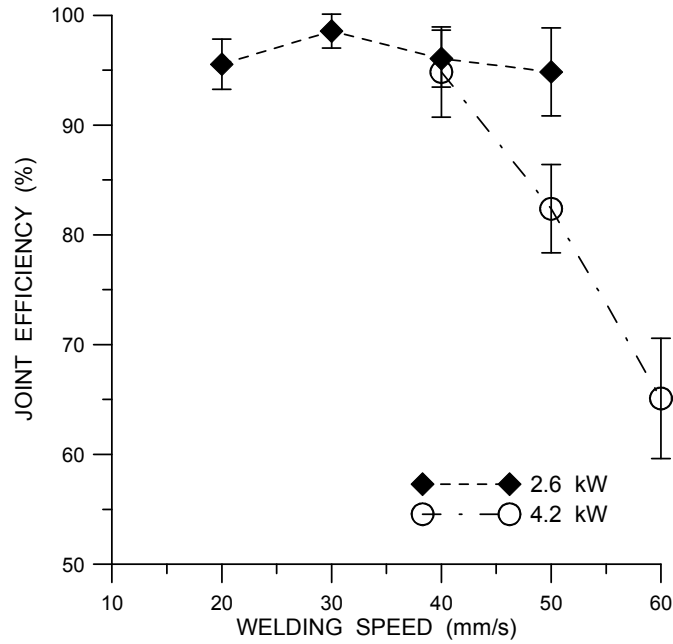
Figure 4.31: Transverse tensile joint efficiency for welds produced at total welding powers of 2.6 kW and 4.2 kW.
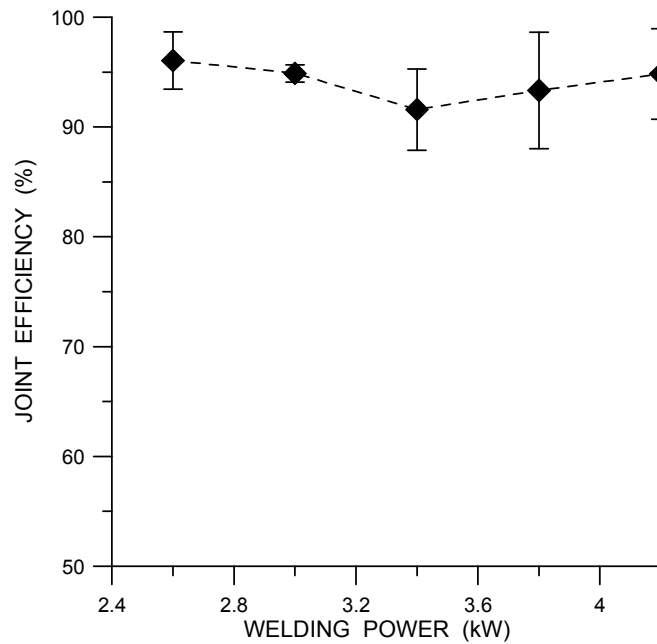
Figure 4.32: Transverse tensile joint efficiency for welds produced at a constant travel speed of 40 mm/s.

Due to the variation in thickness of the gage length of a tailor welded blank transverse tensile specimen (shown in Figure 3.17), quantitative comparisons between the weld metal ductility and the base metal can not be obtained from these tests. However, qualitative comparisons can be made regarding the ductility of the weld metal for specimens welded under different conditions by examining the load versus displacement plots shown in Figure 4.29 and Figure 4.30. All welds produced with a welding power of 2.6 kW showed comparable displacements at failure with the average ranging between 7 and 8 mm; however, the variance in the data was also found to increase with increasing welding speed. Similar results were obtained from the load displacement curves for welds produced at 40 mm/s for welds with welding powers between 3.0 and 3.8 kW. These results have been included in Appendix A. A very different trend is observed for welds produced with 4.2 kW total welding power (see Figure 4.30). The weld produced at 40 mm/s is comparable to the welds made 2.6 kW, but the welds produced at 50 mm/s and 60 mm/s show a definite decrease in the displacement at failure with results averaging around 2 mm for the 60 mm/s weld. These results suggest that a decrease in ductility accompanies the decrease in strength observed above a threshold welding speed between 40 mm/s and 50 mm/s.

4.3.4 SEM-EDS and Metallographic Analysis

The chemical composition was analyzed across the fusion zone of welds using a scanning electron microscope (SEM) with energy dispersive spectrometry (EDS). This was done to look for variations in magnesium concentrations between welding conditions that could account for the decrease in transverse tensile strength observed in welds produced at high welding speeds. 5000 series aluminum alloys derive their strength from solid

solution strengthening with magnesium additions and the loss of magnesium during laser welding has been shown to result in a loss of strength [19]. Therefore, it was of interest to determine if DSAW had an influence on the resulting magnesium concentration of the fusion zone that could explain the differences in strength observed for varying welding conditions.

Four welds were examined by performing EDS line scans across the fusion zone. The specimens analyzed were produced at welding speeds of 20 and 50 mm/s using 2.6 kW total welding power and welding speeds of 40 and 60 mm/s when using 4.2 kW total welding power. Figure 4.33 and Figure 4.34 show the location of EDS measurements and their respective magnesium readings for welds produced with 2.6 kW total welding power at a speed of 50 mm/s and 4.2 kW total welding power at a speed of 60 mm/s. It can be seen in the accompanying magnesium plots that the magnesium concentration is consistent across the weld. These results are also consistent with the nominal 4.5 weight percent magnesium content in the 5182 aluminum alloy [70].

The average magnesium concentrations measured across the base metal and fusion zone for each of the four specimens are summarized in Table 4.2. The differences observed between the mean base metal and the mean weld metal magnesium content were examined for a significant statistical difference using a t-test, at a 95% significance level, to test the null hypothesis that mean magnesium concentration was equal across both the base metal and fusion zone. No significant difference between means was found using the t-test. This suggests that no appreciable magnesium loss occurs during DSAW of 5182 aluminum alloys over a range of welding conditions. These results are in contrast to a study of Nd:YAG laser welding of 5182 aluminum alloys by Pastor
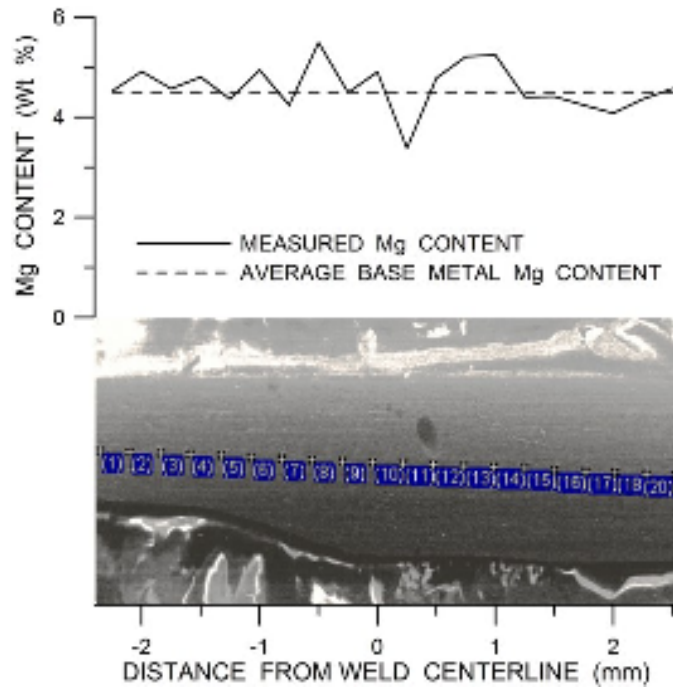
Figure 4.33: Test locations and results for SEM-EDS analysis to identify magnesium content across a weld produced with 2.6 kW total welding power at a speed of 50 mm/s.
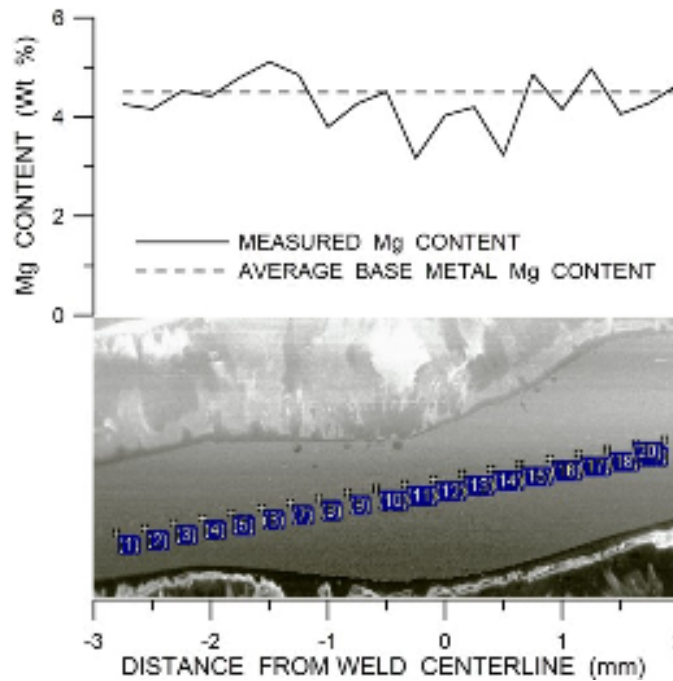
Figure 4.34: Location and results of SEM-EDS analysis examining magnesium content across a weld produced at 4.2 kW total welding power and 60 mm/s.

Table 4.2: Magnesium contents measured using SEM-EDS for welds produced with total welding powers of 2.6 kW and 4.2 kW.

Welding Conditions:	Test 1	Test 2	Test 3	Test 4
Power (kW)	2.6	2.6	4.2	4.2
Speed (mm/s)	20	50	40	60
Base Metal Mg Content:				
Average (Wt. %)	4.48	4.50	4.68	4.40
Std. Dev.	0.41	0.26	0.20	0.20
# Data Points	12	9	11	5
Fusion Zone Mg Content:				
Average (Wt. %)	4.23	4.68	4.58	4.29
Std. Dev.	0.50	0.59	0.79	0.59
# Data Points	29	11	26	15
Statistical Calculations:				
Pooled Variance	0.47	0.47	0.67	0.53
Degress of Freedom (DF)	39	18	35	18
T_{obs}	1.49	0.85	0.38	0.43
$t_{(0.95,DF)}$	2.02	2.10	2.03	2.10

et al. [19], who reported magnesium losses between 0.74 and 1.20 weight percent across the fusion zone, for keyhole and conduction-mode Nd:YAG laser welds. The higher energy density of Nd:YAG laser welding compared to DSAW is believed to be responsible for the differences between this study and the study by Pastor *et al.* [19]. Also, no published literature could be found to support the occurrence of magnesium losses during arc welding of aluminum alloys. For these reasons, further studies on the composition of the weld metal were not deemed to be necessary and magnesium loss was not considered to be responsible for the decrease in tensile strength observed in welds produced with a total welding power of 4.2 kW at 50 and 60 mm/s. The lack of magnesium loss during DSAW is also thought to be advantageous for TWB applications where the retention of weld metal strength has been found to be important for post weld forming [69,73].

Metallographic analysis was performed on transverse cross sections of welds that were produced under a variety of welding conditions, with emphasis on the same conditions used for tensile and micro-hardness testing. Examination of metallographic specimens revealed that welds produced under all conditions exhibited porosity similar to the specimens shown in Figure 4.35. These round spherical pores are believed to be caused by hydrogen gas, as this is the dominant cause for gas porosity in aluminum alloys [62,63,64]. Hydrogen is expelled into the molten weld pool as solidification occurs, caused by the rapid decrease in hydrogen solubility of solid aluminum compared to molten aluminum. The solubility limit of the molten weld pool is then exceeded, promoting the nucleation and growth of gas bubbles. Although the bubbles tend to be buoyant, solidification tends to freeze the bubbles in place before they can reach the surface. Magnesium vapours have also been reported to cause spherical occluded vapour pores in laser welded aluminum alloys [19]. This is not expected to be a problem with DSAW as magnesium vapour pores would likely be accompanied by a decrease in magnesium content in the fusion boundary caused by vaporization near the surface of the weld pool; however, no evidence of magnesium vaporization or loss was found in this study as previously discussed.

Porosity formation during DSAW of 10 mm thick aluminum plate was not reported to be a problem by Zhang *et al.* [26]. They also reported that no precautions or material preparation were employed in their study to prevent porosity. The contrast between porosity content in the present study and the study by Zhang *et al.* [26] is believed to be caused by the difference in welding position and the welding speeds employed. Zhang *et al.* [26] produced welds in the vertical-up progression. Up-hill
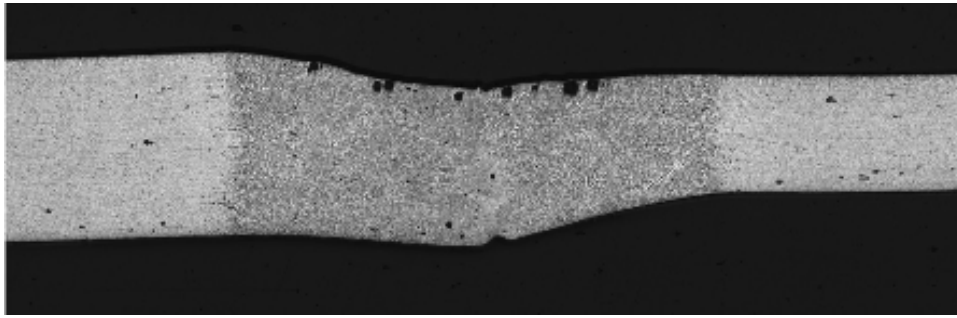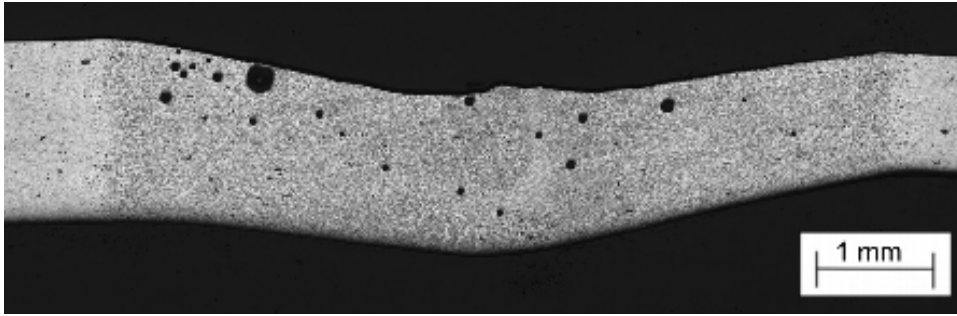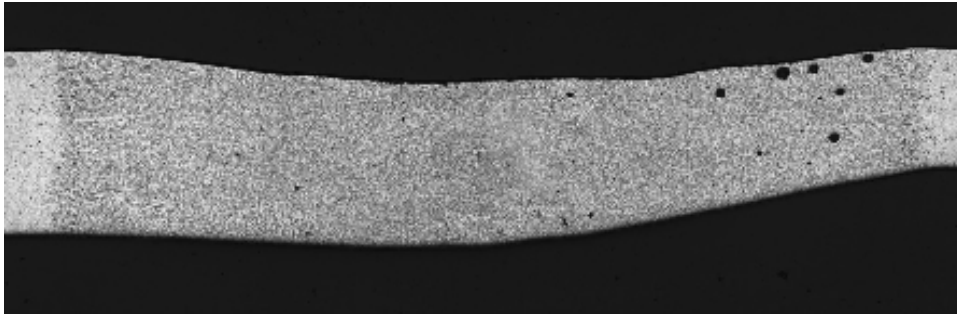
Figure 4.35: Metallographic cross sections showing porosity in welds produced with the following welding conditions: a) 2.6 kW and 20 mm/s, b) 3.0 kW and 40 mm/s, c) 4.2 kW and 40 mm/s.

welds have been shown to reduce porosity by minimizing the distance between the solidification front and the pool surface that a pore must travel to escape from the pool surface [64]. The welding speeds used by Zhang *et al.* [26] to make full penetration butt welds were limited to a maximum speed of 2 mm/s, much slower than the speeds between 20 and 60 mm/s used in this study. As a result, the gas pores formed in the present study on thin sheet aluminum alloys had very little time to escape from the weld pool compared to thick plate applications. These observations indicate that controlling hydrogen porosity is critical when welding thin gauge materials that permit higher welding speeds to be used than thicker plate materials.

The volume fraction of porosity in the weld metal was inferred by measuring the area fraction of porosity on three transverse sections for each welding condition that tensile testing was performed on. The results are shown in Figure 4.36 and Figure 4.37. The average porosity levels ranged between 0.25 and 1.0 volume percent porosity for all the welding conditions examined. No clear trends were identified between welding conditions as a great deal of scatter existed in the data; however, this scatter is not unexpected as metallographic porosity measurements do not consider the same proportion of a weld as density or radiographic testing methods [63].

Despite the scatter in the data collected, these porosity measurements did not exceed a threshold value of 1-2 volume percent porosity that has been shown to be the upper limit of porosity that can be tolerated in aluminum alloy welds, without decreasing of the strength of the weld metal [57,58]. This is in close agreement with the tensile results obtained in this study where it was found that the joint strengths approached that of the base metal. Welds produced using a total welding power of 4.2 kW at 50 and
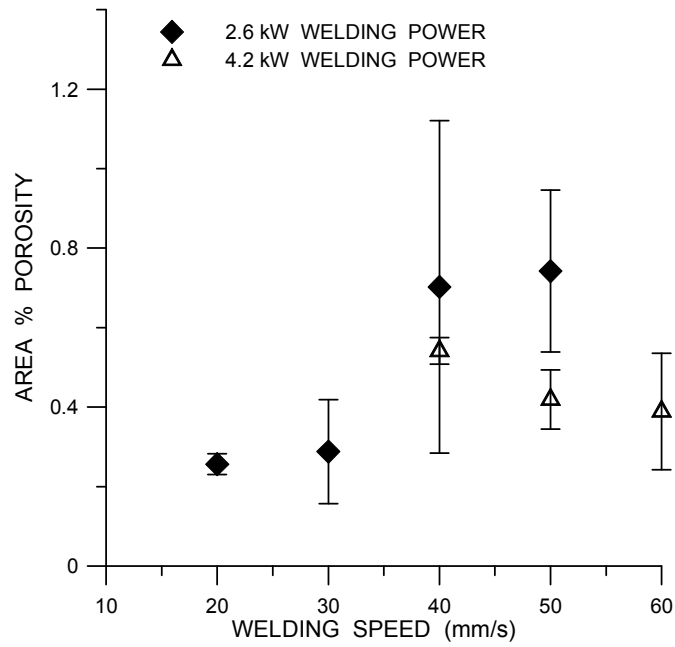
Figure 4.36: Weld metal porosity volumes for weld specimens produced using total welding powers of 2.6 kW and 4.2 kW.
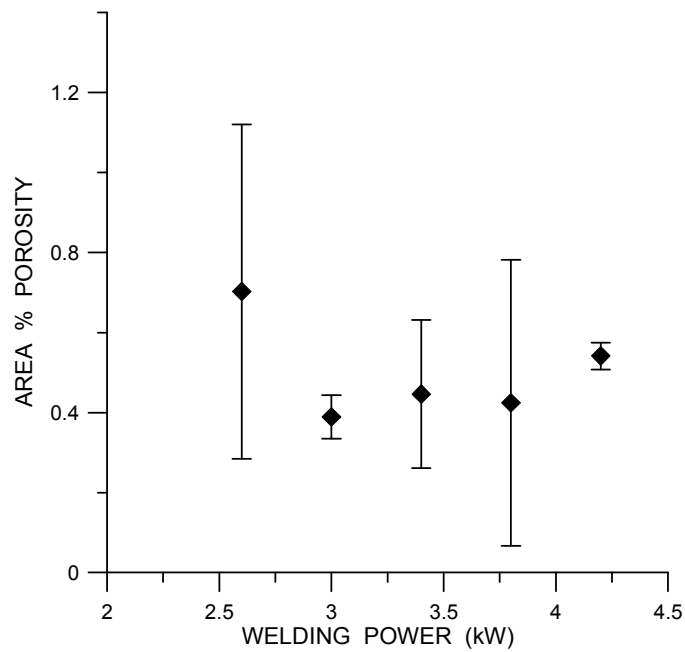

Figure 4.37: Weld metal porosity volume for weld specimens produced using a constant travel speed of 40 mm/s.

60 mm/s were the only exceptions. The cause for the decrease in weld strength at these welding speeds is not clear.

The Canadian Standards Association (CSA) W59.2 standard for welded aluminum construction permits a maximum weld metal porosity of 0.1% area fraction in radiographic testing, for applications using sheet material with a thickness below 3 mm [84]. This tolerance is well below the measured porosity contents found in the welds produced in this study. Although the W59.2 welding code is not applicable to automotive applications, it is thought that the hydrogen porosity content must be reduced for automotive TWB applications to ensure consistently high quality and strength welds are attained.

Furthermore, weld metal ductility has been shown to be much less tolerant of porosity and can be reduced by very small amounts porosity [57,59]. As a result, it was determined that the welding procedure needed to be optimized to minimize the formation of hydrogen gas pores. Without addressing the porosity concerns, an analysis of the ductility and forming properties of TWBs produced with DSAW would have a negative bias and little value. To overcome the porosity, mechanical cleaning of the surface oxide was evaluated as will be presented in the following section.

4.4 Effects of Wire Brushing Prior to Welding

Stainless steel wire brushing of aluminum specimens prior to welding has been proven to be effective in reducing the thickness of the oxide layer with particular emphasis on removing hydrated oxides that have formed during extended storage periods [64,65]. Two main benefits can be achieved: hydrogen porosity can be significantly reduced and the stability of the weld pool is increased [23,64]. The reduction in porosity occurs as a

result of removing the hydrated surface oxides that would otherwise dissociate in the welding arc and expose the weld pool to a source of hydrogen gas. The weld pool stability arises from the reduction in cathodic cleaning that must take place to successfully remove the surface oxide and facilitate coupling between the arc and the weld metal. However, the need for cathodic cleaning is not eliminated by stainless steel wire-brushing as the aluminum oxide will quickly form a thin new layer during the time lapse between brushing and welding.

To examine the effects of wire-brushing on the weld quality and hydrogen porosity, a control study was performed to compare welds on specimens that had been stainless steel wire-brushed prior to welding to those made on specimens that were not brushed prior to welding. In addition to wire brushing, a trailing shielding gas supply was used in this study to fully protect the trailing edge of the weld pool from atmospheric contamination during welding. This was believed to be important as it was observed that the weld pool could approach 20 to 30 mm in length when using welding speeds above 30 mm/s. Under these conditions, the length of the weld pool exceeds the 12 to 15 mm trailing shielding gas coverage provided by the standard GTAW and PAW gas nozzles used in this study. As a result, atmospheric oxygen and humidity could reach the weld pool and form a thin layer of refractory surface oxide on the molten weld pool surface before solidification is complete. This stable and solid oxide layer would prevent gas bubbles from breaking through the surface of the weld pool, trapping porosity near the surface of the weld. To address this concern, an additional 30 mm of trailing shielding gas supply was added to the existing welding torches using a shielding gas flow of 10 lpm for both torches.

Two welding conditions were used to compare the effects of stainless steel wire brushing: 3.0 kW at 30 mm/s and 3.0 kW at 50 mm/s. Six transverse cross sections were mounted for each weld condition and the area fractions of porosity in the fusion zone were measured. Representative cross sectional images are shown in Figure 4.38 and the porosity measurements are summarized in Table 4.3. The results showed a marked decrease in hydrogen porosity of 84 % and 77 % for welds produced at 30 and 50 mm/s, respectively. These results suggest that stainless steel wire brushing prior to welding is effective for controlling hydrogen porosity formation during welding; however, it should be noted that the presence of hydrogen porosity was not eliminated entirely by wire brushing. The small amounts of hydrogen porosity observed could have been caused by small oxide particles that were entrapped into the soft aluminum alloy during brushing [65], or from small amounts of hydrogen present in the base metal from prior processing [64]. The porosity content in stainless steel wire brushed specimens was not found to exceed the 0.1% limit specified by the CSA – W59.2 welded aluminum construction standard [84]. Due to the reduction in hydrogen porosity observed on wire brushed specimens, it was concluded that mechanical and forming properties of DSA welds should be evaluated on specimens that were wire brushed prior to welding.

Table 4.3: Comparison of average porosity area fraction for welds produced on specimens with and without stainless steel wire brushing using a total welding power of 3.0 kW.

Welding Speed	Surface Preparation	Average Porosity Area Fraction (%)
30 mm/s	Degreased	0.31 ± 0.15
30 mm/s	Degreased & SS Wire Brushed	0.05 ± 0.03
50 mm/s	Degreased	0.40 ± 0.07
50 mm/s	Degreased & SS Wire Brushed	0.09 ± 0.07
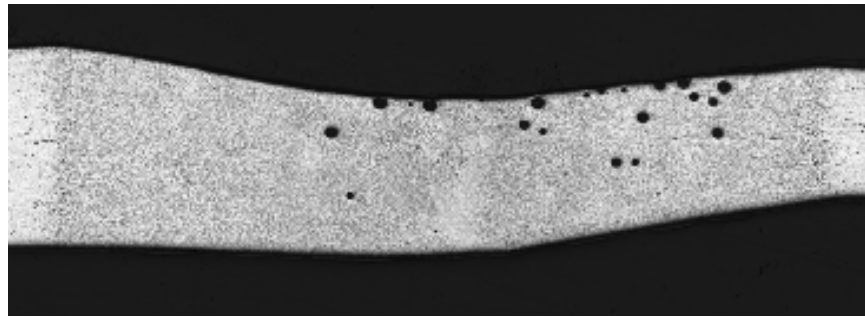
(a)
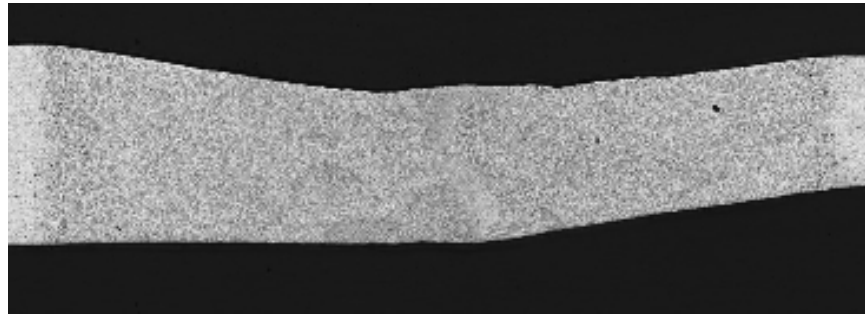
(b)
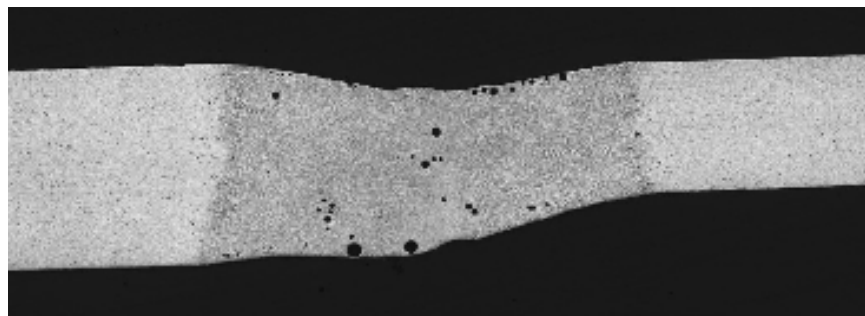
(c)
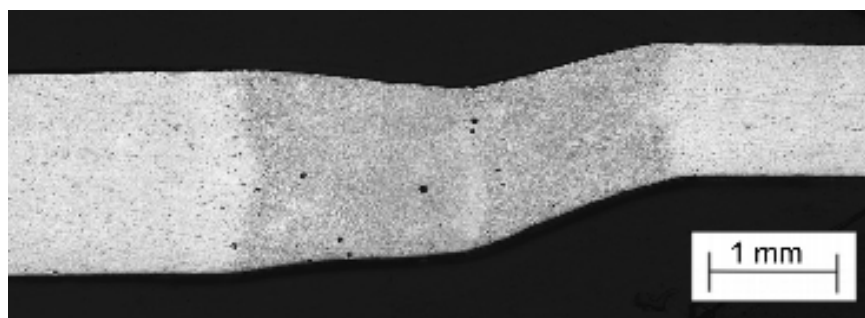
(d)

Figure 4.38: Hydrogen porosity in welds produced with a welding power of 3.0 kW at 30 mm/s for a) non-brushed specimen and b) stainless steel wire brushed specimen, and welds produced with a welding power of 3.0 kW at 50 mm/s for c) non-brushed specimen and d)stainless steel wire brushed specimen.

Further investigation of wire brushing was carried out to determine the effects of wire brushing on the range of suitable welding conditions identified earlier in Section 4.3.1. Visual weld quality was improved on specimens that had been stainless steel wire-brushed prior to welding. Top and bottom weld surfaces for welds produced at 2.6 kW total welding power are presented in Figure 4.39 and Figure 4.40. These welds were produced at identical welding speeds and powers to the welds shown earlier in Figure 4.16 and Figure 4.17. It can be seen that the stainless steel wire brushed specimens exhibit improved weld bead consistency compared to non-brushed specimens. No surface contamination or black spots are present along the weld centerline on the wire-brushed specimens.

The range of suitable welding conditions was also found to increase when stainless steel wire-brushing was used to remove the surface oxide from the work-pieces prior to welding. This can be seen by comparing the top surfaces of welds produced at 2.6 kW and 50 mm/s in Figure 4.16 and Figure 4.39, and the bottom weld surfaces shown in Figure 4.17 and Figure 4.40. Without wire brushing, the welds exhibit an inconsistent top and bottom weld bead, while the welds produced at the same welding conditions show very consistent weld beads when the specimens were wire brushed prior to welding.

Figure 4.41 shows the increase in welding speeds found to produce visually acceptable welds on wire brushed specimens. Wire brushing reduced the transition heat input between acceptable and inconsistent welds to approximately 50 J/mm compared to 60 J/mm for non-brushed specimens. This equates to a 20 % increase in travel speed for a given welding power. This observation is in agreement with modeling of DSAW conducted by Kwon and Weckman [31]. They reported that their model of conduction

124
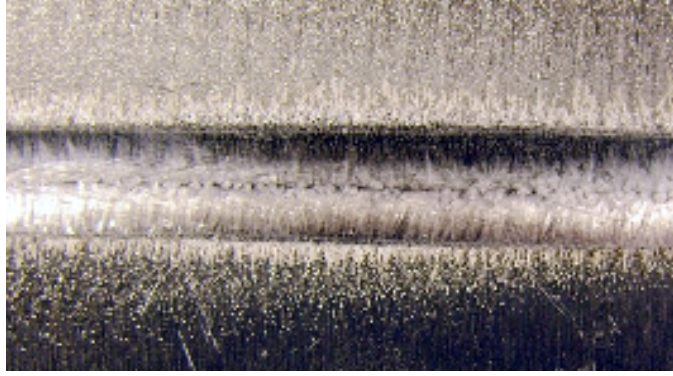
(a)
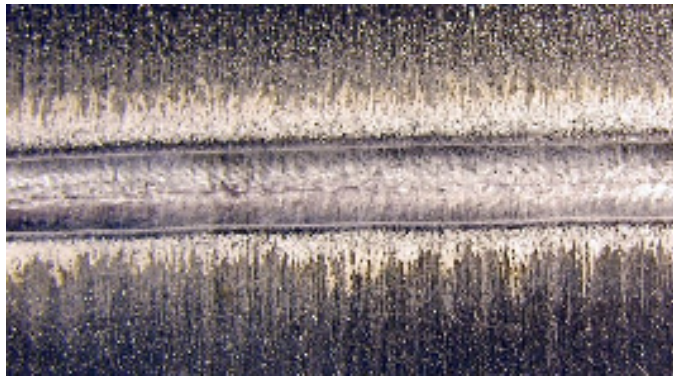
(b)
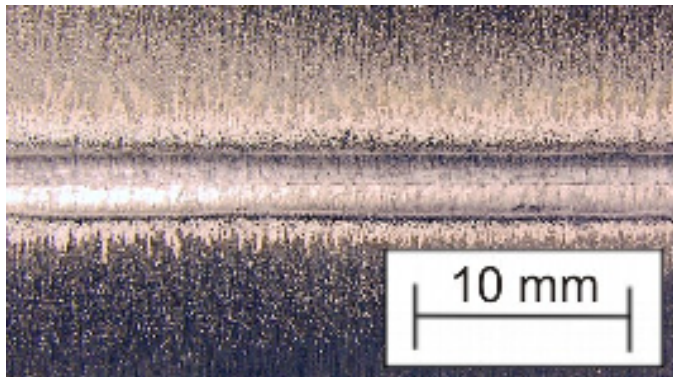
(c)

Figure 4.39: Top surfaces of welds produced on stainless steel wire brushed specimens made using a constant power of 2.6 kW and welding speeds: a) 30 mm/s, b) 40 mm/s, c) 50 mm/s.
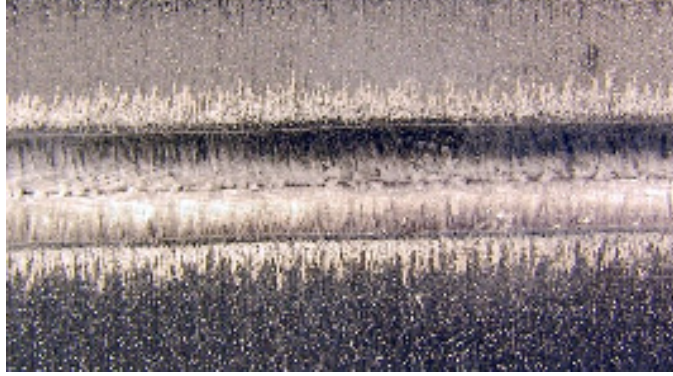
(a)
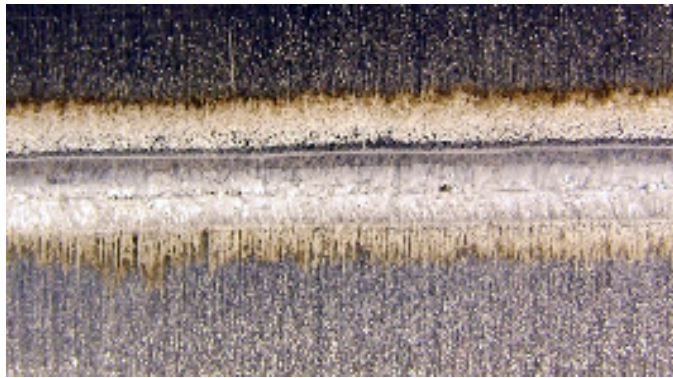
(b)
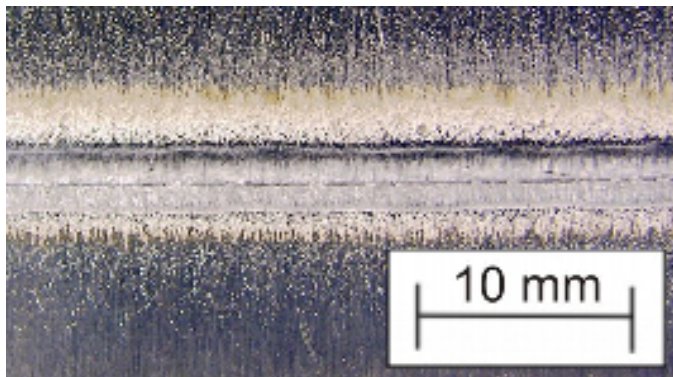
(c)

Figure 4.40:   Bottom surfaces of welds produced on stainless steel wire brushed specimens made using a constant power of 2.6 kW and welding speeds: a) 30 mm/s, b) 40 mm/s, c) 50 mm/s.
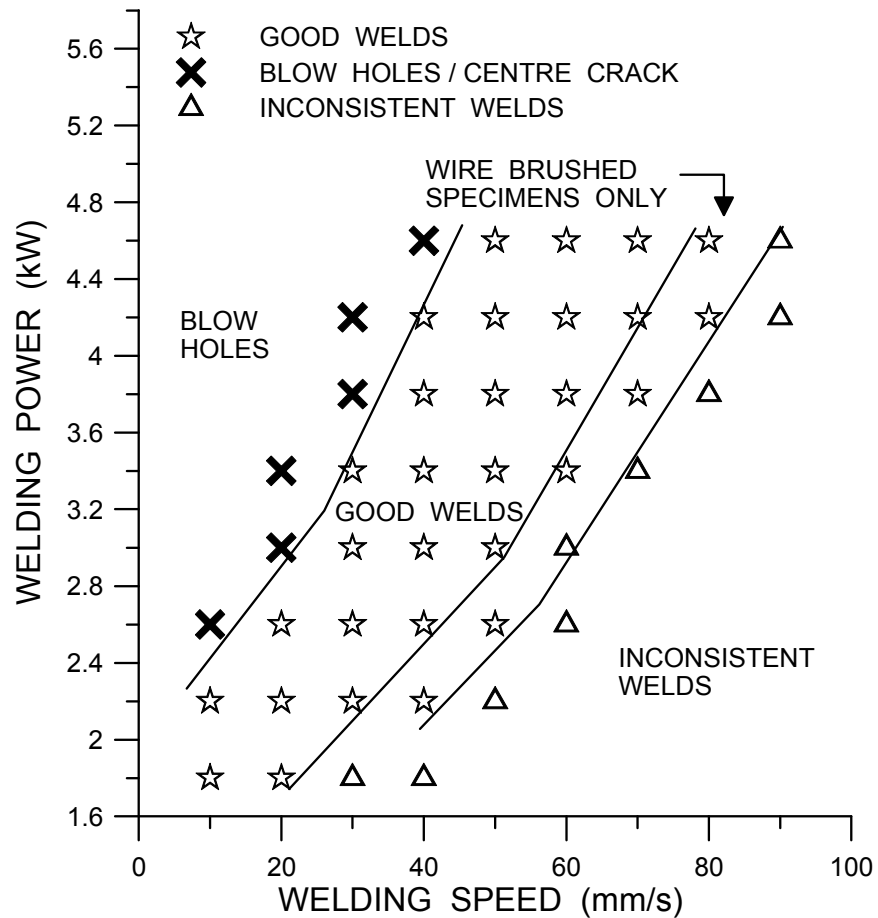
Figure 4.41: Range of welding conditions that produce visually acceptable welds on specimens that were stainless steel wire brushed prior to welding.

mode DSAW predicted that full penetration butt welds could be produced on 5182 aluminum alloy sheet at welding speeds that were found to produce inconsistent weld beads (on specimens that were not wire brushed). They proposed that the welding speed was limited by the ability of the arc to cathodically clean the surface oxide, rather than insufficient heat input to create a full penetration weld pool. Consequently, the increased consistency of the weld bead at high welding speeds observed in this study is believed to be a result of mechanically removing thickened oxide layers prior to welding. This

would reduce the amount of cathodic cleaning required to remove the surface oxide and maintain a stable weld pool when low heat input welding conditions are used.

4.5 Mechanical and Forming Properties of DSA Welds

The feasibility of using DSAW for TWB applications ultimately depends on the post weld forming properties of the welded specimen. Ideally, the forming limits should not be severely limited by the strength or ductility of the weld. The forming limits of TWBs have been shown to be lower than monolithic stamping blanks because the thinner sheet tends to undergo a greater amount of deformation than the thicker sheet, resulting in premature failure [71,72]. Previous studies on 5182 aluminum tailor welded blanks have shown that the formability can be further reduced if the weld is the cause of failure [71,72]. Therefore, it is of interest to identify the mechanical and forming properties of optimized welds produced with DSAW. All specimens were stainless steel wire brushed prior to welding to limit the formation of hydrogen porosity and trailing shielding gas coverage was also used to fully protect the weld pool from contamination until solidification was complete. Comparisons were made between welds produced with a welding power of 2.6 and 4.2 kW over a range of welding speeds from 30 to 80 mm/s. Further welds were produced with powers of 1.3, 1.8 and 2.2 kW at speeds of 15, 20, and 25 mm/s, respectively.

The mechanical and forming properties of 1.0 to 1.5 mm thick 5182 aluminum alloy TWBs produced with DSAW were evaluated using the following tests: transverse tensile tests to determine the joint efficiency, longitudinal tensile tests to identify the yield strength, ultimate tensile strength and ductility of the weld metal and limiting dome

height tests to compare the relative formability of TWB specimens compared to the base metal formability.

4.5.1 Tensile and Formability Testing

Welds produced using total welding powers of 2.6 and 4.2 kW were chosen as a basis for tensile and formability testing as these conditions would allow direct comparisons to be made between the tensile test results presented in Section 4.3 for specimens that were not stainless steel wire brushed prior to welding. Load versus displacement curves obtained from transverse tensile tests of welds produced with welding powers of 2.6 kW and 4.2 kW are shown in Figure 4.43 and Figure 4.44, respectively. These results are similar to those presented earlier in Figure 4.29 and Figure 4.30 for weld specimens that were not stainless steel wire brushed prior to welding. Qualitative comparisons of the displacement at failure suggest that the ductility decreased as the welding speed was increased for a constant power of 2.6 kW. A similar trend of decreasing ductility with increasing welding speed is also observed with a welding power of 4.2 kW. Figure 4.42 shows the typical failure of a transverse tensile specimen. In all cases, specimen failure observed to occur near the weld centerline.

Figure 4.42: Typical transverse tensile specimen failure.
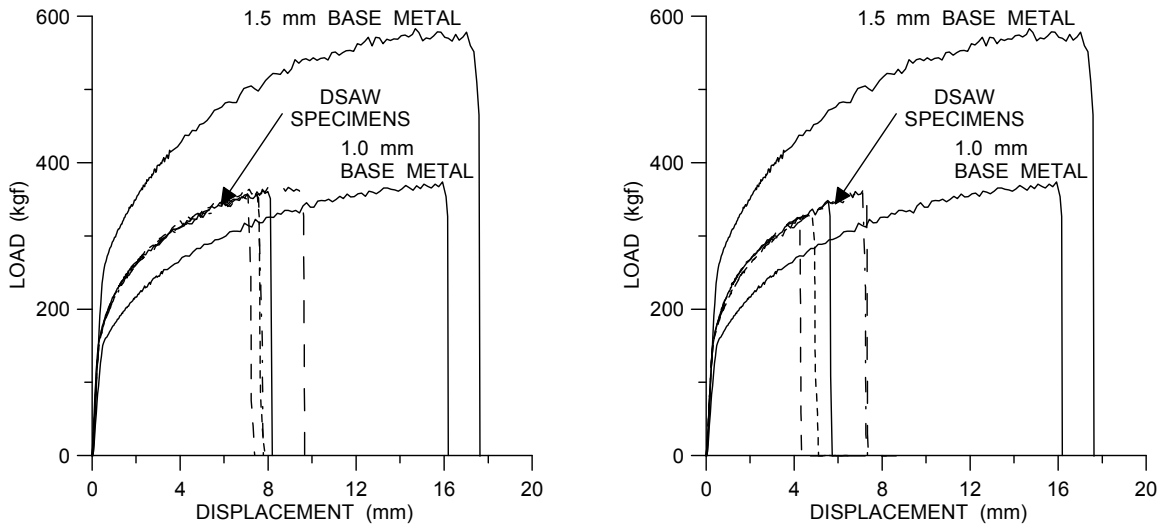
(a)   (b)
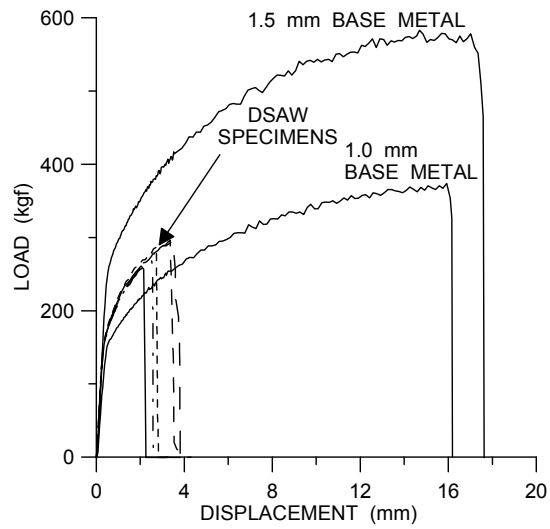
(c)

Figure 4.43: Load displacement curves for welds produced with a total welding power of 2.6 kW on stainless steel wire brushed specimens at welding speeds of a) 30 mm/s, b) 40 mm/s, c) 50 mm/s.

130
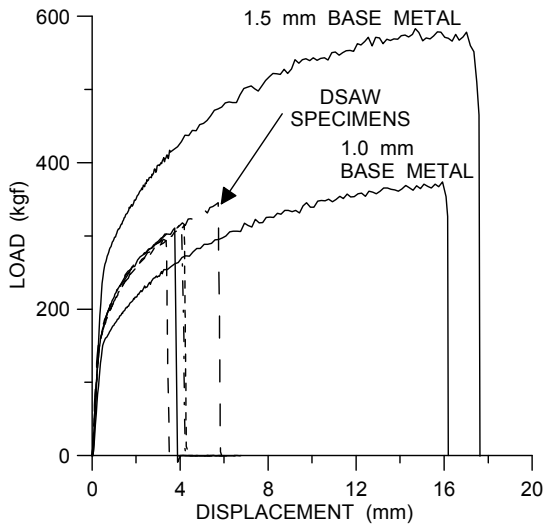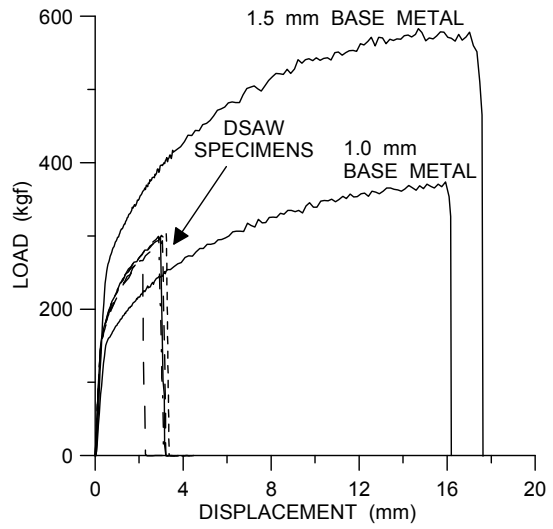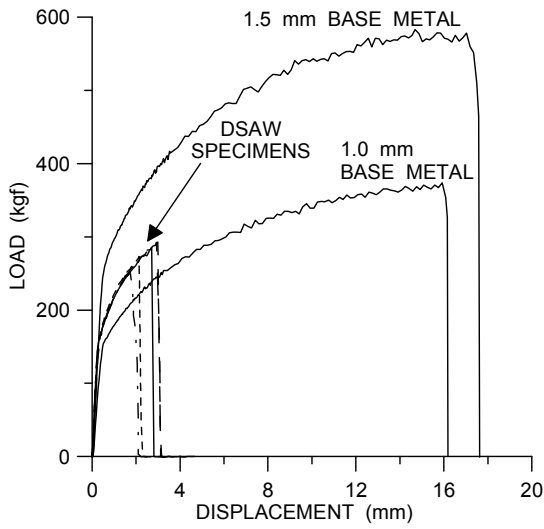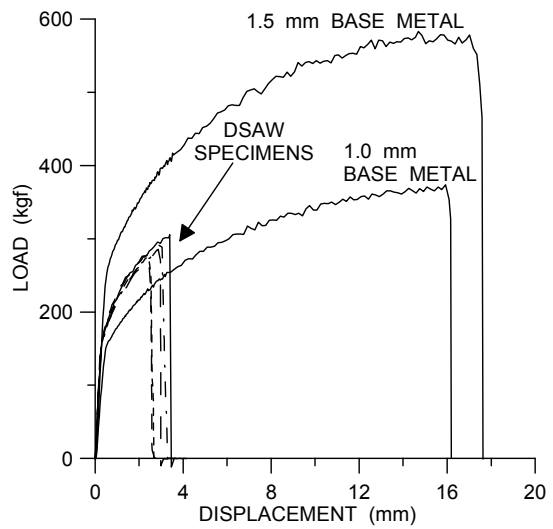
Figure 4.44: Load displacement curves for welds produced with a total welding power of 4.2 kW on stainless steel wire brushed specimens at welding speeds of a) 50 mm/s, b) 60 mm/s, c) 70 mm/s, and d) 80 mm/s.

The joint efficiencies for the transverse tensile tests obtained for wire brushed specimens have been compared to earlier results on non-brushed specimens in Figure 4.45. A peak joint efficiency of 96% was observed for the weld produced at 2.6 kW and 30 mm/s. Increases in the welding speed tended to reduce the joint efficiency up to a welding speed of 60 mm/s. Beyond 60 mm/s, the joint efficiency was consistently observed to fall between 75 and 80%. The results for 2.6 kW were similar to those observed for specimens that were not wire brushed prior to welding with the exception of the weld produced at 50 mm/s which produced a slightly lower joint efficiency for the wire brushed specimen. The joint efficiency for the weld produced at 4.2 kW and 50 mm/s was similar for both the brushed and the non-brushed specimens while welding speeds greater than and equal to 60 mm/s produced slightly higher joint efficiencies for the wire brushed specimens

The tensile strength of welded aluminum alloys has been reported to be tolerant of 1 to 2 volume percent porosity without having a noticeable effect on the strength [57]. For this reason, the similarity in strength observed between wire brushed specimens and non-brushed specimens is not unexpected because the hydrogen porosity volumes were not found to exceed 1% porosity by volume. It should also be mentioned that other researchers have reported that the tensile strength of welded aluminum alloys is proportional to the loss in cross sectional area of the weld caused by porosity [58,59]. In this case, a slight improvement in strength would be expected from the reduction in porosity; however, the improvement in strength would not be expected to exceed 1% based on the maximum porosity levels observed in non-brushed specimens.
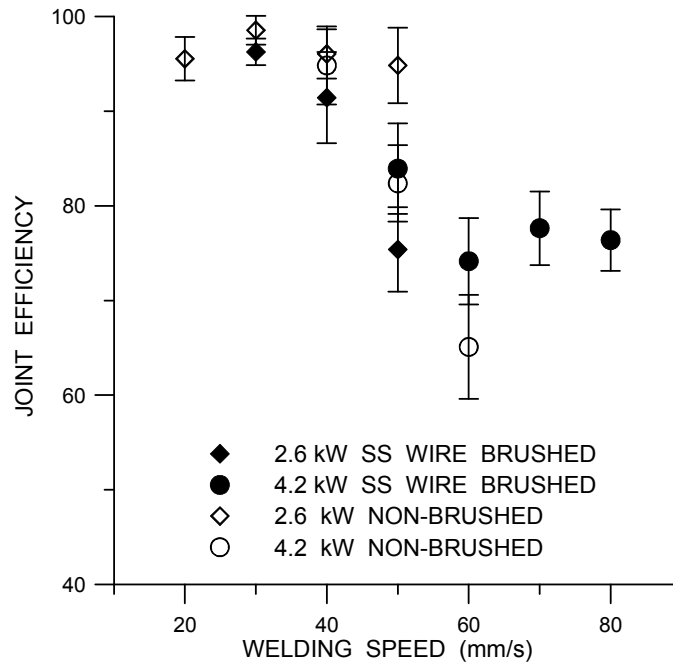
Figure 4.45: Joint efficiency for stainless steel wire brushed specimens and welded using total welding powers of 2.6 kW and 4.2 kW.

Consequently, the improvement in strength would not be evident with the 2 to 5% variance in measurements from tensile testing of the welded specimens.

Longitudinal tensile tests were performed using sub-size tensile specimens that were specially machined so that the gage length of the specimen was comprised solely of weld metal. The specimens were machined with a 30 mm gage length which permitted the use of a 25.4 mm (1 inch) extensometer allowing accurate strain measurements to be obtained. This allowed stress-strain curves to be obtained allowing quantitative comparisons to be drawn between different welding conditions as well as comparing weld metal properties to those of the base metal. Table 4.4 presents the tensile properties obtained for base metal specimens and welded specimens produced with welding powers of 2.6 and 4.2 kW at various welding speeds.

Table 4.4: Longitudinal tensile results for total welding powers of 2.6 and 4.2 kW.

Welding Condition	$\sigma_{Y0.2}$ (MPa)	UTS (MPa)	% Elongation
2.6 kW, 30 mm/s	127.7 ± 5.5	224.2 ± 6.2	13.0 ± 1.8
2.6 kW, 40 mm/s	143.2 ± 4.1	236.9 ± 18.0	10.5 ± 2.6
4.2 kW, 50 mm/s	148.8 ± 6.6	216.2 ± 7.3	8.6 ± 0.8
4.2 kW, 60 mm/s	136.4 ± 6.7	206.3 ± 4.4	10.2 ± 1.3
4.2 kW, 70 mm/s	128.6 ± 5.1	188.2 ± 9.0	6.8 ± 1.4
Base Metal	125.7 ± 2.5	288.6 ± 0.8	22.5 ± 1.4

Figure 4.46 and Figure 4.47 show the median (of five repetitions) stress-strain plots for welds produced with a total welding power of 2.6 kW and 4.2 kW, respectively. The yield stress is observed to be similar to the base metal for all the welding conditions tested, while the weld metal strain at failure and the ultimate strength were found to be less than half of the base metal values. The strain at failure (elongation) showed a decreasing trend with increased welding speed for both welding powers of 2.6 kW and 4.2 kW. The elongation values ranged between 6.8% and 13% for the welded specimens compared to 22% for the base metal. These results are comparable to those obtained from laser beam welding of 5182-O aluminum alloys [74]. Davies *et al.* [69] also reported similar elongation measurements for GTA welded 5182 aluminum alloys specimens; however, they also reported that they were able to attain elongation values between 16% and 21% for welds produced with a welding procedure that significantly reduced the number of internal voids in the weld metal.

The ultimate tensile strength of the weld metal was also found to decrease as the welding speed was increased in a similar trend to the joint efficiencies obtained from the transverse tensile tests. Longitudinal tensile tests were not performed on welds produced
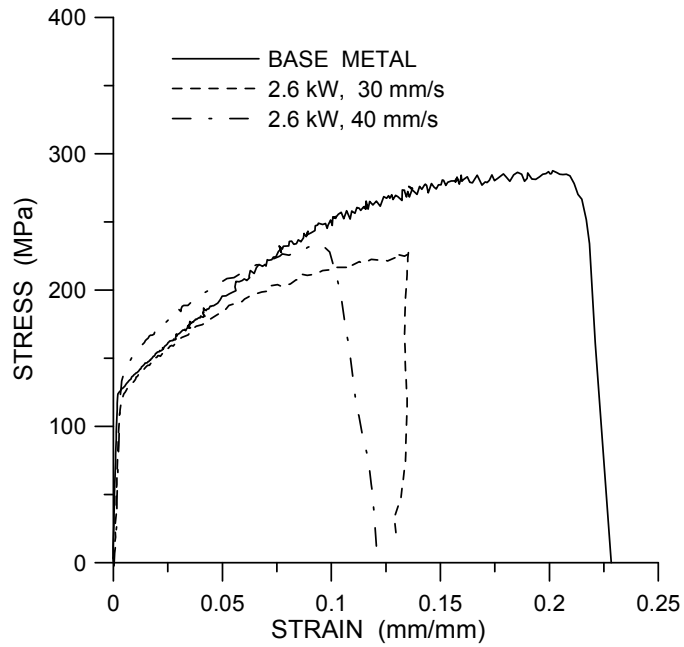
Figure 4.46: Stress strain curves obtained from longitudinal tensile tests on the weld for specimens produced with a total welding power of 2.6 kW.
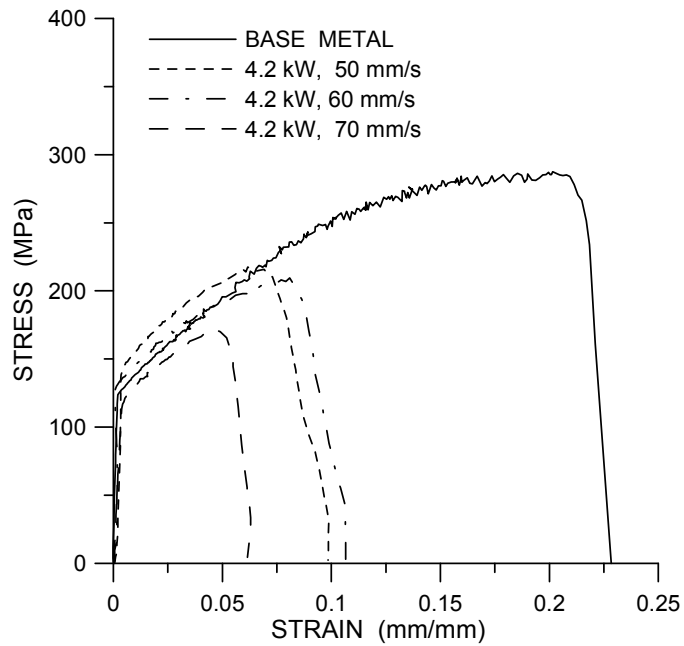
Figure 4.47: Stress strain curves obtained from longitudinal tensile tests on the weld for specimens produced with a total welding power of 4.2 kW.

with 2.6 kW welding power at 50 mm/s and 4.2 kW welding power at 80 mm/s because the weld width was too narrow to machine a consistent tensile specimen with a 30 mm gage length suitable for an extensometer to be attached during testing.

Formability testing was carried out using a limiting dome height test fixture on welds produced using a welding power of 2.6 kW at speeds of 30, 40 and 50 mm/s. These welding conditions were selected as they were found to produce the best joint efficiencies and the highest ductility of the welding conditions tested above. The formability results are presented in Table 4.5. The base metal forming limits were very similar for the two sheet thicknesses used in this study. The thicker sheet had a slightly higher punch height at failure so all welded specimens were compared to the thinner 1.0 mm thick sheet to determine the percentage of base metal formability that was retained by the TWB specimen. The TWB welded specimens were found to have significantly reduced formability compared to the base metal. This can be seen in Figure 4.48 which compares the limiting dome height specimens for the base metal with a specimen welded with a welding power of 2.6 kW at a speed of 30 mm/s. These specimens failed at a punch height of 27.4 mm and 14.3 mm, respectively. The best result observed for the welded specimens was found to be 52.3% of the parent metal for a weld produced at 40 mm/s; however, it should be noted that the variance of the forming results for welds produced at 40 and 50 mm/s showed a substantial increase compared to the weld at 30 mm/s. For this reason, the welding speed of 30 mm/s was thought to produce the best forming results as the average punch height at failure was very close to the average obtained for a welding speed of 40 mm/s. In all cases, the welded specimens had a greater variance than the base metal specimens.

Table 4.5: Limiting dome height test results for 1.0 to 1.5 mm thick 5182 aluminum alloy tailor welded blanks welded with a total power of 2.6 kW.

Test Condition / Welding Speed	Punch Height at Failure (mm)	Percent of 1.0 mm Base Metal Formability
1.5 mm Base Metal	28.0 ± 0.29	-
1.0 mm Base Metal	27.4 ± 0.33	-
2.6 kW, 30 mm/s	14.3 ± 0.66	51.9
2.6 kW, 40 mm/s	14.4 ± 2.41	52.3
2.6 kW, 50 mm/s	10.6 ± 1.93	38.4

27.4 mm   14.3 mm
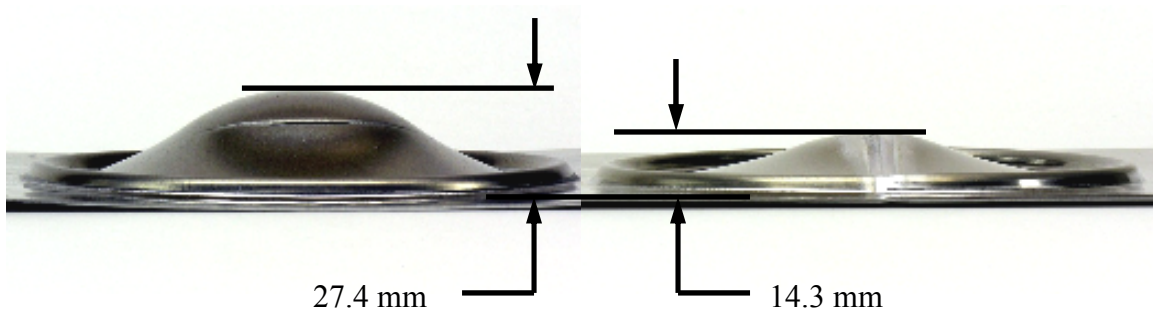
Figure 4.48: Base metal limiting dome height specimen (1.0 mm thick) with a punch failure height of 27.4 mm (left) compared with a 1.0 to 1.5 mm thick TWB specimen welded with a power of 2.6 kW at 30 mm/s showing a failure height of 14.3 mm (right).

The weld was found to be the failure location during forming for all of the specimens tested. Typical failures for the base metal specimens and the welded specimens are shown in Figure 4.49. The base metal specimens were observed to start necking in a uniform ring around the centre of the specimen at the point where the specimen was no longer in contact with the hemispherical punch. Fracture was observed to initiate in the necked region and quickly propagated around the necked ring as shown in Figure 4.49a. The welded specimens were not observed to produce any necking in the

(a)

1.5 mm Sheet

1.0 mm Sheet
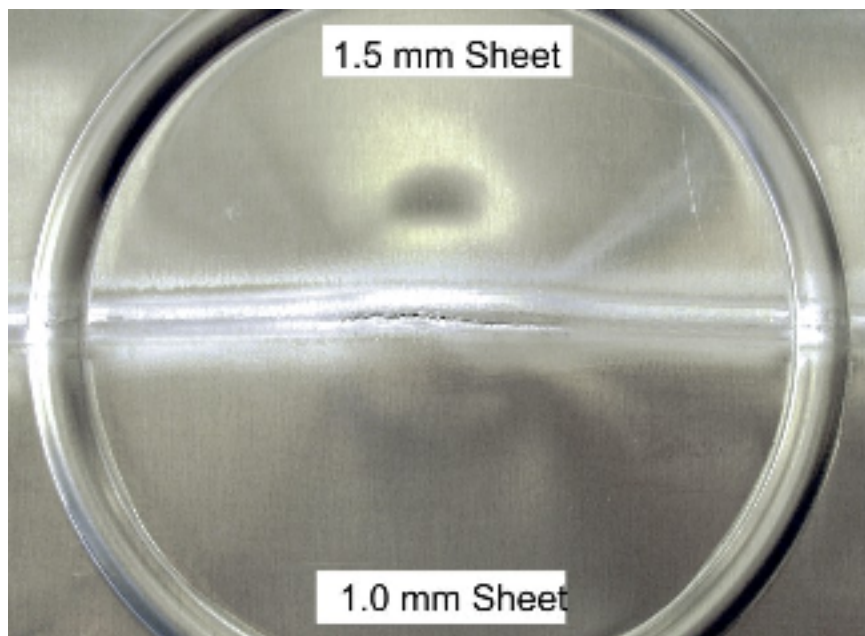
(b)

Figure 4.49: Typical failures observed for limiting dome height tests for a) base metal specimens and b) TWB specimens welded with a power of 2.6 kW at 30, 40 and 50 mm/s.

base metal. The failure was observed to occur along the weld centerline, forming a crack that propagated along the length of the weld as shown in Figure 4.49b. The formability limits of the welded specimens in this study are comparable to those found by Shakeri *et al.* [71] and Buste *et al.* [72] on 5754 aluminum alloy TWBs. They reported that the formability was limited to 45 to 55 % when the weld was the location of failure; however, formability was reported to exceed 80 % of the base metal formability when the failure occurred in the thin base metal sheet. This suggests that the forming limits observed in this study could be greatly improved if the failure location can be moved from the weld to the base metal. For this reason, the fracture mechanism and metallographic properties were examined in detail to look for evidence that would explain why the weld was limiting the formability of the TWB specimens.

4.5.2 SEM and Metallographic Analysis

Fracture surfaces from transverse tensile tests were examined using a SEM to allow the failure mode to be identified for the different welding conditions. The fracture surface for the weld produced with a welding power of 2.6 kW at a speed of 30 mm/s is shown in Figure 4.50. A classic ductile fracture surface was observed across the entire specimen. The ductile fracture surface observed is consistent with the tensile data that showed that this welding condition produced the greatest joint efficiency and had the highest ductility of all the welds tested. None of the other welding conditions produced the same entirely ductile fracture surface that was observed for this specimen.

Fractures surfaces for specimens that were produced with welding speeds greater than 30 mm/s contained a mixture of ductile fracture surfaces and dendritic regions. A

139
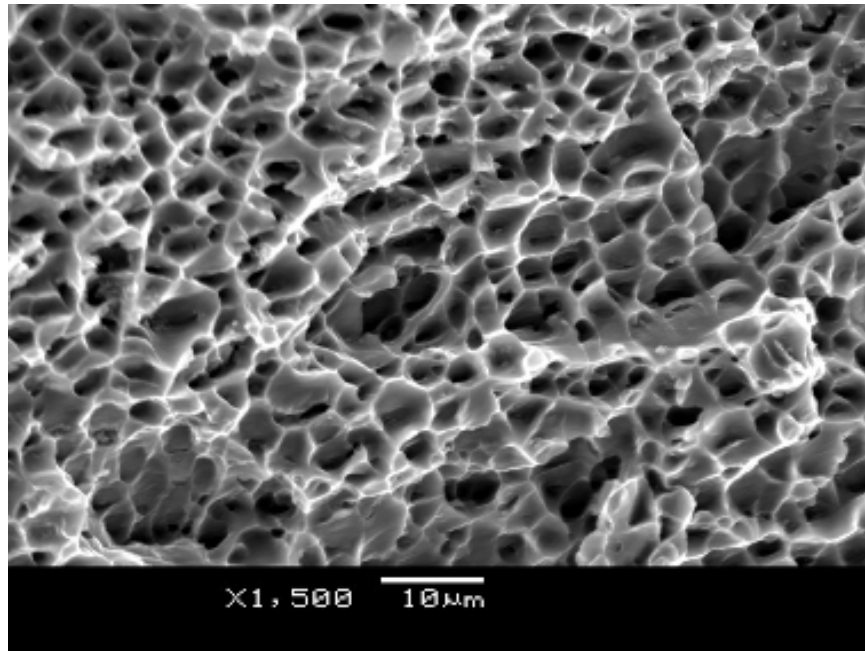
Figure 4.50: Ductile fracture surface produced during transverse tensile testing of a weld produced with a total welding power of 2.6kW at a speed of 30 mm/s.

representative example is shown in Figure 4.51 of a weld produced with a welding power of 4.2 kW and a welding speed of 60 mm/s. At low magnification, the fracture surface could be mistaken for a completely ductile failure; however, higher magnification reveals that a mixture of dendrites and ductile surfaces are present.   The dendritic regions observed along the fracture surface suggest that the weld likely contained solidification shrinkage micro-porosity along the weld centerline where the specimen failed in tension. This finding also provides an explanation for the decrease in strength and ductility that was observed for welds produced with increasing welding speed.

To verify the presence of solidification micro-porosity within the weld, transverse cross-sections were analyzed using an optical microscope.   The irregular shape of
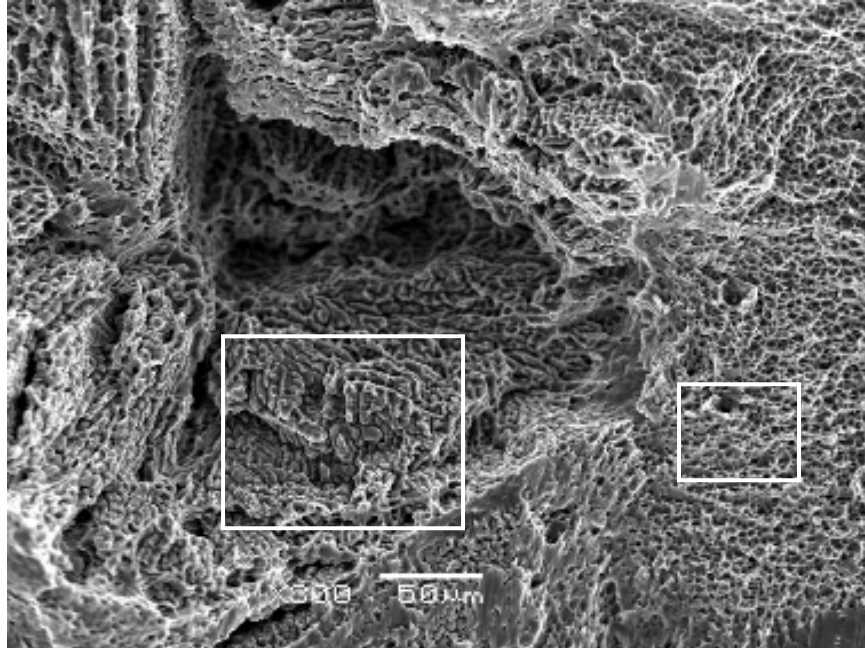
(a)
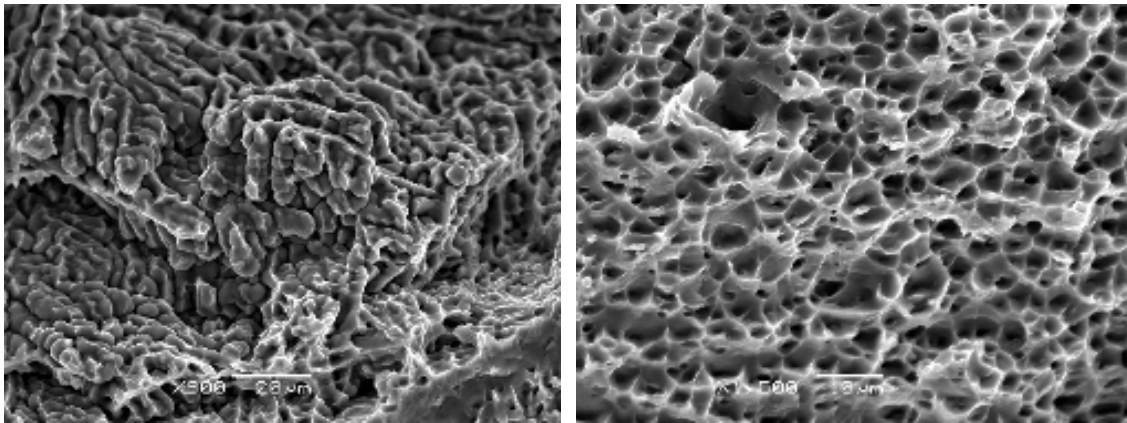
(b)   (c)

Figure 4.51: Fracture surface of a weld produced with a welding power of 4.2 kW and a travel speed of 60 mm/s showing a) a mixture of dendrites (left) and ductile fracture surface (right) and higher magnification images of b) dendrites and c) ductile fracture surface.

solidification shrinkage pores can be distinguished from gas pores that have smooth round shapes caused by the surface tension between the molten weld pool and a gas bubble [85]. Solidification shrinkage micro-porosity also tends to be observed in clusters instead of the randomly spaced and often isolated gas pores [85].

All of the welds were found to contain solidification micro-porosity to varying degrees. Figure 4.52 shows a weld produced with a welding power of 2.6 kW and welding speed of 30 mm/s. The low magnification image shown in Figure 4.52a shows that the weld does not appear to contain any solidification shrinkage micro-porosity defects; however, at higher magnification small clusters of micro-porosity are evident, as can be seen in Figure 4.52b. The quantity of solidification micro-porosity was found to increase as the welding speed was increased as can be seen in Figure 4.53. In these specimens, the solidification micro-porosity is evident without the use of higher magnification due to the increase in the number of pores. The pores are also observed to be clustered near the weld centerline which coincides with the failure location in transverse tensile tests and limiting dome height tests.

The presence of solidification porosity explains why the ductility and the ultimate tensile strength of the weld were found to be lower than the base metal for all of the welding conditions tested. The small solidification shrinkage pores would have produced localized stress concentrations during tensile loading, localizing the strains around the pores causing premature failure. The further decreases in ductility observed as the welding speed was increased are explained by the increased volume of solidification shrinkage porosity that was observed for these specimens. Li *et al.* [86] found that
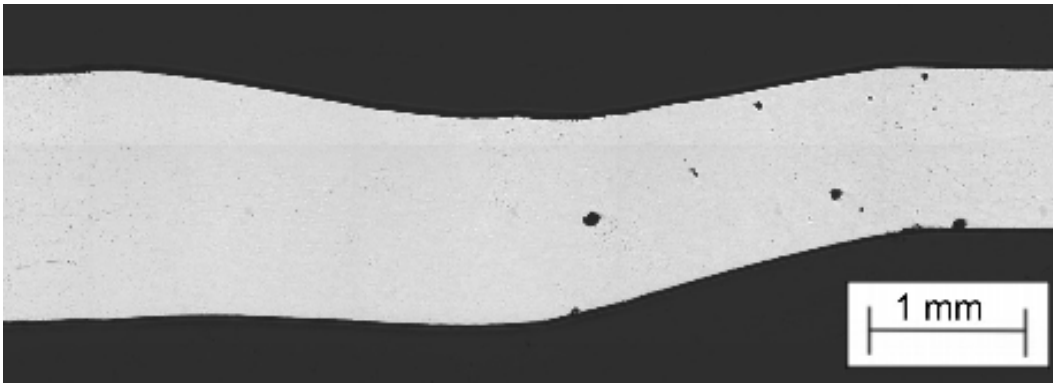
(a)
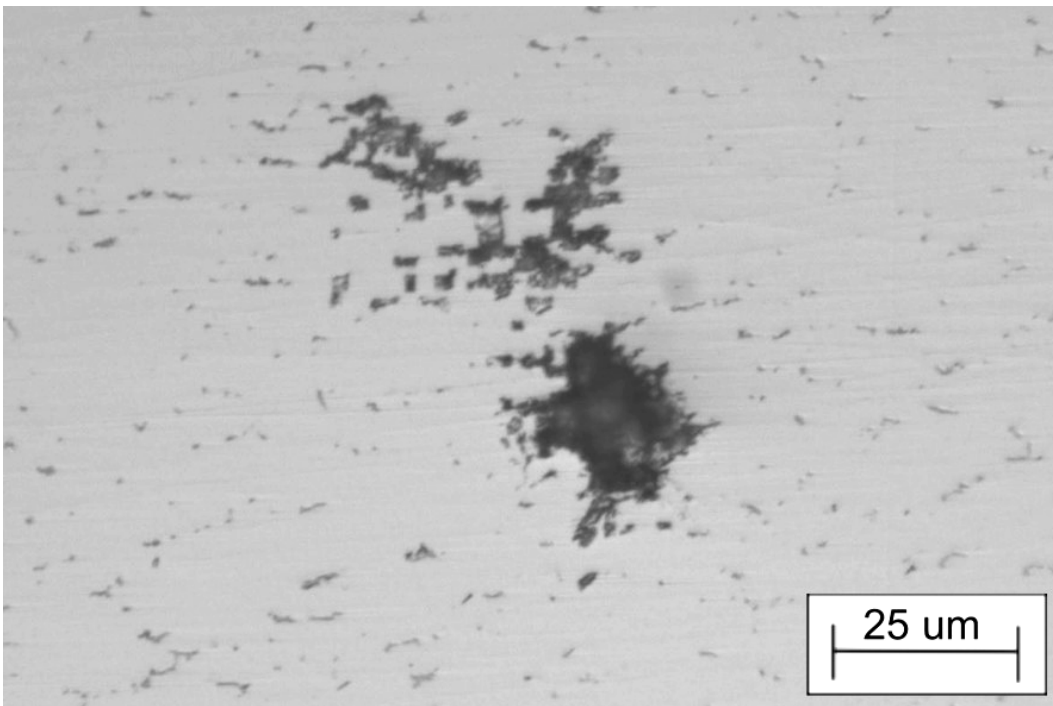
(b)

Figure 4.52: Transverse cross-section of a weld produced with a welding power of 2.6 kW and a travel speed of 30 mm/s showing a) low magnification view of the weld fusion zone and b) higher magnification image revealing solidification shrinkage micro-porosity.
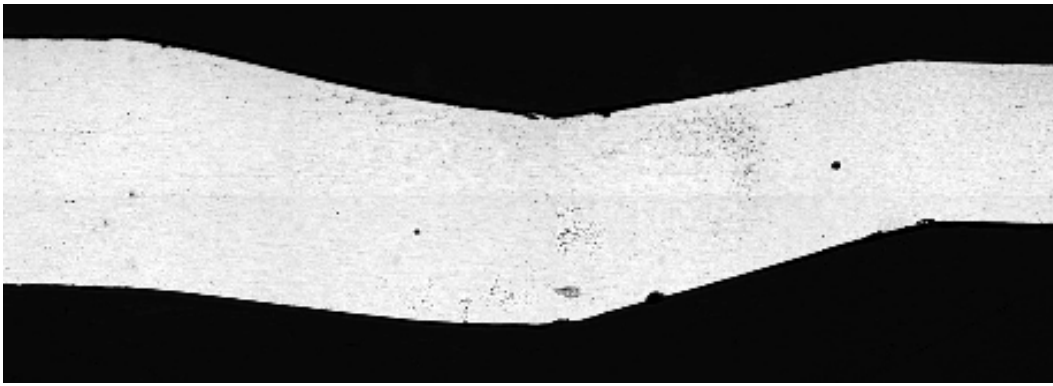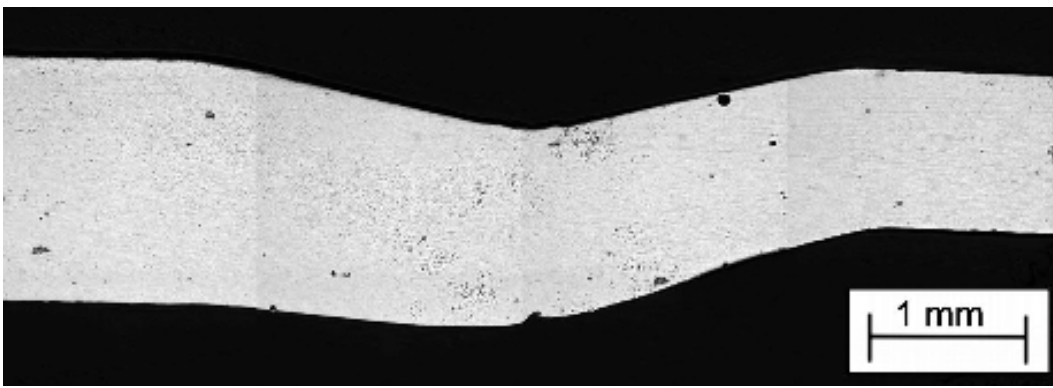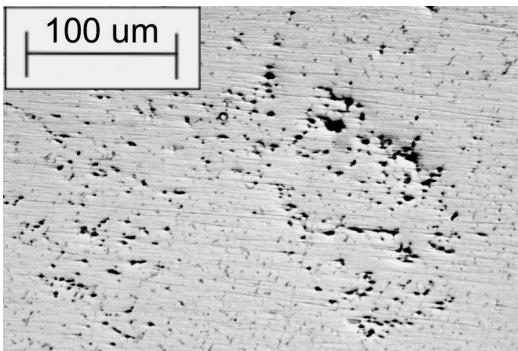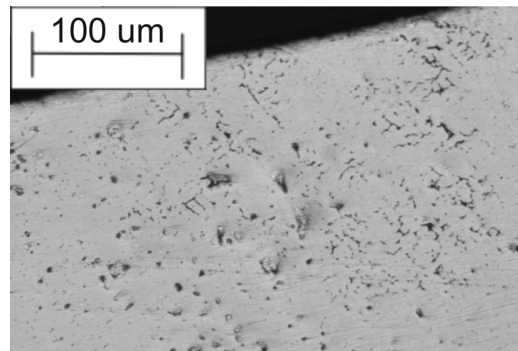
Figure 4.53: Significant solidification shrinkage micro-porosity is observed in welds produced with a welding power of 4.2 kW at travel speeds of a) and c) 50 mm/s, and b) and d) 60 mm/s.

fatigue life was also reduced by the presence of solidification shrinkage micro-porosity in their study on repair welding of aluminum castings.

Solidification shrinkage micro-porosity is a problem that has been encountered in metal casting and is caused primarily by limited flow of molten metal to fill voids created by the volume contraction that occurs during the liquid-to-solid phase transformation pf long freezing range alloys [87]. Alloys with large solidification temperature ranges are even more susceptible to micro-porosity due to the formation of a mushy zone caused by the nucleation and growth of equiaxed dendritic grains during solidification. Dendrite arms on the equiaxed grains tend to have very fine spacing which will choke the flow of fluid to the dendrite roots and the tail end of the weld, preventing interdendritic and intergranular voids from being filled at the final stages of solidification.

The fusion zone for welds in this study were comprised of columnar grains extending from the fusion boundary to a region of equiaxed grains in the centre of the weld. This is shown for welds produced with a welding power of 2.6 kW at 30 mm/s and 4.2 kW at 60 mm/s in Figure 4.54. The location of the equiaxed grains in the micrographs is seen to correspond to the location of the micro-porosity observed in the welds. This further supports that the micro-porosity observed in this study is caused by solidification shrinkage.

To help understand the increase in solidification shrinkage micro-porosity at higher welding speeds, the length of the weld pool was considered for different welding conditions for two reasons. First, increasing the length relative to the width of the weld pool would be expected to promote the formation of a longer mushy zone at the tail of the weld pool during solidification. This would increase the distance that molten metal must
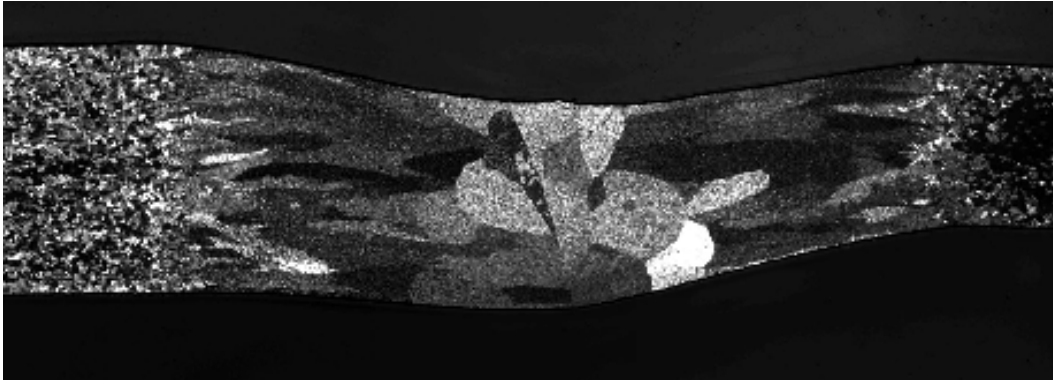
(a)
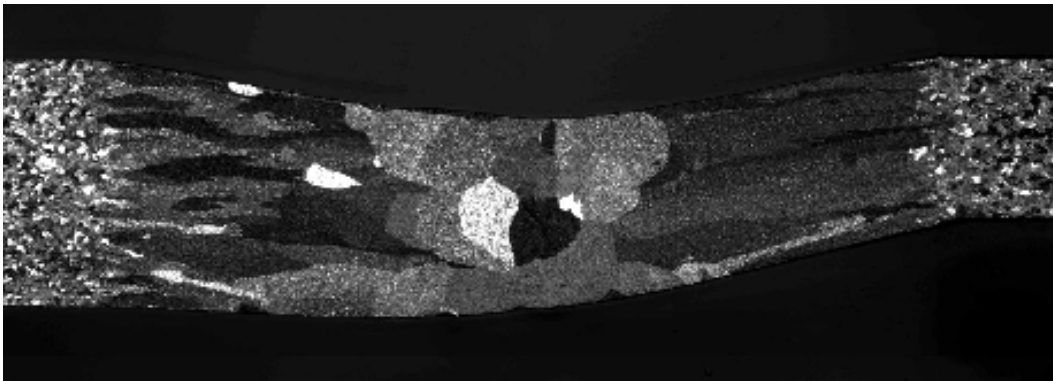
(b)
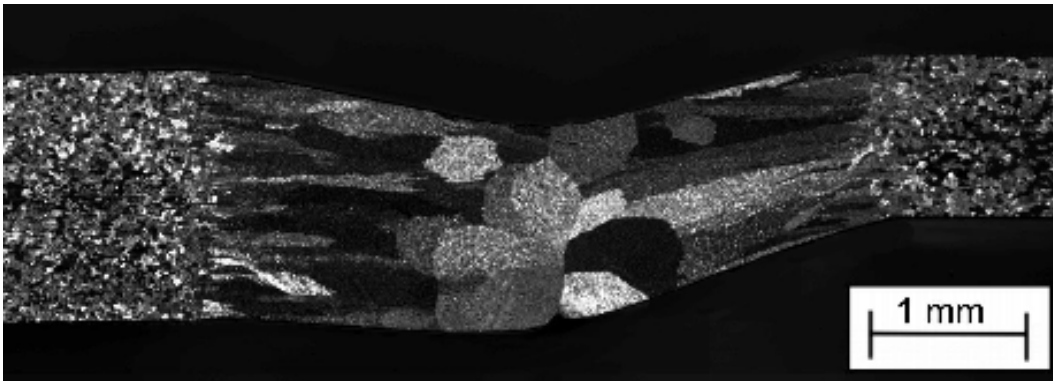
(c)

Figure 4.54: Weld Macrostructure showing columnar grains extending from the fusion boundary and equiaxed grains growing from the weld center in welds produced with a) 2.6 kW and 30 mm/s, b) 4.2 kW and 50 mm/s, and c) 4.2 kW and 60 mm/s.

travel through small inter-dendrite channels to fill solidification shrinkage voids and consequently would be expected to increase the quantity of micro-porosity in the solidified structure [87]. Second, at high welding speeds, the solidification process will not be described by equilibrium cooling conditions. Instead, the Scheil non-equilibrium cooling conditions where solute diffusion into the solid is considered negligible [9,87] is more appropriate. Under these cooling conditions, it is expected that solute will be rejected from newly formed solid causing an increase in the solute concentration of the remaining liquid. This will push the composition of the remaining liquid towards the eutectic composition and depress the solidus temperature. ThermoCalc® simulations performed by Dr. Simon Barker [88] show that under non-equilibrium, Scheil-type cooling conditions, the freezing point (solidus temperature) can be depressed from 586°C to 445°C. With an equilibrium liquidus temperature of 633°C this equates to an increase in the freezing range from 47°C under equilibrium cooling to 188°C under non-equilibrium cooling conditions. This extension of the freezing temperature range would be expected to have a significant impact on the length of the mushy zone during solidification of the weld.

The relative length of the weld pool for all the weld conditions used in this study was estimated by measuring the aspect ratio of the weld pool. This was achieved by measuring the length of the weld crater at the end of the top (PAW) weld surface, shown in Figure 4.55, and dividing it by the width of the weld. The weld crater was used to identify the length of the weld pool because it should be representative of the length of the steady state weld pool. The weld pool crater measurements and respective aspect ratios (length/width) are shown in Table 4.6 for the welding conditions examined in this

147

Figure 4.55: Weld pool crater at the end of the PAW side of specimen showing the length and width measurements used to determine the aspect ratio of the weld pool.

Table 4.6: Weld pool crater measurements and aspect ratios (length/width) of welds produced with welding powers of 2.6 kW and 4.2 kW at various welding speeds.

Welding Condition	Weld Width (mm)	Weld Pool Length (mm)	Aspect Ratio
2.6 kW, 30 mm/s	5.1	19.8	3.9
2.6 kW, 40 mm/s	3.7	13.6	3.7
2.6 kW, 50 mm/s	2.8	12.8	4.6
4.2 kW, 50 mm/s	5.6	31.8	5.7
4.2 kW, 60 mm/s	4.5	27.4	6.1
4.2 kW, 70 mm/s	3.9	22.3	5.8
4.2 kW, 80 mm/s	3.4	19.4	5.7

study. It was found that the welding speeds of 30 and 40 mm/s produced smaller aspect ratios than welds produced at speeds greater than 50 mm/s.

Further evidence that the relative length of the weld pool and mushy zone influences the final weld properties was found when the transverse tensile strength (joint efficiency), the ultimate tensile strength, the weld metal ductility, and the formability

148

results obtained in this study were plotted as a function of the weld pool aspect ratio. These results are presented in

Figure 4.56. Here is it clear that the material properties tend to improve as the weld aspect ratio decreases (the length of the weld pool is decreased relative to its width). The improvement in mechanical properties also correlates well with the relative amount of solidification shrinkage micro-porosity observed in transverse cross sections.

Extrapolating the trend of improving mechanical properties and the decrease in solidification shrinkage micro-porosity observed as the weld pool aspect ratio decreases suggests that the mechanical properties could be improved further and the solidification shrinkage porosity could be decreased or even eliminated in welds produced with aspect ratios below 3.7. This is supported by the current understanding of solidification micro-porosity formation; decreasing the weld pool aspect ratio would decrease the length of the mushy zone during solidification, improving fluid flow to the tail end of the weld, hence, minimizing the chances of voids forming as the weld metal contracts during solidification. Therefore, it was of interest to determine the mechanical and forming properties of DSA welds with low weld pool aspect ratios.

4.5.3 Low Aspect Ratio Welds

Examination of the welds produced in Section 4.3.1 and Section 4.4 (welds used to identify the range of suitable welding speeds and powers for joining 1.0 to 1.5 mm thick 5182 aluminum sheet) revealed that the aspect ratio of the weld pool generally decreased as the welding speed was decreased for a given welding power. Further
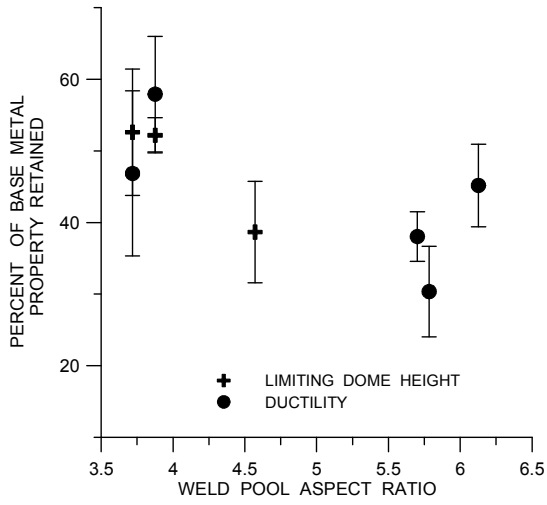
(a)
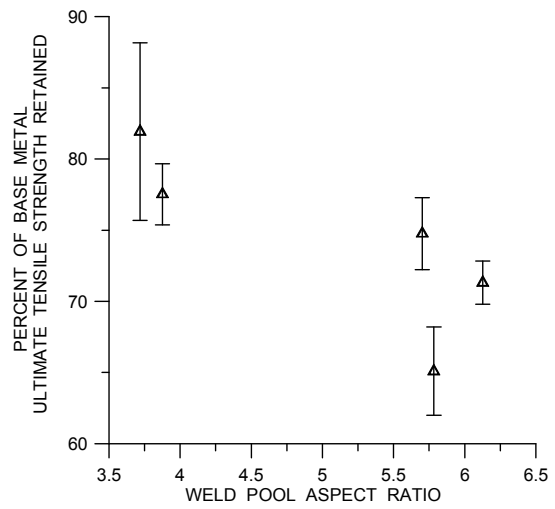
(b)
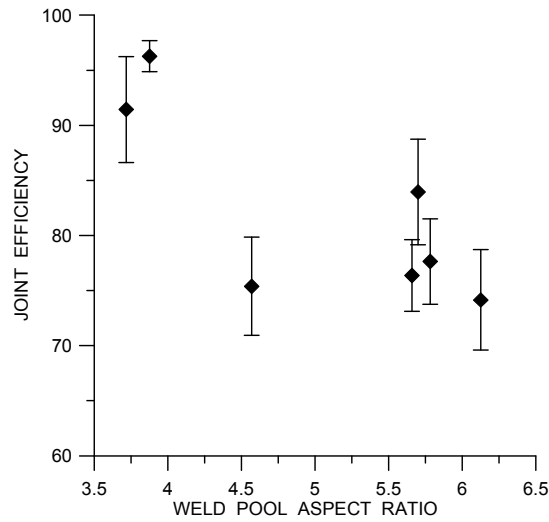
(c)

Figure 4.56: Mechanical and forming properties of welded specimens versus the weld pool aspect ratio including: a) limiting dome height and weld metal ductility, b) ultimate tensile strength and c) transverse joint efficiency.

decreases in the weld pool aspect ratio were observed as both the welding speed and welding power were decreased. Aspect ratios below 3.7 were not observed for welding powers of 2.6 and 4.2 kW (blowholes were observed before the aspect ratio fell below 3.7). Therefore, it was necessary to use welding powers below 2.6 kW to attain welds with aspect ratios below 3.7. The welding conditions used to produce low aspect ratio welds were 2.2 kW at 25 mm/s, 1.8 kW at 20 mm/s and 1.3 kW at 15 mm/s. These welding conditions produced weld pool aspect ratios of 3.0, 2.6 and 2.1, respectively.

Measured properties of the welds produced using process parameters that resulted in relatively low aspect ratio welds are presented in Table 4.7. Reducing the aspect ratio was found to improve the joint efficiency compared to welds with aspect ratios greater than 3.7. Joint efficiencies of 100% were obtained with transverse tensile failure now occurring in the thin base metal sheet for specimens welded at 1.8 and 2.2 kW with welding speeds of 20 and 25 mm/s, respectively. Welds produced with a welding power of 1.3 kW and a welding speed of 15 mm/s exhibited base metal failure in 3 of 5 specimens.

Table 4.7: Properties of three welds produced using process parameters that resulted in relatively low weld pool aspect ratios.

Property	2.2 kW, 25 mm/s	1.8 kW, 20 mm/s	1.3 kW, 15 mm/s
Aspect Ratio	3.0	2.6	2.1
Joint Efficiency (%)	100 ± 0.0	100 ± 0.0	99.3 ± 0.93
$\sigma_{Y\,0.2}$ (MPa)	146 ± 5.47	146 ± 4.13	129 ± 5.64
UTS (MPa)	270 ± 19.2	282 ± 8.4	246 ± 4.7
% Elongation at Failure	13.6 ± 2.0	19.2 ± 2.8	17.7 ± 2.2

The yield strengths for longitudinal tensile tests on the base metal were consistent with the base metal results, unchanged from the yield strength of welds with larger aspect ratio weld pools. This finding suggests that the yield strength of 5182 alloys is not significantly influenced by solidification micro-porosity in the weld fusion zone. However, the ultimate tensile strength (UTS) and weld metal ductility were found to improve with decreasing weld pool aspect ratios. The best ductility results were obtained with the specimen welded with a power of 1.8 kW at a speed of 20 mm/s and a weld pool aspect ratio of 2.6. The percent elongation at failure for this specimen was 19.2% which is very close to the results obtained for the base metal of 22.5%. This result is also comparable to ductility results obtained from optimized GTAW welds on 5182 aluminum sheet from a previous study on aluminum TWBs [69].

Transverse metallographic specimens showed that the solidification micro-porosity was eliminated for all three low aspect ratio welding conditions. A representative image is shown in Figure 4.57 of a specimen welded at 1.8 kW and 20 mm/s. No micro-porosity was found when higher magnifications were used to examine these specimens. The lack of solidification shrinkage micro-porosity observed in the metallographic specimens for the weld at 2.2 kW and 25 mm/s would suggest that the weld metal ductility should be similar to that obtained for the weld produced at 1.8 kW and 20 mm/s; however, it is thought that very fine and undetectable solidification shrinkage porosity must exist in the weld produced with 2.2 kW at a welding speed of 25 mm/s. This hypothesis is supported by Shakeri *et al.* [71] who reported that 5754 aluminum alloy TWBs did not have any micro-structural defects prior to forming were found to have "V" and "W" shape defects after the specimens had been deformed. They

Figure 4.57: Low aspect ratio weld specimen produced with a welding power of 1.8 kW at a welding speed of 20 mm/s showing that the weld is free of solidification micro-porosity.

concluded that a number of flaws must exist in the weld metal that are undetectable and open up when the weld is deformed.

The difference in ductility between the base metal and the weld produced using 1.8 kW, at 20 mm/s welding conditions could be attributed to the presence of a few undetectable defects and the cast structure of the weld which would be expected to produce a lower consistency among results than the wrought base metal structure.

Limiting dome height testing was also conducted on the low aspect ratio weld specimens to examine the influence of the relative weld pool length on the post weld formability. The results have been summarized in Table 4.8. The weld produced at 1.8 kW and 25 mm/s with a weld pool aspect ratio of 2.6 clearly demonstrated the best forming results and is shown on the right in Figure 4.58. A total punch height at failure of 24.3 mm was observed which is 88.8% of the base metal formability. Further, the

Table 4.8: Limiting dome height test results for 1.0 to 1.5 mm thick 5182 aluminum alloy tailor welded banks produced with low aspect ratio weld pool dimensions.

Test Condition	Weld Pool Aspect Ratio	Punch Height at Failure (mm)	Percent of Base Metal Formability
1.0 mm Base Metal	-	27.4 ± 0.33	-
2.2 kW, 25 mm/s	3.0	22.3 ± 1.20	81.6
1.8 kW, 20 mm/s	2.6	24.3 ± 0.46	88.8
1.3 kW, 15 mm/s	2.1	22.4 ± 1.00	81.7

27.4 mm   24.3 mm
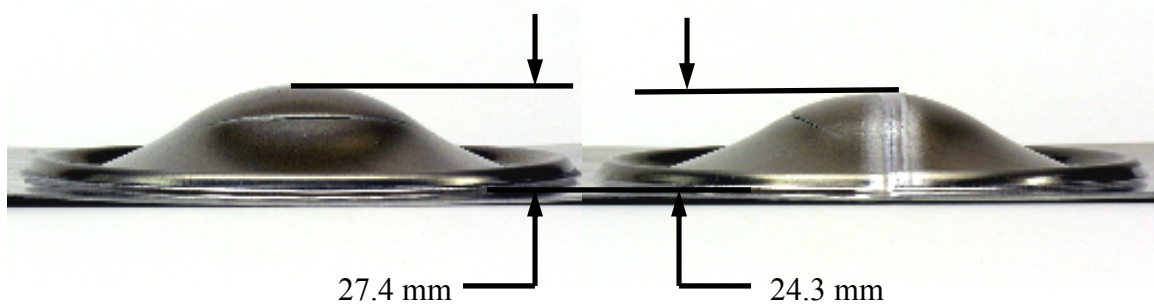
Figure 4.58: Limiting dome height specimen of 1 mm thick base metal (left) compared with a low aspect ratio TWB weld specimen produced with a welding power of 1.8 kW and a travel speed of 20 mm/s (right).

spread of experimental data was found to be the lowest for this test condition.   The other two low aspect ratio welding conditions also performed much better than previous welds. In all the low aspect ratio weld cases, the formability was found to exceed 80% of the base metal formability.   This suggests that very good forming results can be consistently obtained with 5182 aluminum alloy TWBs produced with DSAW provided that the aspect ratio of the weld pool is kept relatively small to avoid the formation of solidification micro-porosity at the tail of the weld pool.

Optimal forming properties were found to coincide with the 1.8 kW and 20 mm/s welding conditions that produced optimal weld metal ductility and ultimate tensile strengths. It is believed that the relatively short weld pool for this welding condition successfully minimized the micro-porosity defects that were found to inhibit forming and reduce the mechanical properties of the weld in earlier studies. The increased formability found for the low aspect ratio welds in this study matches the formability reported by Shakeri *et al.* [71] and Buste *et al.* [72] for 5754 aluminum alloy TWBs with similar thickness ratios to the 1.0 to 1.5 mm used in this study. The limiting dome heights at failure in this study were found to be better than those obtained with CO_2 laser welding on 5182 aluminum alloys [74]; however, no information was provided on the presence of internal weld defects for comparison to this study.

The significant increase in forming results compared to earlier limiting dome height tests in Section 4.5.1was accompanied by a change in the failure mode. The low aspect ratio welds were not observed to fail along the weld centerline. The higher punch height at failure of the low aspect ratio welds compared to the high aspect ratio welds discussed earlier allowed increased material deformation to occur prior to specimen failure. As a result, necking began to occur in a circular area on the specimen, the same as was observed on the base metal specimens. This is shown in Figure 4.59. In the specimens welded with a power of 2.2 kW at 25 mm/s shown in Figure 4.59a, failure was found to initiate where the weld and the circular ring intersected. The fracture then propagated along the circular ring towards the thinner base metal sheet. In the specimens

155
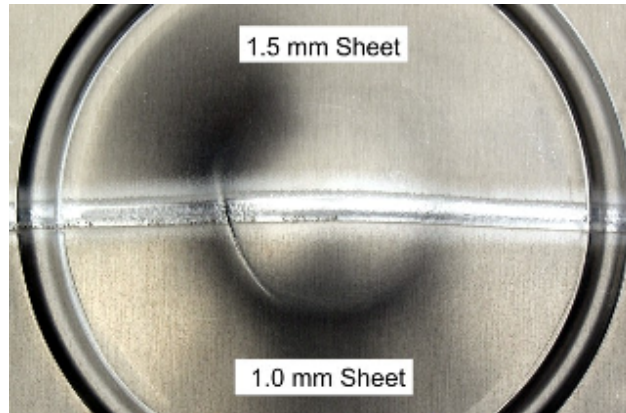
(a)
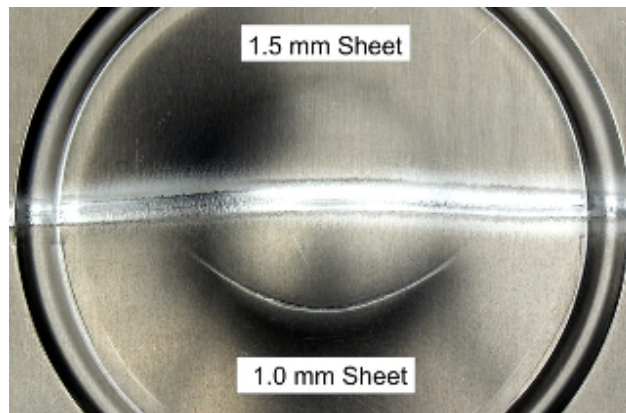
(b)
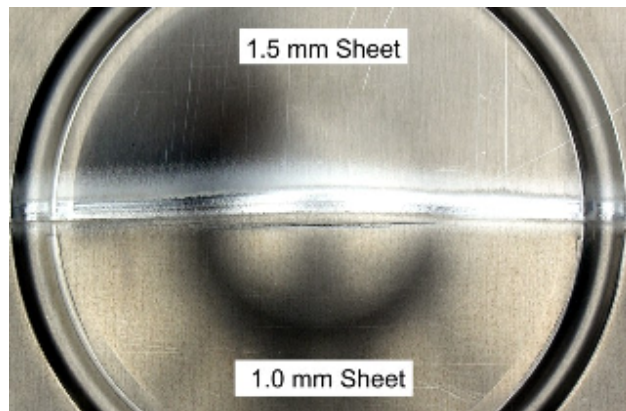
(c)

Figure 4.59: Typical limiting dome height failures observed for welded specimens produced with a) 2.2 kW at 25 mm/s and b) 1.8 kW at 20 mm/s and c) 1.3 kW at 15 mm/s.

welded with a power of 1.8 kW at 20 mm/s, fracture was observed to initiate in the thin sheet and propagate around the necked region in the specimen as shown Figure 4.59b.

The change in the fracture initiation point between these welding conditions is believed to be caused by strain localization around internal weld defects that would have promoted fracture initiation. Figure 4.59c shows the failure observed with the welding specimen produced with a 1.3 kW welding power at 15 mm/s. These specimens were observed to fail in the base metal parallel to the weld. It is not understood why failure occurred parallel to the weld instead of in the necked region observed in the other tests.

These findings suggest that the retention of weld metal ductility is very important in maximizing the formability of 5182 aluminum TWBs. In this study, specimens with tensile elongation of 17.7% were found to shift failure initiation during forming from the weld to the base metal. This ductility represents a 78% retention of the base metal ductility which was found to have an elongation of 22.5% at failure. These findings are further supported by the observation that a joint efficiency of 96% (for 2.6 kW welding power and 30 mm/s welding speed) was unable to attain acceptable forming results despite the transverse strength of the joint.

Figure 4.60 is an extension of

Figure 4.56 that includes the three low aspect ratio welding conditions examined. It is clearly shown in this figure that decreasing the aspect ratio of the weld pool has a very positive influence on the mechanical and forming properties of the weld. The improvement in the weld properties can be attributed to a decrease in quantity of solidification shrinkage micro-porosity that was observed in transverse cross sections. The decrease in micro-porosity is caused by a decrease in the length of the mushy zone comprised of solid and liquid phases during cooling and solidification of the weld pool.
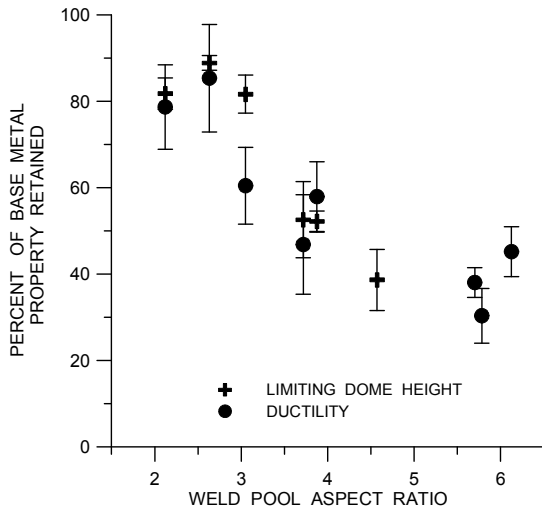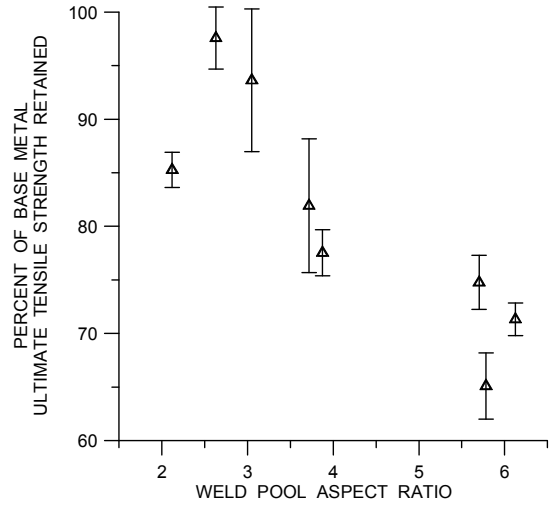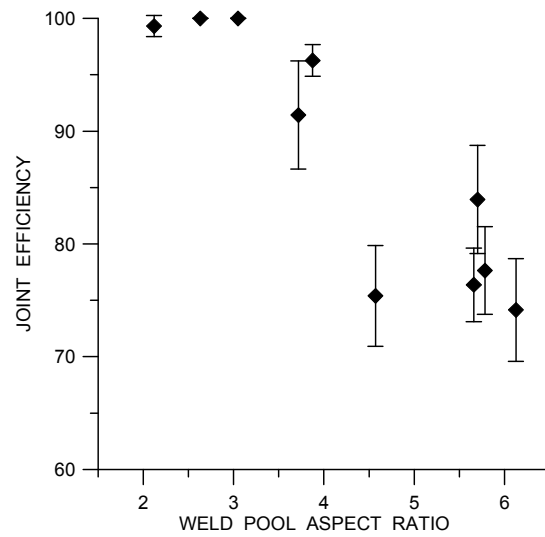
Figure 4.60: Mechanical and forming properties of 5182 aluminum alloy TWBs versus the DSAW weld pool aspect ratio including: a) limiting dome height and weld metal ductility, b) ultimate tensile strength and c) transverse joint efficiency.

pool. Therefore, it can be concluded that the quality and mechanical properties of the weld in this study of conduction-mode DSAW on 5182 aluminum alloys, were very dependent on the relative length to width ratio of the mushy zone during solidification. The length of the mushy zone will be determined by the thermal gradient at the tail end of the weld pool with higher thermal gradients producing shorter mushy regions during solidification. Therefore, welding conditions that produce high thermal gradients at the tail end of the weld pool will be expected to have shorter mushy zones, lower weld pool aspect ratios and improved mechanical properties compared to welding conditions that produce low thermal gradients. Furthermore, it is expected that the importance of the weld pool aspect ratio is likely to hold true for all conduction-mode welding processes used for welding 5182 aluminum alloys. This is supported by findings from other researchers who have used GTAW to weld aluminum alloys and have reported internal weld defects including lack of fusion and micro-porosity as the cause of degradation of mechanical properties [4,85,86]; however, these researchers did not offer an explanation to explain the presence of internal weld defects or provide evidence to support whether the welding parameters influenced the quantity of internal weld defects.

The findings of this study suggest that DSAW is a welding process that is capable of attaining high quality welds that have excellent mechanical and forming properties. From this perspective, however, the upper limit on the DSAW welding speed of 20 mm/s (1.2 m/min) that was found to produce excellent quality welds in this study, falls below the current production speeds of 133 to 200 mm/s (8 to 12 m/min) demanded for high production volumes [11].

Using the findings of this study, improvements in the upper limit of welding speeds capable of producing highly formable 5182 aluminum alloy TWBs may be achieved if welding conditions can be found that will maintain a weld pool aspect ratio below 2.6 and 3.0. The trends observed in this study suggest that increasing the welding speed above 25 mm/s will tend to increase the weld pool aspect ratio which would indicate that significant productivity improvements are not likely to be achieved in conduction mode DSAW.

Past studies on dual-beam laser welding of 5754 aluminum alloys have been found to retain greater than 80% of the base metal formability when welded with welding speeds of about 120 mm/s (7 m/min) [71,72]. It is suspected that these welds were made using keyhole mode due to the high energy density associated with the laser beam; however, no mention of the welding mode was given. It is thought that very high energy densities associated with laser beam welding may be capable of producing a weld with minimal solidification shrinkage micro-porosity due to the low net heat input and high cooling rates that would promote rapid solidification without forming a long, narrow weld pool. For this reason, examining the solidification structure of keyhole-mode welding processes to determine the threshold welding parameters that produce micro-porosity defects could provide further understanding of the productivity limits associated with welding 5182 aluminum alloy sheet for high production applications, such as automotive tailor welded blanks. Processes that might be suitable for such a study would be Nd:YAG laser welding, keyhole-mode micro-plasma arc welding, or a DSAW system that uses two micro-plasma welding torches.

Chapter 5

Summary and Conclusions

The feasibility and merits of using the conduction-mode Double-Sided Arc Welding process to manufacture 1.0 mm to 1.5 mm thick 5182 aluminum alloy tailor welded blanks in the flat position using a butt-joint configuration have been studied. The three main objectives of this study were: to identify the welding parameters that minimized the geometric discontinuity across the weld, to determine the range of welding speeds and powers that produced visually acceptable weld quality, and to evaluate the influence of welding parameters on the mechanical and forming properties of 5182 aluminum alloy TWBs produced with the DSAW process.

5.1 Effects of Welding Torch Standoff Distance

The effects of varying the GTAW and PAW welding torch standoff distances from 1.5 to 6.0 mm was investigated to determine if the arc forces, which act in opposite directions on the weld pool in DSAW, influence the final weld bead geometry, specifically weld bead drop through. The arc voltage was found to increase linearly by 0.67 V/mm for the GTAW torch and by 0.53 V/mm for the PAW torch with increasing torch standoff distances. The increased arc length and arc voltage were found to decrease the arc efficiency and result in narrower weld beads. Weld metal sag or drop through was not found to be influenced by varying the torch standoff distances. It was concluded that the expected variation in the ratio of arc forces due to changing the torch-to-work piece

standoff distances were insignificant in comparison to the surface tension and gravitational forces acting on the weld pool for a welding power of 3.0 kW.

5.2 Effects of PAW Electrode Geometry

The electrode tip geometry of the PAW torch electrode was investigated to determine the effects on the DSAW welding process and the resulting weld bead. It was found that using a blunt electrode tip instead of a conical, truncated electrode reduced the buildup of heat at the tip of the electrode. This minimized melting of the electrode tip and was found to improve the consistency of the DSAW welds produced by reducing the rate of electrode degradation. A blunt electrode tip was also found to cause a slight increase in the arc voltage caused by reduced thermionic emission from the cooler electrode surface. This was accompanied by a decrease in the net heat transfer to the work piece. It was found that a conical electrode truncated to a 3.2 mm diameter provided the best compromise between the process efficiency and the electrode life for welding powers between 1.8 and 4.6 kW.

5.3 Effects of DSAW Welding Process Parameters

The range of welding speeds and powers suitable for welding 5182 aluminum alloy TWBs were investigated to identify the DSAW process window for 1.0 to 1.5 mm thick sheets. It was found that net heat inputs between 60 and 110 J/mm produced visually acceptable welds when using welding powers ranging between 1.8 and 4.6 kW and travel speeds of 10 to 70 mm/s. Above 110 J/mm, blowholes were produced due to excessive heat input. The weld widths were found to decrease as the net heat input per unit distance was decreased by increasing the welding speed for a given welding power or by

162

decreasing the welding power for a given welding speed. Net heat inputs below 60 J/mm, resulted in inconsistent cathodic cleaning and arc coupling with the work piece, preventing acceptable quality welds from being produced.

Offsetting the welding torches in the transverse direction from the joint was investigated to determine if the DSAW weld bead quality could be influenced by the torch-to-joint alignment. It was found that offsetting the welding torches towards the thinner 1.0 mm sheet by 1 or 2 mm resulted in poor wetting of the thick sheet by the weld pool, poor coupling between the arc and the thick sheet and insufficient heat input into the thick sheet for melting to occur. This caused the thin sheet to overheat and blowholes to be produced in the thin sheet. On the other hand, offsetting the welding torches towards the thicker 1.5 mm thick sheet by 1 mm produced acceptable quality welds; however, offsetting the torches further towards the thicker 1.5 mm sheet caused poor wetting of the thin sheet by the weld pool and overheating of the thick sheet resulting in the formation of blowholes in the thick sheet only. It was concluded that the welding torches should be aligned with the joint or offset by 1 mm towards the thick sheet when welding 1.0 to 1.5 mm thick 5182 aluminum alloy sheets.

The transverse tensile strength of DSAW welds produced on 1.0 to 1.5 mm thick 5182 aluminum alloy sheets were found to approach the strength of the 1.0 mm thick base metal for a variety of welding conditions; however, the strength was found to decrease with welding speeds greater than 40 mm/s. No significant difference in micro-hardness was detected across the base metal, heat affected zone and fusion zone of welds produced in this study.

5.4 Effects of Wire Brushing Prior to Welding

Initial DSAW welds produced in this study on 5182 aluminum sheet were found to exhibit significant hydrogen porosity even though the weld specimens were thoroughly cleaned and degreased prior to welding. Stainless steel wire brushing weld specimens prior to welding was found to reduce the quantity of hydrogen gas porosity measured in metallographic cross sections of the fusion zone by 77 to 84% compared to specimens that were not wire brushed prior to welding. The reduction in hydrogen porosity was attributed to the removal of thick hydrated surface oxides that likely formed during extended material storage and produced a source of hydrogen gas to the weld pool during welding. It was concluded that stainless steel wire brushing is a critical material preparation step for TWBs produced with a DSAW process to minimize hydrogen gas pores that could otherwise reduce the ductility of the weld metal and inhibit the formability of a 5182 aluminum alloy TWB.

Stainless steel wire brushing was also found to improve the weld pool stability compared to non-brushed specimens. The improved weld pool stability allowed travel speeds to be increased by 15 to 20% for a given welding power thereby lowering the minimum heat input required to attain a consistent weld bead from 60 to 50 J/mm. Wire brushing also improved the visual appearance of the weld specimens, by eliminating the presence of dark particles of magnesium oxides on the weld bead surface.

5.5 Mechanical and Forming Properties of DSAW Welds

The mechanical and forming properties of the DSAW welds made on dissimilar thickness 5182 aluminum alloy sheet, (1.0 to 1.5 mm thick) have been evaluated for a wide range

of welding conditions. It was found that the yield strength and micro-hardness of the DSAW welds were comparable to the base metal properties and were not affected by the welding speed or welding power.

The ultimate tensile strength, ductility and post weld formability of the DSAW welds were found to be influenced by the welding process parameters, with particular emphasis on the welding speed. Ultimate tensile strengths were found to reach a high of 282 MPa and a low of 188 MPa, compared to the 288 MPa ultimate strength of the base metal. The weld metal ductility was found to vary between 6.8 and 19.2% elongation at failure compared to 22.5% for the base metal. Limiting dome height formability testing revealed that the formability of welded specimens was found to increase with increasing ductility and ultimate strength of the weld metal.

Welds made using welding speeds greater than 30 mm/s were found to exhibit solidification shrinkage micro-porosity and a corresponding degradation in mechanical properties, especially ductility and formability. As the welding speed was further increased, degradation of the material properties continued to increase due to an increase in the quantity of micro-porosity defects in the weld. These defects caused significant strain localization resulting in a marked decrease in ductility and formability. The severity of solidification shrinkage micro-porosity present in the weld metal was found to correspond to the relative length-to-width ratio of the weld pool for all of the welding conditions examined. Welds produced at high welding speeds resulted in large length-to-width ratios, a relatively large distance between the liquidus and non-equilibrium solidus and low thermal gradients in the mushy zone at the tail of the weld. These conditions are known to promote micro-porosity in alloys with a wide freezing range.

Alternatively, DSAW welds produced using welding speeds below 25 mm/s were found to produce excellent material properties that were nearly indistinguishable from the base metal with excellent ductility and formability. These welds had relatively small length-to-width ratios and little or no evidence of solidification micro-porosity, because the length of the mushy zone at the tail of the weld was much smaller and the thermal gradients were much higher. These conditions are known to prevent solidification micro-porosity during solidification of alloys with a wide freezing range. They also provide more time and opportunity for any hydrogen bubbles that may form during solidification to float up and escape through the top surface of the weld pool thereby further reducing the propensity for hydrogen porosity. The solidification shrinkage micro-porosity was found to be influenced by the welding speed with particular emphasis on the relative length-to-width of the weld pool. Increasing the length of the molten weld pool, relative to its width, was found to increase the quantity of micro-porosity contained in the weld. It was proposed that increasing the relative length of the weld pool increased the length of the mushy solid-liquid region during solidification which choked the flow of molten metal to fill voids left by solidification shrinkage. It was found that the maximum length-to-width ratio of the weld pool capable of producing a weld free of micro-porosity was 2.6, and was achieved using a welding power of 1.8 kW with a welding speed of 20 mm/s.

5.6 DSAW for Automotive Aluminum TWBs

The DSAW process has been shown to be capable of successfully producing tailor-welded blanks in 5182 aluminum alloy sheets with excellent ductility and formability provided that all sources of porosity are eliminated. This includes careful cleaning and

removal of preexisting hydrated oxides using stainless steel wire brushing prior to welding to minimize hydrogen porosity and welding at slow enough speeds to prevent the formation of solidification micro-porosity at the tail of the weld pool.

References

1. F. Stodolsky, A. Vyas, R. Cuenca, and L. Gaines, Life-cycle energy savings potential from aluminum-intenstive vehicles, SAE Tech. Paper Series 951837, SAE Int'l, Warrendale, PA..

2. I. Stol, Selecting manufacturing processes for automotive aluminum space frames, *Welding J.*, 1994, 73(2), 57-65.

3. I. D. Harris, Arc welding automotive aluminum, *Advanced Materials & Processes*, 2001, 158(8), 52-54.

4. R. W. Davies, H. E. Oliver, M. T. Smith, G. J. Grant, Characterizing Al tailor welded blanks for automotive applications, *J. Metals*, 1999, 51(11), 46-50.

5. E. Kubel, Manufacturers want more tailor welded blanks, *Manufact. Eng.*, 1997, 119(5), 38-45.

6. M. Bertram, K. Buxmann, R. Chase, P. Furrer, B. Gilmont, J. Hannagan, K. Martchek, P. Morton, G. Rebitzer, "Improving sustainability in the transport sector through weight reduction and the application of aluminum", Aluminum Assoc., European Aluminum Assoc. and Intl. Aluminum Inst., July, 2007.

7. H. Helms, U. Lambrecht, U. Hopfner, Energy savings by light weighting, Final Report, Inst. for Energy and Environmental Research, January 2003.

8. M. J. Wheeler, Aluminum tailor welded blanks, Lightweight Materials Workshop, Natural Resources Canada, Sheridan Park, Mississauga, June, 1999.

9. Kou, S., *Welding Metallurgy*, 2nd ed., John Wiley & Sons, Toronto, ON, Canada, 2003.

10. C. A. Huntington, T. W. Eagar, Laser Welding of Aluminum and Aluminum Alloys, *Welding J.*, 1982, 62(4), 105s-107s.

11. Duley, W. W., *Laser Welding*, John Wiley & Sons, Toronto, ON, Canada, 1999.

12. H. Zhao, D. R. White, T. DebRoy, Current issues and problems in laser welding of automotive aluminum alloys, *Intl Mater. Reviews*, 1999, 44(6), 228-266.

13. Cary, H. B., Helzer, S. C., *Modern Welding Technology*, 6th ed., Pearson Prentice Hall, Upper Saddle River, New Jersey, 2005.

14. M. Deutsch, *Effects of Nd:YAG laser welding and VPPAW welding process variables on weld geometry and defects of 1.6 mm thick 5182 aluminum*, MASc thesis, University of Waterloo, 2001.

15. M. G. Deutsch, A. Punkari, D. C. Weckman, H. W. Kerr, The weldability of 1.6 mm thick AA5182 aluminum sheet by single and dual-beam Nd:YAG laser welding, *Sci. Technol. Welding Joining,* 2003, 8(4), 246-256.

16. A. Punkari, *Variable Polarity Plasma Arc Welding and Dual-Beam Nd:YAG Laser Welding of Aluminum Alloys*, MASc. thesis, University of Waterloo, 2002.

17. A. Punkari, D. C. Weckman, H. W. Kerr, Effects of magnesium content on dual-beam Nd:YAG laser welding of aluminum-magnesium alloys, *Sci. Technol. Welding Joining,* 2003, 8(4), 269-282.

18. D.W. Moon, E. A. Metzbower, Laser beam welding of aluminum alloy 5456, *Welding J.*, 1983, 63(2), 53s-58s.

19. M. Pastor, H. Zhao, R. P. Martukanitz, T. DebRoy, Porosity, underfill and magnesium loss during continuous wave Nd:YAG laser welding of thin plates of aluminum alloys 5182 and 5754, *Welding J.*, 1999, 79(6), 207s-216s.

20. M. Kutsuna, Q. Yan, Study on porosity formation in laser welds in aluminum alloys (Report 1): Effects of hydrogen and alloying elements, *Welding Intl.*, 1998, 12(12), 20-32.

21. P. Vilaca, J. P. Santos, A. Gois, L. Quintino, Joining aluminum alloys dissimilar in thickness by friction stir welding and fusion processes, *Welding in the World*, 2005, 49(3), 56-62.

22. M. P. Miles, B. J. Decker, T. W. Nelson, Formability and strength of friction stir welded aluminum sheets, *Metall. Mater. Trans. A*, 2004, Vol. 35A, 3461-3468.

23. *AWS Welding Handbook*, Vol. 2, *Welding Processes*, 8th ed. American Welding Society, Miami, FL, 1991.

24. Y. M. Zhang and S. B. Zhang, Method of arc welding using dual serial opposed torches, US Patent no. 5,990,446, Nov. 23, 1999.

25. Y. M. Zhang, S. B. Zhang, Double-sided are welding increases joint penetration, *Welding J.*, 1998, 77(6), 57-61.

26. Y. M. Zhang, S. B. Zhang, Double-sided GTA welding of aluminum alloys with single power supply, Proc. 5th Int'l Conf. "Trends in Welding Research", Pine Mountain, GA, USA, June 1-5, 1998, J. M. Vitek S. A. David, J. A. Johnson, H. B. Smartt, T. DebRoy, eds., ASM Int'l, Materials Park, OH, 271-275.

27. Y. M. Zhang, S. B. Zhang, M. Jiang, Keyhole double-sided arc welding process, *Welding J.*, 2002, 81(11), 249s-255s.

28. Y. M. Zhang, C. Pan, A. T. Male,Welding of austenitic stainless steel using a double-sided arc welding process, *Mater. Sci. Technol.*, 2001, 17(10), 1280-1284.

29. Y. Kwon, *Double-Sided Arc Welding of AA5182 Aluminum Alloy Sheet*, MASc. thesis, University of Waterloo, 2003.

30. Y. Kwon, D. C. Weckman, Double sided arc welding of 5182 aluminum alloy sheet, Accepted October 2007 to *Sci. Technol. Welding Joining.*

31. Y. Kwon, D. C. Weckman, An analytical thermal model of conduction mode double sided arc welding, Accepted May 2008, *Sci. Technol. Welding Joining.*

32. S. Anousheh, *Optimization of Weld Bead Shape in Double-Sided Arc Welding of AA5182 Aluminum Sheet*, MASc thesis, University of Waterloo, 2006.

33. E. Craig, The plasma arc process – a review, *Welding J.*, 1988, 67(2), 19-25.

34. Lancaster, J. F., *The Physics of Welding*, 2nd ed., Int'l Institute of Welding, Pergamon Press, Toronto, ON, Canada, 1986.

35. P. W. Fuerschbach, Cathodic cleaning and heat input in variable polarity plasma arc welding of aluminum, *Welding J.,* 1998, 77(2), 76s-85s.

36. T. B. Correy, Effect of gas pressures on etching and surface roughness of cathodically etched metal surfaces, *Proc., Physics of the Welding Arc, A Symposium, Institute of Welding, London,* 1962, 224-233.

37. Q. Pang, T. Pang, J.C. McClure, A.C. Nunes, Workpiece cleaning during variable polarity plasma arc welding of aluminum, *Trans. ASME J. Eng. Industry,*1994, Vol. 116, 463-466.

38. P. W. Fuerschbach, G. A. Knorovsky, A study of melting efficiency in plasma arc and gas tungsten arc welding, *Welding J.*, 1991, 70(11), 278s-297s.

39. N. S. Tsai, T. W. Eager, Distribution of the heat and current fluxes in gas tungsten arcs, *Metall. Trans. B,* 1985, Vol. 16B, 841-846.

40. M. Lu, S. Kou, Power and current distribution in gas tungsten arcs, *Welding J.,* 1988, 67(2), 29s-34s.

41. L. F. Martinez, C. Matlock, R. E.Marques, J. C. McClure, A. C. Nunes Jr., Effect of weld gases on melt zone size in VPPA welding of Al 2219, *Welding J.,* 1994, 73(10), 51-55.

42. A. C. Nunes JR., E. O. Bayless JR., C. S. Jones III, P. M. Munafo, A. P. Biddle, W. A. Wilson, Variable polarity plasma arc welding on the space shuttle external tank, *Welding J.*, 1984, 63(9), 27-35.

43. J. Dowden, P. Kapadia, B. Fenn, Space charge in plasma arc welding and cutting, *J. Physics D (Applied Physics)*, 1993, 26(8), 1215-1223.

44. Y. M. Zhang, S. B. Zhang, Welding Aluminum Alloy 6061 with the opposing dual-torch GTAW process, *Welding J.*, 1999, 78(6), 202s-206s.

45. Y. M. Zhang, C. Pan, A. T. Male, Solidification behaviour of Al-Mg aluminum alloy using double-sided arc welding process, *J. Mater. Sci. Letters*, 2000, 19, 831-833.

46. Y. M. Zhang, C. Pan, A. T. Male, Improved microstructure and properties of 6061 aluminum alloy weldments using a double-sided arc welding process, *Metall. Mater. Trans. A*, 2000, Vol. 31A, 2537-2543.

47. P. A. Woods, D. R. Milner, Motion in the weld pool in arc welding, *Welding J.,* 1971, 50(4), 163s-173s.

48. S. D. Kim, S. J. Na, Effect of weld pool deformation on weld penetration in stationary gas tungsten arc welding, *Welding J.,* 1992, 71(5), 179s-193s.

49. K. Hong, D.C. Weckman, A. B. Strong, The influence of thermofluids phenomena in gas tungsten arc welds in high and low thermal conductivity metals, *Can. Metall. Quart.,* 1998, 37(3-4), 293-303.

50. J. C. Metcalfe, M. B. C. Quigley, Heat transfer in plasma arc welding, *Welding J.,* 1975, 54(3), 99s-103s.

51. T. D. Burleigh, T. W. Eagar, Measurement of the force exerted by a welding arc, *Metall. Trans. A,* 1982, 14(6), 1223-1224.

52. S. I. Rokhlin, A. C. Guu, A study of arc force, pool depression, and weld penetration during gas tungsten arc welding, *Welding J.,* 1993, 72(8), 381s-390s.

53. E. Friedman, Analysis of weld puddle distortion and its effects on penetration, *Welding J.,* 1978, 57(6), 161s-166s.

54. J. Converti, Ph. D. Thesis, Mechanical Engineering, M.I.T., Cambridge, MA, July 1981, p. 57.

55. M. L. Lin, T. W. Eager, Influence of arc pressure on weld pool geometry, *Welding J.,* 1985, 64(6), 163s-169s.

56. W. F. Savage, E. F. Nippes, K. Agusa, Effect of arc force on defect formation in GTA welding, *Welding J.,* 1979, 58(7), 212s-224s.

57. R. F. Ashton, R. P. Wesley, C. R. Dixon, The effect of porosity on 5086-H116 aluminum alloy welds, *Welding J.,* 1975, 54(3), 95s-98s.

58. J. F. Rudy, E. J. Rupert, Effects of porosity on mechanical properties of aluminum welds, *Welding J.,* 1970, 49(7), 322s-336s.

59. R. J. Shore, R. B. McCauley, Effects of porosity on high strength aluminum 7039, *Welding J.,* 1970, 49(7), 311s-321s.

60. F. I. Saunders, R. H. Wagoner, Forming of tailor-welded blanks, *Metall. Mater. Trans. A,* 1996, 27A, 2605-2616.

61. C.J. Bayley, A. K. Pilkey, Influence of welding defects on the localization behaviour of an aluminum tailor-welded blank, *Mater. Sci. Eng. A,* 2005, 403, 1-10.

62. R. A. Woods, Porosity and hydrogen absorption in aluminum welds, *Welding J.,* 1974, 53(3), 97s-108s.

63. Z. P. Saperstein, G.R. Prescott, E. W. Monroe, Porosity in Aluminum welds, *Welding J.,* 1964, 40(10), 443s-453s.

64. J. H. Devletian, W.E. Wood, Factors affecting porosity in aluminum welds – A review, *Welding Research Council Bulletin,* Dec. 1983, Vol. 290, 1-18.

65. *AWS Welding Handbook*, Vol. 3, *Materials and Applicatons Part 1*, American Welding Society, Miami, Florida, 1996.

66. A. T. D'Annessa, Microstructural aspects of weld solidification, *Welding J.,* 1967, 46(11), 491s-499s.

67. J. D. Dowd, Inert shielding gases for welding aluminum, *Welding J.,* 1956, 35(4), 207s-210s.

68. F. R. Collins, Porosity in aluminum alloy welds, *Welding J.,* 1958, 37(6), 589-593.

69. R. W. Davies, M. T. Smith, H. E. Oliver, M. A. Khaleel, S. G. Pitman, Weld metal ductility in aluminum tailor welded blanks, *Metall. and Mater. Trans. A,* 2000, Vol. 31A, 2755-2763.

70. ASM Handbook Vol. 2, Properties and Selection: Nonferrous Alloys and Special Purpose Materials, 10th ed. ASM International, Materials Park, OH, 1990.

71. H. R. Shakeri, A. Buste, M. J. Worswick, J. A. Clarke, F. Feng, M. Jain, M. Finn, Study of damage initiation and fracture in aluminum tailor welded blanks made via different welding techniques, *J. Light Metals,* 2002, 2(2), 95-110.

72. A. Buste, X. Lalbin, M. J. Worswick, J. A. Clarke, B. Altshuller, M. Finn, M. Jain, Prediction of strain distribution in aluminum tailor welded blanks for different welding techniques, *Can. Metall. Quart.,* 2000, 39(4), 1-10.

73. C. H. Cheng, L. C. Chan, C. L. Chow, T. C. Lee, Experimental investigation on the weldability and forming behaviour of aluminum alloy tailor-welded blanks, *J. Laser Appl.,* 2005, 17(2), 81-88.

74. K. H. Leong, K. R. Sabo, B. Altshuller, T. L. Wilkinson, C. E. Albright, Laser beam welding of 5182 aluminum alloy sheet, *J. Laser Appl.,* 1999, 11(3), 109-118.

75. G. Reid, Personal Communications, Thermal Arc, Ohio, October 2006.

76. CAN/CSA – W117.2-M87, Safety in Welding, Cutting and Allied Processes, Can. Standard Assoc., Toronto, ON, 1987, Section 5.3.2.2

77. Smith, W. F., *Structure and Properties of Engineering Alloys,* 2nd ed., McGraw-Hill, Toronto, ON, 1993.

78. M. M. Mossman, J. C. Lippold, Weldability testing of dissimilar combinations of 5000 and 6000 series aluminum alloys, *Welding J.,* 2002, 81(11), 188s-194s.

79. R. Pistor, Personal communications, Liburdi Automation Inc., Dundas, ON, Nov. 2006.

80. B and B Precision Machine Inc., B and B Torch brochure. 6762 Hwy 431 South, Owens Cross Roads, AL 35763, 2000.

81. Thermal Dynamics Corp., Thermal Arc WC100B Plasma Torch Manual. 1983, West Lebanon, N.H., U.S.A.

82. G. F. Vander Voort, "Metallography Principles and Practice", ASM International, Materials Park, OH, 1999, 510s, 610s.

83 M. Miles, Formability Testing of Sheet Metals, Metalworking: Sheet Forming, Vol. 14B ASM Handbook, ASM Int'l, Materials Park, OH, 2006, pp 673-696.

84 CAN/CSA – W59.2-M1991. Welded Aluminum Construction, Can. Standard Assoc., Toronto, ON, 1991, p 40.

85   J. P. Anson, J. E. Gruzleski, The quantitative discrimination between shrinkage and gas porosity in cast aluminum alloys using spatial data analysis, *Materials Characterization,* 1999, 43, 319-335.

86   L. Li, Z. Liu, M. Snow, Effect of defects on fatigue strength of GTAW repaired cast aluminum alloy, *Welding J.,* 2006, 85(11), 264s-270s.

87   Flemings, M. C., *Solidification Processing,* McGraw-Hill, Toronto, ON, Canada, 1974.

88   S. Barker, 5182 aluminum alloy ThermalCalc simulation, Novellis Inc., Kingston, ON, May, 2008

Appendix A – Microhardness and Tensile Data
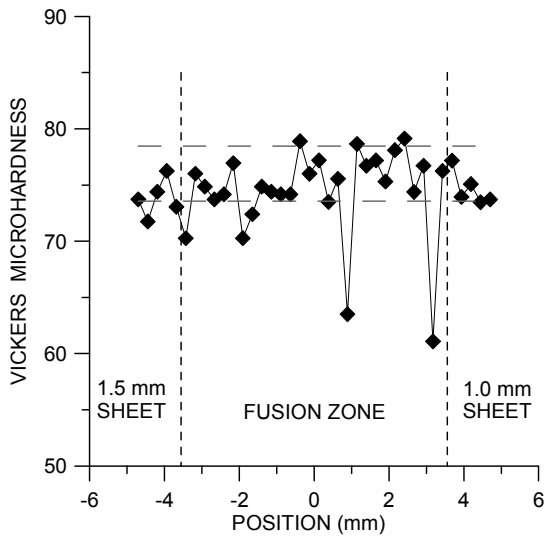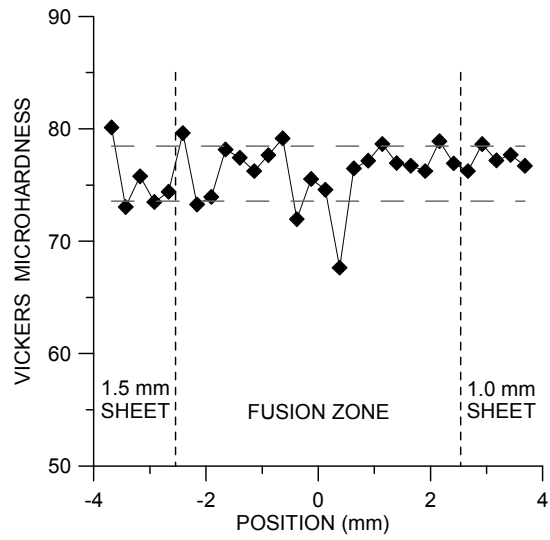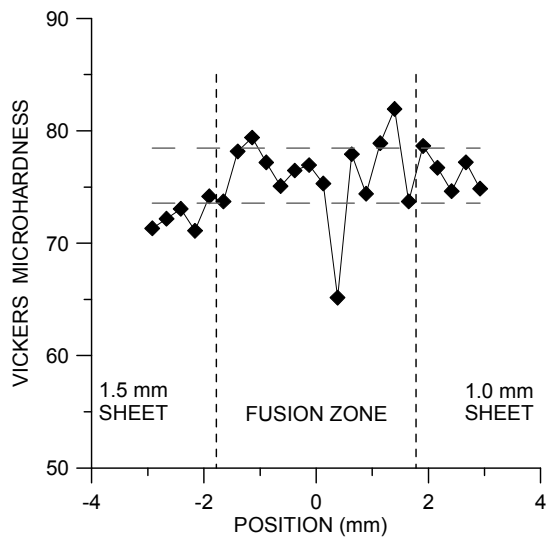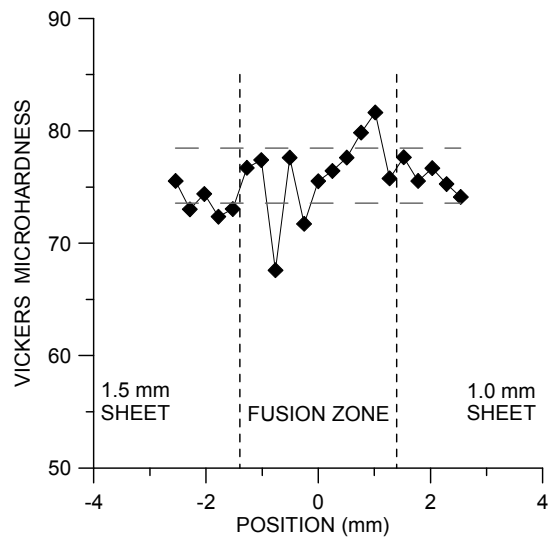
Figure A.1: Vickers microhardness results for welds produced with a total welding power of 2.6 kW and welding speeds of: (a) 20 mm/s, (b) 30mm/s, (c) 40 mm/s, (d) 50 mm/s. The horizontal lines on each plot represent plus and minus one standard deviation of the average base metal hardness.
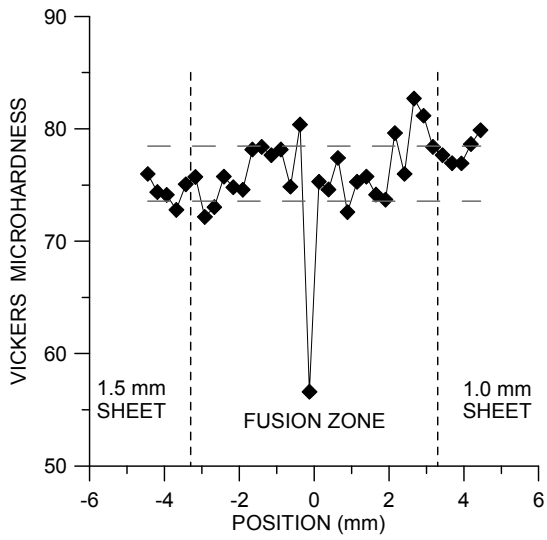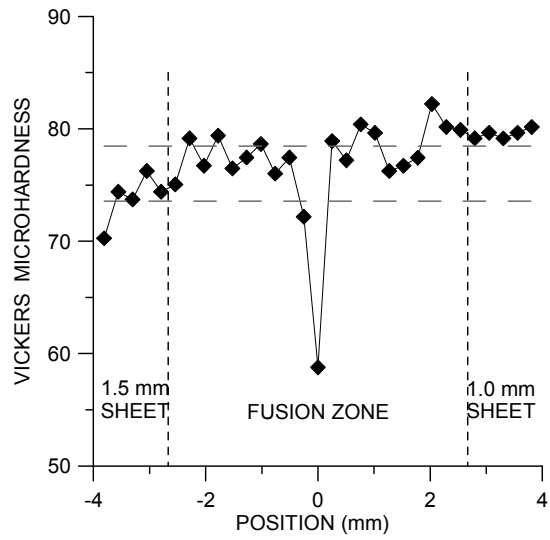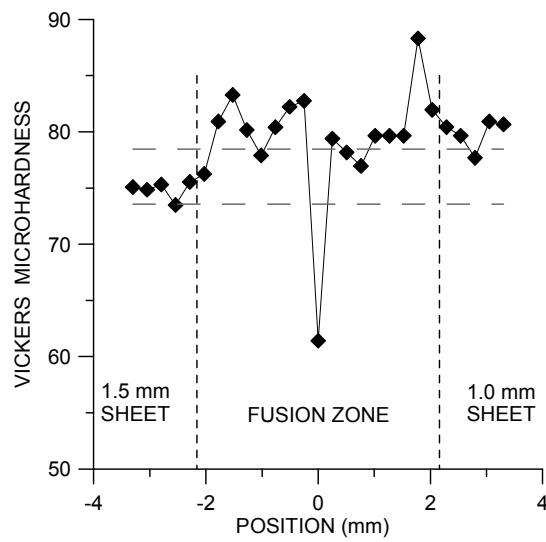
Figure A.2: Vickers microhardness results for welds produced with 4.2 kW total welding power at travel speeds of (a) 40 mm/s, (b) 50 mm/s, (c) 60 mm/s.
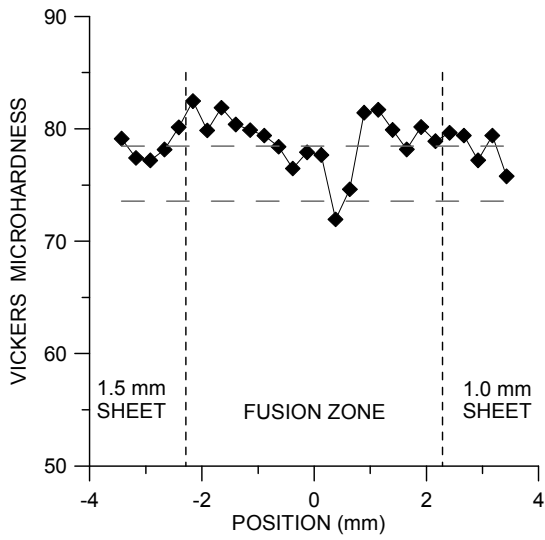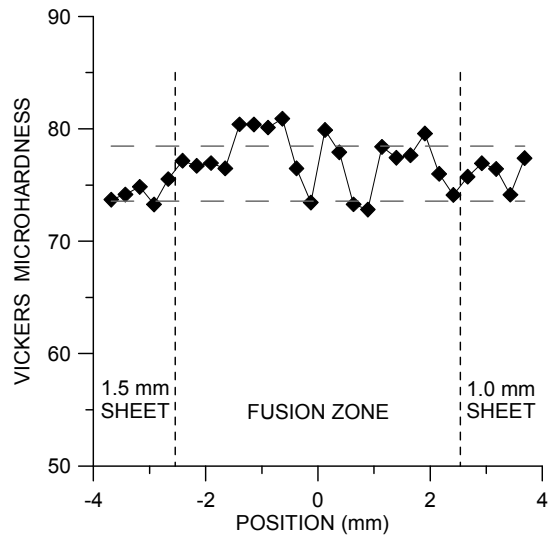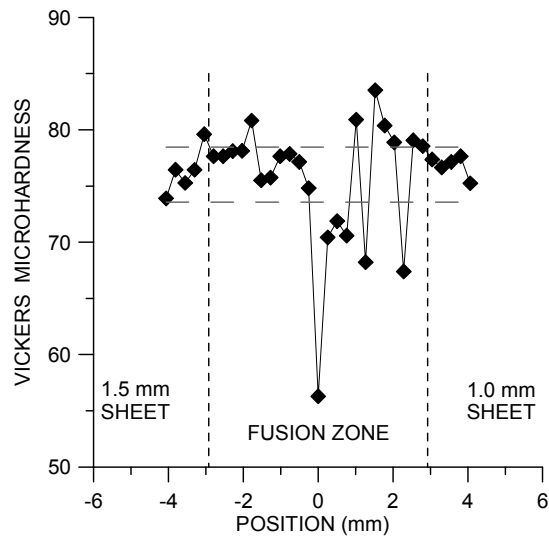
Figure A.3: Vickers microhardness results for welds produced with a welding speed of 40 mm/s and total welding powers of (a) 3.0 kW, (b) 3.4 kW, (c) 3.8 kW.
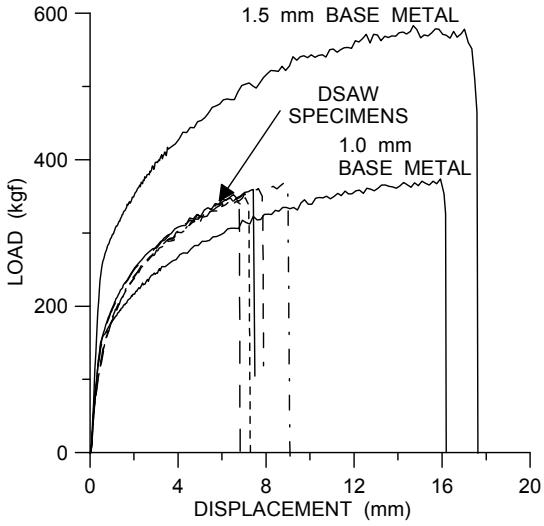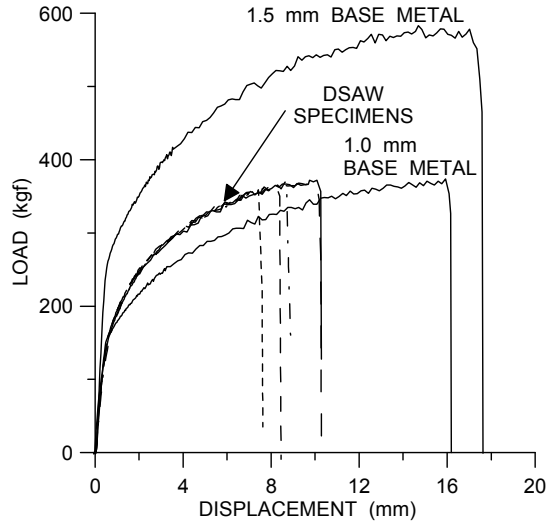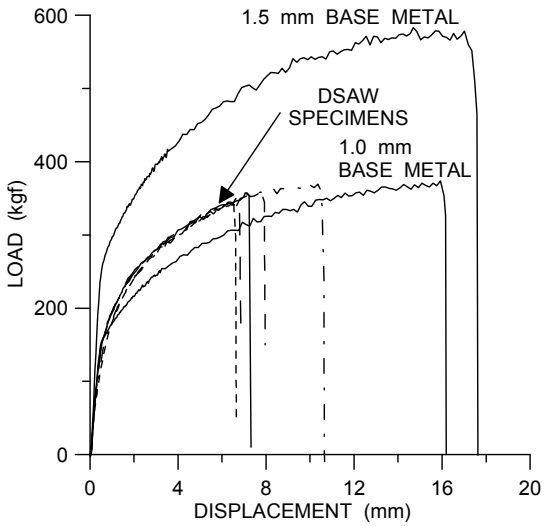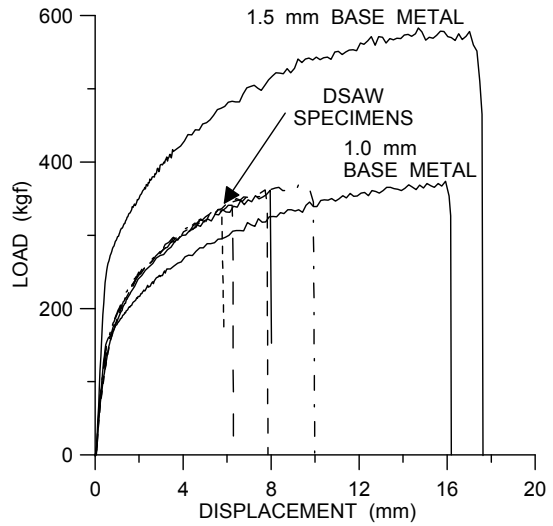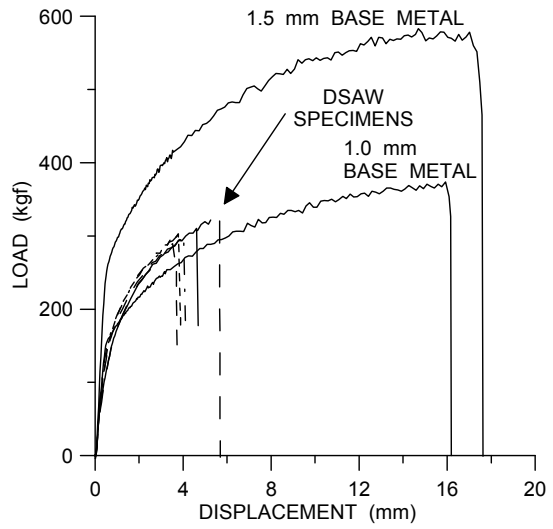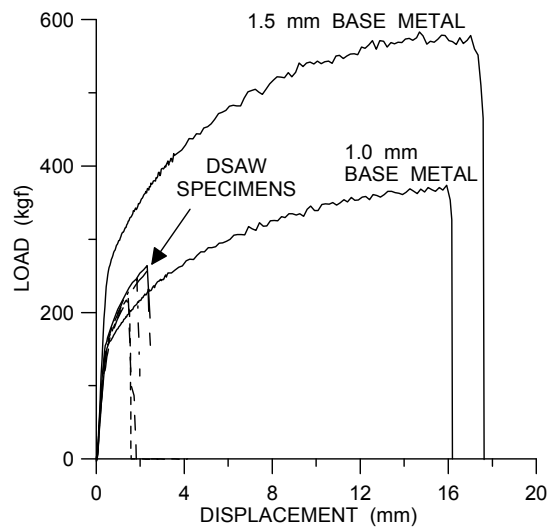
Figure A.4: Load displacement curves obtained from transverse tensile tests of welds produced with 2.6 kW total welding power at travel speeds of (a) 20 mm/s, (b) 30 mm/s, (c) 40 mm/s, (d) 50 mm/s.
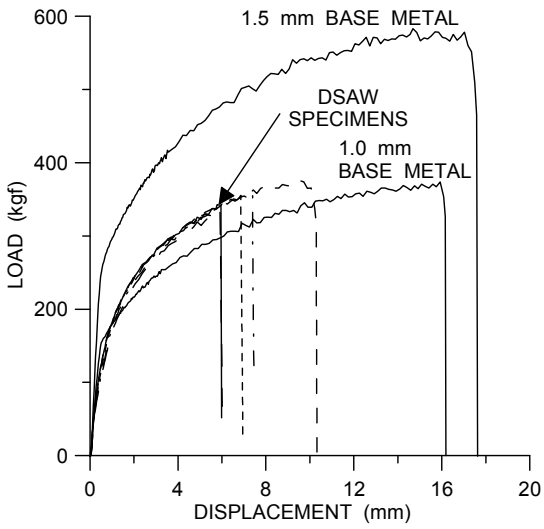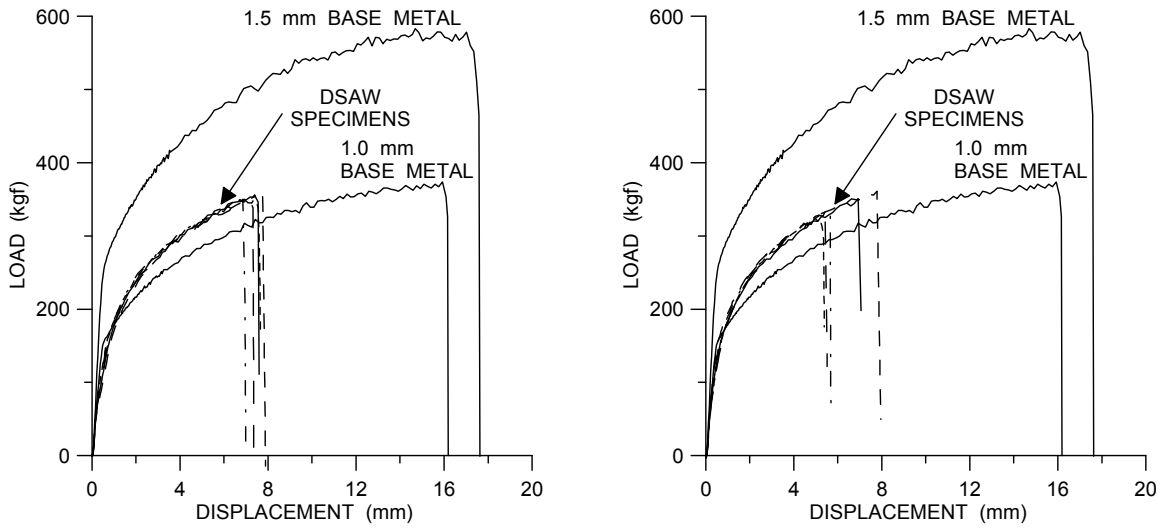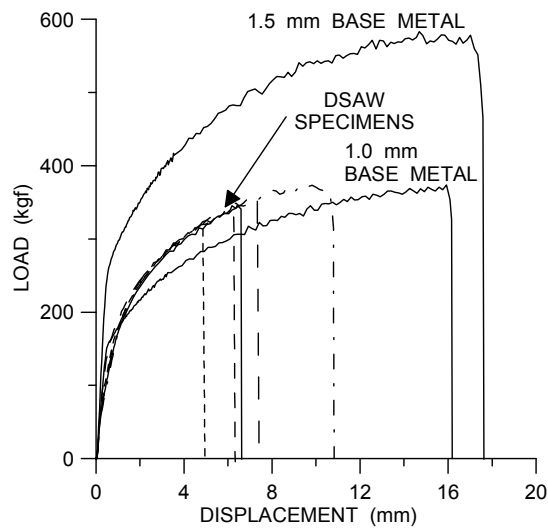
Figure A.5: Load displacement curves obtained from transverse tensile tests of welds produced with 4.2 kW total welding power at travel speeds of (a) 40 mm/s, (b) 50 mm/s, (c) 60 mm/s.

Figure A.6: Load displacement curves obtained from transverse tensile tests of welds produced with a welding speed of 40 mm/s and total welding powers of (a) 3.0 kW, (b) 3.4 kW, (c) 3.8 kW.